

# Development of Optimized Therapeutic Platforms for Magnetic Fluid Hyperthermia in Adjuvant Cancer Therapies

by

*Fernando José Mérida Figueróa*

A dissertation submitted in partial fulfillment of the requirements for the degree of

DOCTOR OF PHILOSOPHY  
In  
CHEMICAL ENGINEERING

UNIVERSITY OF PUERTO RICO  
MAYAGÜEZ CAMPUS

2018

Approved by:

\_\_\_\_\_  
Madeline Torres-Lugo, Ph.D.  
President, Graduate Committee

\_\_\_\_\_  
Date

\_\_\_\_\_  
Maribella Domenech, Ph.D.  
Member, Graduate Committee

\_\_\_\_\_  
Date

\_\_\_\_\_  
Eduardo Juan, Ph.D.  
Member, Graduate Committee

\_\_\_\_\_  
Date

\_\_\_\_\_  
Jorge Almodóvar, Ph.D.  
Member, Graduate Committee

\_\_\_\_\_  
Date

\_\_\_\_\_  
Solangie Pagán, Dr. PH  
Graduate Studies Representative

\_\_\_\_\_  
Date

\_\_\_\_\_  
Aldo Acevedo, Ph.D.  
Chair, Department of Chemical Engineering

\_\_\_\_\_  
Date

©Copyright 2018  
Fernando José Mérida Figueróa  
All rights reserved

This dissertation contains portions that were published by the author in the *Journal of Magnetism and Magnetic Materials*

## Abstract

Magnetic Fluid Hyperthermia (MFH) has a great potential as an adjuvant in cancer therapy, enhancing the effects of antineoplastic agents, sensitizing resistant cancers and reducing undesired side effects. When compared to other local hyperthermia approaches, non-specific heating is reduced with MFH since the heat is produced only when alternating magnetic fields are turned on. The clinical translation of MFH faces several challenges including nanoparticle low heat dissipation rates, limited cellular uptake of drugs and/or nanoparticles, and poor nanoparticle accumulation in tumors after intravenous injection. To tackle these challenges, the following hypotheses were proposed: (i) optimization of synthesis and peptization of magnetic nanoparticles will lead to increased heat dissipation rates; (ii) the use of low-intensity ultrasound will improve the cellular uptake of drugs and nanoparticles, potentiating the effects of MFH/drug combination therapies, and (iii) the intraperitoneal administration of nanoparticles will induce their uptake by mouse peritoneal macrophages and tumors. To test these hypotheses, systematic experimental designs were proposed to evaluate nanoparticle properties and their performance *in vitro* and *in vivo*. The coprecipitation synthesis and peptization of iron oxide nanoparticles were optimized, obtaining nanoparticles with remarkably high heat dissipation rates in liquid and solid matrices. Using an *in vitro* ovarian cancer model, increased cytotoxic profile of the drug 2-phenylethanesulfonamide was observed when low-intensity ultrasound was coupled to MFH/drug combination therapies. *In vivo* intraperitoneal administration of nanoparticles did not improve nanoparticle accumulation in subcutaneous breast cancer tumors, but significantly induced uptake by peritoneal macrophages which promoted accumulation in omental tissues. These results demonstrated that optimization of experimental methodologies was key to enhance nanoparticle properties, potentiating novel chemotherapeutic agents and fostering opportunities for improved nanoparticle delivery *in vivo*.

## Resumen

La hipertermia por fluidos magnéticos (MFH) tiene un inmenso potencial como coadyuvante en terapias para cáncer, mejorando los efectos de antineoplásicos, convirtiendo cánceres resistentes en sensibles, y reduciendo efectos secundarios indeseados. Comparada con otras formas de hipertermia local, el calentamiento no específico es reducido con MFH ya que el calor es producido solamente cuando los campos magnéticos externos son activados. La incorporación de MFH en la clínica enfrenta varios retos incluyendo bajas tasas de disipación de calor, limitada internalización de drogas y/o nanopartículas, y poca acumulación de nanopartículas en tumores luego de inyección intravenosa. Para aplacar estos retos, las siguientes hipótesis fueron propuestas; (i) la optimización de síntesis y peptización de nanopartículas magnéticas mejorará la liberación de calor; (ii) el uso de ultrasonido de baja intensidad mejorará la internalización de drogas y nanopartículas, potenciando los efectos de terapias combinadas de MFH/drogas, y (iii) la administración intraperitoneal de nanopartículas inducirá su internalización en macrófagos peritoneales de ratón y en tumores. Para probar estas hipótesis, diseños experimentales sistemáticos fueron propuestos para evaluar propiedades de nanopartículas y su desempeño *in vitro* e *in vivo*. La síntesis por co-precipitación y peptización fueron mejoradas, obteniendo nanopartículas con liberación de calor notablemente altas en preparaciones líquidas y sólidas. Usando un modelo de cáncer de ovario *in vitro*, se observó que el perfil citotóxico de la droga 2-feniletino sulfonamida (PES) aumentó cuando el ultrasonido de baja intensidad fue acoplado a terapias combinadas de MFH/droga. La administración intraperitoneal de nanopartículas *in vivo* no mejoró la acumulación de nanopartículas en tumores subcutáneos de cáncer de seno, pero indujo significativamente la internalización en macrófagos peritoneales, lo cual promovió la acumulación en tejidos del omentum. Estos resultados demostraron que la optimización de metodologías experimentales fue clave para mejorar propiedades de nanopartículas, potenciando agentes quimioterapéuticos novedosos y promoviendo oportunidades para la distribución mejorada de nanopartículas *in vivo*.

## List of publications and conferences

### Publications:

- **Mérida, F.**, Chiu-Lam, A., Bohórquez, Ana C., Maldonado-Camargo, L., Pérez, M.E., Pericchi, L., Torres-Lugo, M., Rinaldi, C. Optimization of synthesis and peptization steps to obtain iron oxide nanoparticles with high energy dissipation rates. *J. Magn. Magn. Mater.* 394, 361-371 (2015).
- Alvarez-Berrios, M. P., Castillo, A., **Mérida, F.**, Mendez, J., Rinaldi, C., Torres-Lugo, M. Enhanced proteotoxic stress: one of the contributors for hyperthermic potentiation of the proteasome inhibitor bortezomib using magnetic nanoparticles. *Biomater. Sci.* 3, 391-400 (2015).

### Oral presentations:

- **Mérida, F.** and Torres-Lugo, M. “Magnetic hyperthermia in cancer treatment”. XXII Latin American Congress of Chemical Engineering (COLAEIQ). Medellín, Colombia. July 2016.
- **Mérida, F.**, Juan, E., Rinaldi, C., Torres-Lugo, M. “Development of optimized strategies for magnetic hyperthermia in the treatment of ovarian cancer”. 36<sup>th</sup> Annual Research and Education Forum. University of Puerto Rico, Medical Sciences Campus. San Juan, PR. March 2016
- **Mérida, F.**, Chiu-Lam, A., Bohórquez, A.C., Maldonado-Camargo, L., Torres-Lugo, M., Rinaldi, C. “Optimized synthesis of high-energy dissipating iron oxide nanoparticles for magnetic hyperthermia in ovarian cancer cells” AIChE Annual Meeting. Salt Lake City, UT. November 2015.

*Dedicated to:*

*My parents*

*JUAN DOMINGO and AURA LEONOR*

*my siblings*

*JOSÉ JUAN and MARÍA JOSÉ*

*For their unconditional love, support and understanding...  
You are my everything.*

*My beautiful GUATEMALA,*

*“The soul of the Earth”*

*Hopefully my work will contribute to its scientific development*

*GOD*

*Who always knows why and how things happen...*

*My friends and every person from whom I have received and shared support, advice and apprenticeship.*

*“A veces, uno espera impaciente por vivir la gran aventura de su vida, quizás sin percatarse que, desde siempre, ha estado viviendo una vida llena de aventura”*

## **Acknowledgements**

This work was possible thanks to the intervention of people whose support was pivotal to accomplish the goals of this doctoral project. First of all, I want to express my gratitude to Dr. Madeline Torres-Lugo for accepting me in her research group, and for all the guidance and support received during the course of this work. My gratitude is also to Dr. Carlos Rinaldi from University of Florida for the extensive mentoring and advice received, and for accepting me as visiting student in his research team.

I want to thank to former and current CBEN members and lab mates. Janet Méndez: Thanks for trainings, ideas, discussions, and all kinds of support. Karem Court and Marisel Sánchez for their help in designing/discussing experiments. Jorge Castro for his help as my “bodyguard” during late night experiments, and for support in graphic design. Nicole Pérez and Tania Ramos for their support. To all of them, thanks for those good lab moments too.

I want to give special thanks to Ana Carolina Bohórquez for being my first mentor in the “nanoworld” and for all the time devoted to train me. My eternal gratitude to Andreina Chiu-Lam for her mentoring in various fields, especially in the work with laboratory animals. Thanks for her unconditional support and commitment in the design and execution of experiments, along with the discussion of results.

Special thanks to the members of my Committee: Dr. Eduardo Juan, Dr. Maribella Domenech and Dr. Jorge Almódovar. Thanks for their feedback, comments and suggestions in this work.

I want to thank to former and current members of the Rinaldi Research Lab: Lorena Maldonado-Camargo, Melissa Cruz-Acuña, Tapomoy Bhattacharjee and Shehaab Savliwala for

their collaboration. To former and current members of BIR Lab: Leonardo Rodríguez-Negrón and Christian Colón for their support in the electrical part of this work.

Thanks to my friends for their support, patience and love, because no matter the distance or the time, they were (and are) always there for me. I will not write down names, though they know I am truly grateful with them.

Finally, I want to acknowledge to the funding agencies that have made this work possible: U.S. National Science Foundation under award # HRD-0833112 and HRD-1345156 (CREST Program), the PR Institute for Functional Nanomaterials (EPS-100241) and the US national Institutes of Health (U54 CA 96300/u54 ca 96297). Also, a special acknowledgement to Lantheus Medical Imaging Inc. for donating the ultrasound contrast agents used in experiments referred in Chapter 3 of this dissertation.

## Table of contents

Abstract.....	III
Resumen.....	IV
List of publications and conferences.....	V
Dedication.....	VI
Acknowledgements.....	VII
List of figures.....	XIII
List of tables.....	XVII
<i>Chapter 1.</i> Introduction.....	1
1.1. Justification.....	1
1.2. Rationale and background.....	4
1.2.1. Magnetic nanoparticles and heat dissipation.....	6
1.2.2 Biological aspects of cancer.....	10
1.2.3 Magnetic Fluid Hyperthermia (MFH).....	13
1.2.4 Intraperitoneal administration of nanoparticles and drugs.....	15
1.2.5 Peritoneal anatomy and the role of peritoneal macrophages.....	16
1.2.6 Ultrasound and cell sonoporation.....	20
1.3 Challenges and perspectives of MFH in cancer treatment.....	25
1.4 Objectives.....	27
1.5 Overview of the Dissertation.....	28
1.6 References.....	30
<i>Chapter 2.</i> Optimization of synthesis and peptization of magnetic nanoparticles to increase heat dissipation rates.....	42
2.1 Summary.....	42
2.2 Introduction and literature review.....	43
2.3 Experimental section.....	47
2.3.1 Materials.....	48
2.3.2 Synthesis of iron oxide nanoparticles.....	48
2.3.3 Peptization of iron oxide nanoparticles.....	49
2.3.4 Surface modification of nanoparticles.....	49
2.3.5 Nanoparticle characterization.....	50

2.3.5.1	Dynamic light scattering and zeta potential.....	50
2.3.5.2	Dynamic magnetic susceptibility.....	51
2.3.5.3	Magnetic measurements.....	51
2.3.5.4	Iron quantification.....	52
2.3.5.5	Energy dissipation rates and specific absorption rate.....	52
2.3.5.6	Physical diameter.....	54
2.3.5.7	Weight percentage of iron oxide.....	54
2.3.6	Experimental design and statistical analysis.....	54
2.4	Results and discussion .....	56
2.4.1	Particle size.....	56
2.4.2	Magnetic behavior.....	59
2.4.3	SAR measurements in liquid suspensions.....	63
2.4.4	SAR measurements in solid matrices.....	68
2.4.5	Optimization and reproducibility.....	71
2.4.6	Characterization of PEG-coated nanoparticles.....	72
2.5	Conclusions.....	75
2.6	References.....	76
<i>Chapter 3. In vitro ultrasonic potentiation of 2-phenylethanesulfonamide/ magnetic fluid hyperthermia combination treatments for ovarian cancer.....</i>		
3.1	Summary.....	82
3.2	Introduction and literature review.....	83
3.3	Experimental section.....	92
3.3.1	Materials.....	92
3.3.2	Cell cultures.....	92
3.3.3	Cytotoxicity of PEG-coated nanoparticles and Definity® microbubbles.....	93
3.3.3.1	Nanoparticle cytotoxicity.....	93
3.3.3.2	Definity® microbubbles cytotoxicity.....	93
3.3.4	Nanoparticle internalization into ovarian cancer cells.....	94
3.3.4.1	UV/Vis iron quantification.....	94
3.3.4.2	Confocal microscopy.....	95
3.3.5	Focused ultrasound design and calibration.....	95

3.3.6 Optimization of ultrasound parameters for cell sonoporation.....	97
3.3.6.1 Effect of continuous/pulsed ultrasound, intensity and exposure time.....	97
3.3.6.2 Effect of cell numbers at various intensity values.....	97
3.3.7 Assessment of cell membrane permeabilization.....	98
3.3.8 Ultrasound-assisted nanoparticle internalization.....	99
3.3.9 <i>In vitro</i> MFH and combined ultrasound-drug-MFH experiments.....	99
3.3.9.1 PES dose-response curve.....	99
3.3.9.2 US/PES/MFH experiments.....	100
3.4 Results and discussion.....	101
3.4.1 Cytotoxicity of PEG-coated nanoparticles and Definity® microbubbles.....	102
3.4.2 Optimization of ultrasound conditions.....	104
3.4.2.1 Effect of LIFU on cell viability.....	104
3.4.2.2 Effect of LIFU on cell membrane permeability.....	106
3.4.3 Nanoparticle internalization via non-specific uptake.....	108
3.4.4 Ultrasound-assisted nanoparticle internalization.....	111
3.4.5 MFH and ultrasound-assisted PES/MFH combined therapies.....	114
3.4.5.1 Cytotoxicity of MFH and PES as individual treatments.....	114
3.4.5.2 Ultrasound-assisted PES/MFH combined therapies.....	116
3.5 Conclusions.....	122
3.6 References.....	123
<i>Chapter 4. Intraperitoneal administration of magnetic nanoparticles and their uptake by mouse</i> <i>peritoneal macrophages.....</i>	<i>131</i>
4.1. Summary.....	131
4.2. Introduction and literature review.....	133
4.3 Experimental section.....	137
4.3.1 Materials.....	137
4.3.2 Nanoparticles.....	137
4.3.3 Cell cultures and subcutaneous breast cancer xenografts.....	138
4.3.4 Pharmacokinetics and biodistribution.....	138
4.3.5 Isolation of peritoneal cavity cells and iron uptake.....	139
4.4 Results and discussion.....	140
4.4.1 Pharmacokinetics.....	140

4.4.2 Biodistribution.....	142
4.4.3 Nanoparticle accumulation in subcutaneous tumors.....	147
4.4.4 Nanoparticle uptake by peritoneal macrophages.....	149
4.5 Conclusions.....	154
4.6 References.....	154
<i>Chapter 5. Final Remarks: Conclusions and Dissertation Contributions.....</i>	<i>160</i>
Appendix.....	163
A.1 Mapping of acoustic intensity at the target region.....	163
A.2 Comparison of Trypan Blue vs Calcein-AM to determine cell viability.....	165
A.3 Authorization for <i>in vivo</i> experiments issued by IACUC for University of Florida.....	166

## List of Figures

- Figure 1.1** Illustration of Brown and Néel relaxation mechanisms in magnetic nanoparticles exposed to alternating magnetic fields.....8
- Figure 1.2** Schematic representation of passive versus active targeting of tumors, as proposed by Latorre *et al.* Non-targeted nanoparticles accumulate passively via EPR effect, while active targeting is achieved by attaching ligands to the surface of nanoparticles to recognize specific surface receptors in tumor cells.....12
- Figure 1.3** Schematic representation of MFH for cancer treatment, using IV injection, showing subcellular thermal effects.....14
- Figure 1.4** Diagrammatic sagittal view of the human (female) abdominopelvic cavity, showing the localization of the greater and lesser greater omentum. (Reprinted by permission of ©Pearson Education, Inc., New York).....18
- Figure 1.5** Frontal view of the human abdominopelvic cavity, showing the surface anatomy of the greater and lesser omentum. (Reprinted by permission of ©Pearson Education, Inc., New York).....18
- Figure 1.6** Graphical representation of microbubble-mediated cell sonoporation for the enhanced uptake of magnetic nanoparticles and drug molecules.....23
- Figure 2.1** TEM images and size distributions of representative synthesis runs: a) 5B,  $D_p = 15 \pm 0.41$  nm; b) 11B,  $D_p = 12 \pm 0.35$  nm; c) 15B,  $D_p = 20 \text{ nm} \pm 0.40$  nm. Continuous lines represent log-normal size distributions.....57
- Figure 2.2** DLS measurements for the calculation of volume-weighted hydrodynamic diameters for three representative synthesis runs. a) 5B,  $D_h = 38$  nm,  $\text{Ln } \sigma = 0.05$ . b) 11B,  $D_h = 36$  nm,  $\text{Ln } \sigma = 0.08$ . c) 15B,  $D_h = 58$  nm,  $\text{Ln } \sigma = 0.12$ . Continuous lines represent log-normal size distributions.....59
- Figure 2.3** Magnetic characterization for representative synthesis runs. a) Equilibrium magnetization curves showing field dependence at 300K with  $M_s$  values of 109, 104 and 144 emu/g<sub>Fe</sub> for runs 5B, 11B and 15B, respectively. b) ZFC/FC magnetization curves from 4 to 400 K with  $T_B$  values of 264 K for run 5B and higher than 400K for runs 11B and 15B.....60
- Figure 2.4** DMS measurements for two representative synthesis runs with different initial iron concentration. a) Run 9B with iron concentration of 0.08M and  $D_h=32$  nm b) Run 12B with iron concentration of 1.0M and  $D_h=50$  nm. Solid symbols represent individual measurements and continuous lines are fittings to the Langevin-Chantrell model.....62
- Figure 2.5** Parity plot for volume-weighted hydrodynamic diameters obtained from DLS and DMS measurements. Each point represent a single measurement.....63
- Figure 2.6** Examples of temperature rise profiles for various samples exhibiting different heating slopes. Measurements were performed at an applied magnetic field of  $H_o = 36.5$  kA/m and  $f = 341$  kHz. Each point represents a single measurement.....64
- Figure 2.7** Comparison of SAR values of synthesis runs described in Table 2.3. Blue bars: Temperature and sonication at fixed iron concentration. Brown bars: Iron concentration and

sonication at fixed temperature. Orange bars: Temperature and iron concentration at fixed sonication type. Green bars: Temperature, iron concentration and sonication at their medium levels. These three bars are the center points of the experimental design thus describing the overall variability.....66

**Figure 2.8** DMS plot for run 15B comparing data from liquid suspensions (blue markers) and data from particles fixed in agarose gel (brown markers). Each point represents a single measurement.....69

**Figure 2.9** SAR values for particles immobilized in solid matrices. a) Comparison between suspended (blue markers) and agarose-fixed (maroon markers) nanoparticles for the different synthesis runs. b) Comparison of SAR and ILP values between our immobilized particles and those reported by other research groups.....70

**Figure 2.10.** a) Contour plot of the response surface for SAR, b) Evaluation of the predicted behavior of SAR under optimized conditions by means of additional synthesis runs.....72

**Figure 2.11.** Characterization of PEG-coated nanoparticles. a) TEM image;  $D_p = 16$  nm, b) DLS measurements;  $D_h = 50$  nm, c) TGA curves; iron oxide core between 9 and 18%, d) zeta potential measurements at various pH values.....74

**Figure 3.1.** Overview of experimental design for combined ultrasound-drug-magnetic fluid hyperthermia experiments. Acronyms are defined as follows: 2-phenylethanesulfonamide (PES), magnetic fluid hyperthermia (MFH) and ultrasound (US). Response variable is cell viability...102

**Figure 3.2.** Cytotoxicity assessments in three ovarian cancer cell lines for 48 hours. a) PEG-coated nanoparticles. Error bars represent standard deviations of  $n = 18$  of three independent experiments b) Definity® microbubbles. Error bars represent the standard deviation of 3 independent experiments.....104

**Figure 3.3.** Effect of ultrasound experimental conditions on viability of HeyA8 cells. a) effect of pulse type at various acoustic intensities and exposure times. b) effect of cell numbers at various acoustic intensities. Error bars represent the standard deviation of three independent experiments.....107

**Figure 3.4.** Live-cell fluorescence microscopy for the assessment ultrasound-mediated cell membrane permeabilization via Sytox Green uptake by HeyA8 cells. Conditions A to D represent various combinations of  $I_{SPTA}$  values and exposure time. Images show one of four representative areas evaluated per each sample. Error bars represent 500  $\mu\text{m}$ .....109

**Figure 3.5.** Cellular uptake of PEG-coated nanoparticles (0.6  $\text{mg}_{\text{IO}}/\text{mL}$ ) by ovarian cancer cells as quantified by UV/Vis spectroscopy. Error bars represent standard deviations of three independent experiments.....111

**Figure 3.6.** Localization of PEG-coated nanoparticles in SKOV3 cells, via confocal microscopy. a) cells without nanoparticles, b) cells incubated with nanoparticles (0.1  $\text{mg}_{\text{IO}}/\text{mL}$ ) for 1 hour. Nanoparticles, cell membranes and nuclei are depicted by green, red and blue fluorescence, respectively.....111

**Figure 3.7.** Ultrasound-assisted nanoparticle internalization into HeyA8 cells as a function of  $I_{SPTA}$  values | [exposure time] conditions. Cells were incubated with nanoparticles for 5 or 12 hours. Error bars represent the standard deviation of three independent experiments.....113

**Figure 3.8.** Viability ratio of ovarian cancer cells after exposure to MFH and PES. a) AMF ( $H_o = 15 - 20$  kA/m,  $f = 245$  kHz) exposure for 30 min. Control groups represent cells incubated at 37°C, “MNP w/o AMF” group represents cells incubated with MNP in the absence of AMF, and “AMF w/o MNP” represents cells exposed to AMF in the absence of MNP. Error bars represent the standard deviation of three independent experiments. b) Incubation of HeyA8 cells with various PES concentrations for up to 72 hours. Error bars represent the standard deviation of  $n = 6$ .....117

**Figure 3.9.** Viability ratio of HeyA8 cells after combination treatments of ultrasound (US), drug (PES) and hyperthermia (MFH). a) MFH at 41°C and, b) MFH at 43°C. AMF conditions were  $H_o = 15 - 20$  kA/m,  $f = 245$  kHz, exposure time: 30 min. Cells were sonicated twelve hours before AMF exposure. Error bars represent the standard deviation of three independent experiments..119

**Figure 3.10.** Comparison of cell viability upon alternating magnetic fields (AMF) exposure between cells groups with nanoparticles in the bulk medium (MFH at 41°C) and groups with removed nanoparticles (MagMED 37°C). Cells were sonicated (US) 12 hours before AMF exposure ( $H_o = 15 - 20$  kA/m,  $f = 245$  kHz, exposure time = 30 min). Error bars represent the standard deviation of three independent experiments.....121

**Figure 3.11.** Comparison of US/PES/MFH combination therapies with bulk heating at 41°C. Cells were sonicated either 12 hours (solid bars) or 30 minutes (striped bars) before exposure to AMF ( $H_o = 15 - 20$  kA/m,  $f = 245$  kHz, exposure time = 30 min). Error bars represent the standard deviation of three independent experiments.....122

**Figure 4.1** Pharmacokinetics and half-lives of PEG-coated nanoparticles in blood. Hollow circles represent individual replicates and solid squares represent the mean values. Athymic nude mice were injected either, a) intraperitoneally or b) intravenously. Individual replicate values represent independent experiments carried out using 4 and 5 mice for a) and b), respectively.....143

**Figure 4.2.** Biodistribution of PEG-coated nanoparticles in body organs of athymic nude mice injected either intraperitoneally or intravenously. a) Organs with significant nanoparticle accumulation. b) Organs with small nanoparticle accumulation Error bars represent the standard error of independent experiments carried out with four mice.....145

**Figure 4.3** Excised omentum from a mouse, twenty-four hours after IP injection, showing significant nanoparticle accumulation. a) Brown-colored omentum showing high nanoparticle accumulation, b) brightfield micrograph of omental tissues with nanoparticle clusters indicated by yellow arrows.....146

**Figure 4.4** Biodistribution of PEG-coated nanoparticles in body organs and tumor at 3, 6 and 12 hours after IP injection. Error bars represent the standard error of 3 independent experiments.....147

**Figure 4.5** Comparison of nanoparticle accumulation in TNBC xenografts twenty-four hours post injection either a) intravenously, or b) intraperitoneally.....149

**Figure 4.6** Mouse macrophages adhered to non-treated petri dishes, four days after non-elicited isolation from mice. Images were obtained using a 20X objective.....151

**Figure 4.7** Nanoparticle uptake by mouse peritoneal macrophages after IP injection. a) Brighfield microscope image using a 40X objective, b) EPRs spectra of iron oxide internalized into macrophages.....153

**Figure 4.8** Prussian Blue staining of PEG-coated, iron oxide magnetic nanoparticles taken up by mouse peritoneal macrophages. a) Control group -no nanoparticles-, b) Experimental group -nanoparticles injected via IP.....154

**Figure A.1.** Acoustic intensity mapping at the target region,  $f = 1.1$  MHz. a) Horizontally (total diameter of target region is 35 mm). b) Vertically, from the concave plate of transducer.....164

**Figure A.2.** Distribution of acoustic intensity as a function of input voltage, as measured in the target region. Experimental data was fitted to a second-order polynomial model (included)....165

**Figure A.3.** Live cell counts determined by Trypan Blue exclusion (blue bars) compared to metabolically active cells emitting green fluorescence, determined by Calcein-AM staining using image cytometry.....166

## List of tables

<b>Table 1.1</b> Challenges of magnetic nanoparticles and magnetic hyperthermia in cancer treatment.....	26
<b>Table 2.1</b> Summary of studies on SAR maximization.....	43
<b>Table 2.2.</b> Factors and levels for the optimization study.....	55
<b>Table 2.3.</b> Experimental design for the optimization of SAR.....	56
<b>Table 2.4.</b> Colloidal stability of PEG-MNPs in biological media.....	75
<b>Table 3.1.</b> Literature review on <i>in vitro</i> sonoporation-assisted internalization chemotherapeutic drugs.....	89
<b>Table 3.2.</b> Literature review on sonoporation-assisted internalization of magnetic nanoparticles.....	91
<b>Table 3.4.</b> Normalized iron uptake values expressed as the ratio between uptake achieved with ultrasound, divided by that obtained in the absence of ultrasound.....	114
<b>Table 4.1.</b> Delivery efficiency of nanoparticle delivery to tumors with IV injection.....	149

# Development of Optimized Therapeutic Platforms for Magnetic Fluid Hyperthermia in Adjuvant Cancer Therapies

by

*Fernando José Mérida Figueróa*

A dissertation submitted in partial fulfillment of the requirements for the degree of

DOCTOR OF PHILOSOPHY  
In  
CHEMICAL ENGINEERING

UNIVERSITY OF PUERTO RICO  
MAYAGÜEZ CAMPUS

May 2018

Approved by:

\_\_\_\_\_  
Madeline Torres-Lugo, Ph.D.  
President, Graduate Committee

\_\_\_\_\_  
Date

\_\_\_\_\_  
Maribella Domenech, Ph.D.  
Member, Graduate Committee

\_\_\_\_\_  
Date

\_\_\_\_\_  
Eduardo Juan, Ph.D.  
Member, Graduate Committee

\_\_\_\_\_  
Date

\_\_\_\_\_  
Jorge Almodóvar, Ph.D.  
Member, Graduate Committee

\_\_\_\_\_  
Date

\_\_\_\_\_  
Solangie Pagán, Dr. PH  
Graduate Studies Representative

\_\_\_\_\_  
Date

\_\_\_\_\_  
Aldo Acevedo, Ph.D.  
Chair, Department of Chemical Engineering

\_\_\_\_\_  
Date

©Copyright 2018  
Fernando José Mérida Figueróa  
All rights reserved

This dissertation contains portions that were published by the author in the *Journal of Magnetism and Magnetic Materials*

## Abstract

Magnetic Fluid Hyperthermia (MFH) has a great potential as an adjuvant in cancer therapy, enhancing the effects of antineoplastic agents, sensitizing resistant cancers and reducing undesired side effects. When compared to other local hyperthermia approaches, non-specific heating is reduced with MFH since the heat is produced only when alternating magnetic fields are turned on. The clinical translation of MFH faces several challenges including nanoparticle low heat dissipation rates, limited cellular uptake of drugs and/or nanoparticles, and poor nanoparticle accumulation in tumors after intravenous injection. To tackle these challenges, the following hypotheses were proposed: (i) optimization of synthesis and peptization of magnetic nanoparticles will lead to increased heat dissipation rates; (ii) the use of low-intensity ultrasound will improve the cellular uptake of drugs and nanoparticles, potentiating the effects of MFH/drug combination therapies, and (iii) the intraperitoneal administration of nanoparticles will induce their uptake by mouse peritoneal macrophages and tumors. To test these hypotheses, systematic experimental designs were proposed to evaluate nanoparticle properties and their performance *in vitro* and *in vivo*. The coprecipitation synthesis and peptization of iron oxide nanoparticles were optimized, obtaining nanoparticles with remarkably high heat dissipation rates in liquid and solid matrices. Using an *in vitro* ovarian cancer model, increased cytotoxic profile of the drug 2-phenylethanesulfonamide was observed when low-intensity ultrasound was coupled to MFH/drug combination therapies. *In vivo* intraperitoneal administration of nanoparticles did not improve nanoparticle accumulation in subcutaneous breast cancer tumors, but significantly induced uptake by peritoneal macrophages which promoted accumulation in omental tissues. These results demonstrated that optimization of experimental methodologies was key to enhance nanoparticle properties, potentiating novel chemotherapeutic agents and fostering opportunities for improved nanoparticle delivery *in vivo*.

## Resumen

La hipertermia por fluidos magnéticos (MFH) tiene un inmenso potencial como coadyuvante en terapias para cáncer, mejorando los efectos de antineoplásicos, convirtiendo cánceres resistentes en sensibles, y reduciendo efectos secundarios indeseados. Comparada con otras formas de hipertermia local, el calentamiento no específico es reducido con MFH ya que el calor es producido solamente cuando los campos magnéticos externos son activados. La incorporación de MFH en la clínica enfrenta varios retos incluyendo bajas tasas de disipación de calor, limitada internalización de drogas y/o nanopartículas, y poca acumulación de nanopartículas en tumores luego de inyección intravenosa. Para aplacar estos retos, las siguientes hipótesis fueron propuestas; (i) la optimización de síntesis y peptización de nanopartículas magnéticas mejorará la liberación de calor; (ii) el uso de ultrasonido de baja intensidad mejorará la internalización de drogas y nanopartículas, potenciando los efectos de terapias combinadas de MFH/drogas, y (iii) la administración intraperitoneal de nanopartículas inducirá su internalización en macrófagos peritoneales de ratón y en tumores. Para probar estas hipótesis, diseños experimentales sistemáticos fueron propuestos para evaluar propiedades de nanopartículas y su desempeño *in vitro* e *in vivo*. La síntesis por co-precipitación y peptización fueron mejoradas, obteniendo nanopartículas con liberación de calor notablemente altas en preparaciones líquidas y sólidas. Usando un modelo de cáncer de ovario *in vitro*, se observó que el perfil citotóxico de la droga 2-feniletino sulfonamida (PES) aumentó cuando el ultrasonido de baja intensidad fue acoplado a terapias combinadas de MFH/droga. La administración intraperitoneal de nanopartículas *in vivo* no mejoró la acumulación de nanopartículas en tumores subcutáneos de cáncer de seno, pero indujo significativamente la internalización en macrófagos peritoneales, lo cual promovió la acumulación en tejidos del omentum. Estos resultados demostraron que la optimización de metodologías experimentales fue clave para mejorar propiedades de nanopartículas, potenciando agentes quimioterapéuticos novedosos y promoviendo oportunidades para la distribución mejorada de nanopartículas *in vivo*.

## List of publications and conferences

### Publications:

- **Mérida, F.**, Chiu-Lam, A., Bohórquez, Ana C., Maldonado-Camargo, L., Pérez, M.E., Pericchi, L., Torres-Lugo, M., Rinaldi, C. Optimization of synthesis and peptization steps to obtain iron oxide nanoparticles with high energy dissipation rates. *J. Magn. Magn. Mater.* 394, 361-371 (2015).
- Alvarez-Berrios, M. P., Castillo, A., **Mérida, F.**, Mendez, J., Rinaldi, C., Torres-Lugo, M. Enhanced proteotoxic stress: one of the contributors for hyperthermic potentiation of the proteasome inhibitor bortezomib using magnetic nanoparticles. *Biomater. Sci.* 3, 391-400 (2015).

### Oral presentations:

- **Mérida, F.** and Torres-Lugo, M. “Magnetic hyperthermia in cancer treatment”. XXII Latin American Congress of Chemical Engineering (COLAEIQ). Medellín, Colombia. July 2016.
- **Mérida, F.**, Juan, E., Rinaldi, C., Torres-Lugo, M. “Development of optimized strategies for magnetic hyperthermia in the treatment of ovarian cancer”. 36<sup>th</sup> Annual Research and Education Forum. University of Puerto Rico, Medical Sciences Campus. San Juan, PR. March 2016
- **Mérida, F.**, Chiu-Lam, A., Bohórquez, A.C., Maldonado-Camargo, L., Torres-Lugo, M., Rinaldi, C. “Optimized synthesis of high-energy dissipating iron oxide nanoparticles for magnetic hyperthermia in ovarian cancer cells” AIChE Annual Meeting. Salt Lake City, UT. November 2015.

*Dedicated to:*

*My parents*

*JUAN DOMINGO and AURA LEONOR*

*my siblings*

*JOSÉ JUAN and MARÍA JOSÉ*

*For their unconditional love, support and understanding...  
You are my everything.*

*My beautiful GUATEMALA,*

*“The soul of the Earth”*

*Hopefully my work will contribute to its scientific development*

*GOD*

*Who always knows why and how things happen...*

*My friends and every person from whom I have received and shared support, advice and apprenticeship.*

*“A veces, uno espera impaciente por vivir la gran aventura de su vida, quizás sin percatarse que, desde siempre, ha estado viviendo una vida llena de aventura”*

## **Acknowledgements**

This work was possible thanks to the intervention of people whose support was pivotal to accomplish the goals of this doctoral project. First of all, I want to express my gratitude to Dr. Madeline Torres-Lugo for accepting me in her research group, and for all the guidance and support received during the course of this work. My gratitude is also to Dr. Carlos Rinaldi from University of Florida for the extensive mentoring and advice received, and for accepting me as visiting student in his research team.

I want to thank to former and current CBEN members and lab mates. Janet Méndez: Thanks for trainings, ideas, discussions, and all kinds of support. Karem Court and Marisel Sánchez for their help in designing/discussing experiments. Jorge Castro for his help as my “bodyguard” during late night experiments, and for support in graphic design. Nicole Pérez and Tania Ramos for their support. To all of them, thanks for those good lab moments too.

I want to give special thanks to Ana Carolina Bohórquez for being my first mentor in the “nanoworld” and for all the time devoted to train me. My eternal gratitude to Andreina Chiu-Lam for her mentoring in various fields, especially in the work with laboratory animals. Thanks for her unconditional support and commitment in the design and execution of experiments, along with the discussion of results.

Special thanks to the members of my Committee: Dr. Eduardo Juan, Dr. Maribella Domenech and Dr. Jorge Almódovar. Thanks for their feedback, comments and suggestions in this work.

I want to thank to former and current members of the Rinaldi Research Lab: Lorena Maldonado-Camargo, Melissa Cruz-Acuña, Tapomoy Bhattacharjee and Shehaab Savliwala for

their collaboration. To former and current members of BIR Lab: Leonardo Rodríguez-Negrón and Christian Colón for their support in the electrical part of this work.

Thanks to my friends for their support, patience and love, because no matter the distance or the time, they were (and are) always there for me. I will not write down names, though they know I am truly grateful with them.

Finally, I want to acknowledge to the funding agencies that have made this work possible: U.S. National Science Foundation under award # HRD-0833112 and HRD-1345156 (CREST Program), the PR Institute for Functional Nanomaterials (EPS-100241) and the US national Institutes of Health (U54 CA 96300/u54 ca 96297). Also, a special acknowledgement to Lantheus Medical Imaging Inc. for donating the ultrasound contrast agents used in experiments referred in Chapter 3 of this dissertation.

## Table of contents

Abstract.....	III
Resumen.....	IV
List of publications and conferences.....	V
Dedication.....	VI
Acknowledgements.....	VII
List of figures.....	XIII
List of tables.....	XVII
<i>Chapter 1.</i> Introduction.....	1
1.1. Justification.....	1
1.2. Rationale and background.....	4
1.2.1. Magnetic nanoparticles and heat dissipation.....	6
1.2.2 Biological aspects of cancer.....	10
1.2.3 Magnetic Fluid Hyperthermia (MFH).....	13
1.2.4 Intraperitoneal administration of nanoparticles and drugs.....	15
1.2.5 Peritoneal anatomy and the role of peritoneal macrophages.....	16
1.2.6 Ultrasound and cell sonoporation.....	20
1.3 Challenges and perspectives of MFH in cancer treatment.....	25
1.4 Objectives.....	27
1.5 Overview of the Dissertation.....	28
1.6 References.....	30
<i>Chapter 2.</i> Optimization of synthesis and peptization of magnetic nanoparticles to increase heat dissipation rates.....	42
2.1 Summary.....	42
2.2 Introduction and literature review.....	43
2.3 Experimental section.....	47
2.3.1 Materials.....	48
2.3.2 Synthesis of iron oxide nanoparticles.....	48
2.3.3 Peptization of iron oxide nanoparticles.....	49
2.3.4 Surface modification of nanoparticles.....	49
2.3.5 Nanoparticle characterization.....	50

2.3.5.1	Dynamic light scattering and zeta potential.....	50
2.3.5.2	Dynamic magnetic susceptibility.....	51
2.3.5.3	Magnetic measurements.....	51
2.3.5.4	Iron quantification.....	52
2.3.5.5	Energy dissipation rates and specific absorption rate.....	52
2.3.5.6	Physical diameter.....	54
2.3.5.7	Weight percentage of iron oxide.....	54
2.3.6	Experimental design and statistical analysis.....	54
2.4	Results and discussion .....	56
2.4.1	Particle size.....	56
2.4.2	Magnetic behavior.....	59
2.4.3	SAR measurements in liquid suspensions.....	63
2.4.4	SAR measurements in solid matrices.....	68
2.4.5	Optimization and reproducibility.....	71
2.4.6	Characterization of PEG-coated nanoparticles.....	72
2.5	Conclusions.....	75
2.6	References.....	76
<i>Chapter 3. In vitro ultrasonic potentiation of 2-phenylethanesulfonamide/ magnetic fluid hyperthermia combination treatments for ovarian cancer.....</i>		
3.1	Summary.....	82
3.2	Introduction and literature review.....	83
3.3	Experimental section.....	92
3.3.1	Materials.....	92
3.3.2	Cell cultures.....	92
3.3.3	Cytotoxicity of PEG-coated nanoparticles and Definity® microbubbles.....	93
3.3.3.1	Nanoparticle cytotoxicity.....	93
3.3.3.2	Definity® microbubbles cytotoxicity.....	93
3.3.4	Nanoparticle internalization into ovarian cancer cells.....	94
3.3.4.1	UV/Vis iron quantification.....	94
3.3.4.2	Confocal microscopy.....	95
3.3.5	Focused ultrasound design and calibration.....	95

3.3.6 Optimization of ultrasound parameters for cell sonoporation.....	97
3.3.6.1 Effect of continuous/pulsed ultrasound, intensity and exposure time.....	97
3.3.6.2 Effect of cell numbers at various intensity values.....	97
3.3.7 Assessment of cell membrane permeabilization.....	98
3.3.8 Ultrasound-assisted nanoparticle internalization.....	99
3.3.9 <i>In vitro</i> MFH and combined ultrasound-drug-MFH experiments.....	99
3.3.9.1 PES dose-response curve.....	99
3.3.9.2 US/PES/MFH experiments.....	100
3.4 Results and discussion.....	101
3.4.1 Cytotoxicity of PEG-coated nanoparticles and Definity® microbubbles.....	102
3.4.2 Optimization of ultrasound conditions.....	104
3.4.2.1 Effect of LIFU on cell viability.....	104
3.4.2.2 Effect of LIFU on cell membrane permeability.....	106
3.4.3 Nanoparticle internalization via non-specific uptake.....	108
3.4.4 Ultrasound-assisted nanoparticle internalization.....	111
3.4.5 MFH and ultrasound-assisted PES/MFH combined therapies.....	114
3.4.5.1 Cytotoxicity of MFH and PES as individual treatments.....	114
3.4.5.2 Ultrasound-assisted PES/MFH combined therapies.....	116
3.5 Conclusions.....	122
3.6 References.....	123
<i>Chapter 4. Intraperitoneal administration of magnetic nanoparticles and their uptake by mouse</i>	
peritoneal macrophages.....	131
4.1. Summary.....	131
4.2. Introduction and literature review.....	133
4.3 Experimental section.....	137
4.3.1 Materials.....	137
4.3.2 Nanoparticles.....	137
4.3.3 Cell cultures and subcutaneous breast cancer xenografts.....	138
4.3.4 Pharmacokinetics and biodistribution.....	138
4.3.5 Isolation of peritoneal cavity cells and iron uptake.....	139
4.4 Results and discussion.....	140
4.4.1 Pharmacokinetics.....	140

4.4.2 Biodistribution.....	142
4.4.3 Nanoparticle accumulation in subcutaneous tumors.....	147
4.4.4 Nanoparticle uptake by peritoneal macrophages.....	149
4.5 Conclusions.....	154
4.6 References.....	154
<i>Chapter 5. Final Remarks: Conclusions and Dissertation Contributions.....</i>	<i>160</i>
Appendix.....	163
A.1 Mapping of acoustic intensity at the target region.....	163
A.2 Comparison of Trypan Blue vs Calcein-AM to determine cell viability.....	165
A.3 Authorization for <i>in vivo</i> experiments issued by IACUC for University of Florida.....	166

## List of Figures

- Figure 1.1** Illustration of Brown and Néel relaxation mechanisms in magnetic nanoparticles exposed to alternating magnetic fields.....8
- Figure 1.2** Schematic representation of passive versus active targeting of tumors, as proposed by Latorre *et al.* Non-targeted nanoparticles accumulate passively via EPR effect, while active targeting is achieved by attaching ligands to the surface of nanoparticles to recognize specific surface receptors in tumor cells.....12
- Figure 1.3** Schematic representation of MFH for cancer treatment, using IV injection, showing subcellular thermal effects.....14
- Figure 1.4** Diagrammatic sagittal view of the human (female) abdominopelvic cavity, showing the localization of the greater and lesser greater omentum. (Reprinted by permission of ©Pearson Education, Inc., New York).....18
- Figure 1.5** Frontal view of the human abdominopelvic cavity, showing the surface anatomy of the greater and lesser omentum. (Reprinted by permission of ©Pearson Education, Inc., New York).....18
- Figure 1.6** Graphical representation of microbubble-mediated cell sonoporation for the enhanced uptake of magnetic nanoparticles and drug molecules.....23
- Figure 2.1** TEM images and size distributions of representative synthesis runs: a) 5B,  $D_p = 15 \pm 0.41$  nm; b) 11B,  $D_p = 12 \pm 0.35$  nm; c) 15B,  $D_p = 20 \text{ nm} \pm 0.40$  nm. Continuous lines represent log-normal size distributions.....57
- Figure 2.2** DLS measurements for the calculation of volume-weighted hydrodynamic diameters for three representative synthesis runs. a) 5B,  $D_h = 38$  nm,  $\text{Ln } \sigma = 0.05$ . b) 11B,  $D_h = 36$  nm,  $\text{Ln } \sigma = 0.08$ . c) 15B,  $D_h = 58$  nm,  $\text{Ln } \sigma = 0.12$ . Continuous lines represent log-normal size distributions.....59
- Figure 2.3** Magnetic characterization for representative synthesis runs. a) Equilibrium magnetization curves showing field dependence at 300K with  $M_s$  values of 109, 104 and 144 emu/g<sub>Fe</sub> for runs 5B, 11B and 15B, respectively. b) ZFC/FC magnetization curves from 4 to 400 K with  $T_B$  values of 264 K for run 5B and higher than 400K for runs 11B and 15B.....60
- Figure 2.4** DMS measurements for two representative synthesis runs with different initial iron concentration. a) Run 9B with iron concentration of 0.08M and  $D_h=32$  nm b) Run 12B with iron concentration of 1.0M and  $D_h=50$  nm. Solid symbols represent individual measurements and continuous lines are fittings to the Langevin-Chantrell model.....62
- Figure 2.5** Parity plot for volume-weighted hydrodynamic diameters obtained from DLS and DMS measurements. Each point represent a single measurement.....63
- Figure 2.6** Examples of temperature rise profiles for various samples exhibiting different heating slopes. Measurements were performed at an applied magnetic field of  $H_o = 36.5$  kA/m and  $f = 341$  kHz. Each point represents a single measurement.....64
- Figure 2.7** Comparison of SAR values of synthesis runs described in Table 2.3. Blue bars: Temperature and sonication at fixed iron concentration. Brown bars: Iron concentration and

sonication at fixed temperature. Orange bars: Temperature and iron concentration at fixed sonication type. Green bars: Temperature, iron concentration and sonication at their medium levels. These three bars are the center points of the experimental design thus describing the overall variability.....66

**Figure 2.8** DMS plot for run 15B comparing data from liquid suspensions (blue markers) and data from particles fixed in agarose gel (brown markers). Each point represents a single measurement.....69

**Figure 2.9** SAR values for particles immobilized in solid matrices. a) Comparison between suspended (blue markers) and agarose-fixed (maroon markers) nanoparticles for the different synthesis runs. b) Comparison of SAR and ILP values between our immobilized particles and those reported by other research groups.....70

**Figure 2.10.** a) Contour plot of the response surface for SAR, b) Evaluation of the predicted behavior of SAR under optimized conditions by means of additional synthesis runs.....72

**Figure 2.11.** Characterization of PEG-coated nanoparticles. a) TEM image;  $D_p = 16$  nm, b) DLS measurements;  $D_h = 50$  nm, c) TGA curves; iron oxide core between 9 and 18%, d) zeta potential measurements at various pH values.....74

**Figure 3.1.** Overview of experimental design for combined ultrasound-drug-magnetic fluid hyperthermia experiments. Acronyms are defined as follows: 2-phenylethanesulfonamide (PES), magnetic fluid hyperthermia (MFH) and ultrasound (US). Response variable is cell viability...102

**Figure 3.2.** Cytotoxicity assessments in three ovarian cancer cell lines for 48 hours. a) PEG-coated nanoparticles. Error bars represent standard deviations of  $n = 18$  of three independent experiments b) Definity® microbubbles. Error bars represent the standard deviation of 3 independent experiments.....104

**Figure 3.3.** Effect of ultrasound experimental conditions on viability of HeyA8 cells. a) effect of pulse type at various acoustic intensities and exposure times. b) effect of cell numbers at various acoustic intensities. Error bars represent the standard deviation of three independent experiments.....107

**Figure 3.4.** Live-cell fluorescence microscopy for the assessment ultrasound-mediated cell membrane permeabilization via Sytox Green uptake by HeyA8 cells. Conditions A to D represent various combinations of  $I_{SPTA}$  values and exposure time. Images show one of four representative areas evaluated per each sample. Error bars represent 500  $\mu\text{m}$ .....109

**Figure 3.5.** Cellular uptake of PEG-coated nanoparticles (0.6  $\text{mg}_{\text{IO}}/\text{mL}$ ) by ovarian cancer cells as quantified by UV/Vis spectroscopy. Error bars represent standard deviations of three independent experiments.....111

**Figure 3.6.** Localization of PEG-coated nanoparticles in SKOV3 cells, via confocal microscopy. a) cells without nanoparticles, b) cells incubated with nanoparticles (0.1  $\text{mg}_{\text{IO}}/\text{mL}$ ) for 1 hour. Nanoparticles, cell membranes and nuclei are depicted by green, red and blue fluorescence, respectively.....111

**Figure 3.7.** Ultrasound-assisted nanoparticle internalization into HeyA8 cells as a function of  $I_{SPTA}$  values | [exposure time] conditions. Cells were incubated with nanoparticles for 5 or 12 hours. Error bars represent the standard deviation of three independent experiments.....113

**Figure 3.8.** Viability ratio of ovarian cancer cells after exposure to MFH and PES. a) AMF ( $H_o = 15 - 20$  kA/m,  $f = 245$  kHz) exposure for 30 min. Control groups represent cells incubated at 37°C, “MNP w/o AMF” group represents cells incubated with MNP in the absence of AMF, and “AMF w/o MNP” represents cells exposed to AMF in the absence of MNP. Error bars represent the standard deviation of three independent experiments. b) Incubation of HeyA8 cells with various PES concentrations for up to 72 hours. Error bars represent the standard deviation of  $n = 6$ .....117

**Figure 3.9.** Viability ratio of HeyA8 cells after combination treatments of ultrasound (US), drug (PES) and hyperthermia (MFH). a) MFH at 41°C and, b) MFH at 43°C. AMF conditions were  $H_o = 15 - 20$  kA/m,  $f = 245$  kHz, exposure time: 30 min. Cells were sonicated twelve hours before AMF exposure. Error bars represent the standard deviation of three independent experiments..119

**Figure 3.10.** Comparison of cell viability upon alternating magnetic fields (AMF) exposure between cells groups with nanoparticles in the bulk medium (MFH at 41°C) and groups with removed nanoparticles (MagMED 37°C). Cells were sonicated (US) 12 hours before AMF exposure ( $H_o = 15 - 20$  kA/m,  $f = 245$  kHz, exposure time = 30 min). Error bars represent the standard deviation of three independent experiments.....121

**Figure 3.11.** Comparison of US/PES/MFH combination therapies with bulk heating at 41°C. Cells were sonicated either 12 hours (solid bars) or 30 minutes (striped bars) before exposure to AMF ( $H_o = 15 - 20$  kA/m,  $f = 245$  kHz, exposure time = 30 min). Error bars represent the standard deviation of three independent experiments.....122

**Figure 4.1** Pharmacokinetics and half-lives of PEG-coated nanoparticles in blood. Hollow circles represent individual replicates and solid squares represent the mean values. Athymic nude mice were injected either, a) intraperitoneally or b) intravenously. Individual replicate values represent independent experiments carried out using 4 and 5 mice for a) and b), respectively.....143

**Figure 4.2.** Biodistribution of PEG-coated nanoparticles in body organs of athymic nude mice injected either intraperitoneally or intravenously. a) Organs with significant nanoparticle accumulation. b) Organs with small nanoparticle accumulation Error bars represent the standard error of independent experiments carried out with four mice.....145

**Figure 4.3** Excised omentum from a mouse, twenty-four hours after IP injection, showing significant nanoparticle accumulation. a) Brown-colored omentum showing high nanoparticle accumulation, b) brightfield micrograph of omental tissues with nanoparticle clusters indicated by yellow arrows.....146

**Figure 4.4** Biodistribution of PEG-coated nanoparticles in body organs and tumor at 3, 6 and 12 hours after IP injection. Error bars represent the standard error of 3 independent experiments.....147

**Figure 4.5** Comparison of nanoparticle accumulation in TNBC xenografts twenty-four hours post injection either a) intravenously, or b) intraperitoneally.....149

**Figure 4.6** Mouse macrophages adhered to non-treated petri dishes, four days after non-elicited isolation from mice. Images were obtained using a 20X objective.....151

**Figure 4.7** Nanoparticle uptake by mouse peritoneal macrophages after IP injection. a) Brighfield microscope image using a 40X objective, b) EPRs spectra of iron oxide internalized into macrophages.....153

**Figure 4.8** Prussian Blue staining of PEG-coated, iron oxide magnetic nanoparticles taken up by mouse peritoneal macrophages. a) Control group -no nanoparticles-, b) Experimental group -nanoparticles injected via IP.....154

**Figure A.1.** Acoustic intensity mapping at the target region,  $f = 1.1$  MHz. a) Horizontally (total diameter of target region is 35 mm). b) Vertically, from the concave plate of transducer.....164

**Figure A.2.** Distribution of acoustic intensity as a function of input voltage, as measured in the target region. Experimental data was fitted to a second-order polynomial model (included)....165

**Figure A.3.** Live cell counts determined by Trypan Blue exclusion (blue bars) compared to metabolically active cells emitting green fluorescence, determined by Calcein-AM staining using image cytometry.....166

## List of tables

<b>Table 1.1</b> Challenges of magnetic nanoparticles and magnetic hyperthermia in cancer treatment.....	26
<b>Table 2.1</b> Summary of studies on SAR maximization.....	43
<b>Table 2.2.</b> Factors and levels for the optimization study.....	55
<b>Table 2.3.</b> Experimental design for the optimization of SAR.....	56
<b>Table 2.4.</b> Colloidal stability of PEG-MNPs in biological media.....	75
<b>Table 3.1.</b> Literature review on <i>in vitro</i> sonoporation-assisted internalization chemotherapeutic drugs.....	89
<b>Table 3.2.</b> Literature review on sonoporation-assisted internalization of magnetic nanoparticles.....	91
<b>Table 3.4.</b> Normalized iron uptake values expressed as the ratio between uptake achieved with ultrasound, divided by that obtained in the absence of ultrasound.....	114
<b>Table 4.1.</b> Delivery efficiency of nanoparticle delivery to tumors with IV injection.....	149

# Chapter 1

## *Introduction*

---

### **1.1 Justification**

Hyperthermia makes use of thermal energy to treat malignant tumors due to higher susceptibility of cancer cells to heat stresses when compared to their healthy counterparts<sup>1</sup>. The pursuit of alternative cancer therapies has led to hyperthermia to stand out as a promising adjuvant in cancer treatment, enhancing the effects of both chemotherapy and radiotherapy<sup>2</sup>. Various platforms to produce heat have been proposed to achieve local hyperthermia in cancer treatment. Most of these approaches lack the specificity to deliver the heat only to tumors thus leading to undesired effects in healthy tissues<sup>3</sup>. Magnetic Fluid Hyperthermia (MFH), as a local, minimally invasive hyperthermia approach, uses heat produced by magnetic nanoparticles when exposed to alternating magnetic fields. When compared to other local hyperthermia techniques, MFH reduces non-specific heating because heat generation occurs only when the magnetic field is turned on<sup>3,4</sup>. In addition to potentiate the effects of several chemotherapeutic drugs, it has been demonstrated that MFH induces the sensitization of multidrug resistant cancer cell lines both *in vitro* and *in vivo*<sup>2,5,6</sup>. Bare iron oxide magnetic nanoparticles have been reported as generally non-toxic at low concentrations<sup>7</sup>, however, even when coated with biocompatible polymers<sup>8</sup>, concerns exist about long-term toxicity, *in vivo*, at high concentrations<sup>9</sup>. For this reason, the use of the lowest nanoparticle dose is preferred *in vivo*, but magnetic nanoparticles must dissipate sufficient heat to compensate the low dose, and efficiently accumulate in the tumor to avoid non-specific heating<sup>10</sup>. To tackle this challenge, a good number of studies aiming to increase the heat

dissipation rates of nanoparticles is available in the literature. Most of these studies use complex fractionation techniques involving toxic solvents to tune particle shape and/or physical interactions<sup>11-13</sup>.

In MFH adjuvant cancer therapy, it is required that both nanoparticles and chemotherapeutic drugs efficiently accumulate in tumors and not in non-cancerous tissues. This continues to be a major drawback of chemotherapy. Therefore, there is a need for improvements in these therapies. In the case of nanoparticles, most researchers have opted for the use of targeting ligands to improve their uptake by cancer cells<sup>14</sup>. However, nanotechnology-based active targeting is a complex and expensive approach, with decreased blood circulation times due to immunogenicity thus leading to reduced accumulation in the tumor<sup>15</sup>. Other methods including low-intensity ultrasound, have been studied to improve either drug or nanoparticle uptake by cancer cells<sup>16-18</sup>. In the case of nanoparticles, such methods have been used mainly for imaging purposes. Investigations on how ultrasound-enhanced drug and/or nanoparticle internalization patterns, either individual or together, would enhance MFH adjuvant cancer therapy have not been conducted yet.

The route of administration of magnetic nanoparticles dictates the fate of nanoparticles *in vivo*. The intravenous (IV) administration of nanoparticles, either targeted or non-targeted, is the most widely used route of administration. Yet, it has been reported to have low delivery efficiencies, with very small percentages of the injected doses reaching tumors<sup>19</sup>. Nanoparticle sequestration by blood phagocytes is the main contributor for such low delivery efficiencies, therefore alternative routes of administration have been proposed, including the intraperitoneal (IP) route. Nanoparticle recognition by peritoneal phagocytes can be advantageous when nanoparticles are administered via IP, because phagocytes could transport nanoparticles to sites

where intraperitoneal cancers develop<sup>20</sup>. Notably, the interaction of immune cells with inflammatory cancer cells in the subperitoneal space would support the progression of cancer metastases.

Motivated for a need to overcome some of the challenges that MFH currently faces as an adjuvant cancer therapy, three challenges were identified in this work with potential improvement opportunities. Such challenges were chosen based on previous work of our research group along with those often mentioned in the literature and discussed earlier in this section. Therefore, this work presents relevant findings on three areas: i) optimization of nanoparticle synthesis to increase heat dissipation rates, ii) improvements on nanoparticle/drug internalization for enhanced MFH *in vitro*, iii) improvements on nanoparticle uptake by immune cells *in vivo*. Results demonstrated that optimal synthesis conditions were found to produce magnetic nanoparticles with outstanding heating profiles, using a simple, cost-efficient and reproducible method. The effect of low-intensity ultrasound was also studied to improve the effects of MFH combined with the drug 2-phenylethanesulfonamide (PES), and results indicated that enhanced cancer cell killing profiles can be achieved when nanoparticle/drug mixture were sonicated at various experimental conditions. In addition, the potential of intraperitoneal (IP) administration of nanoparticles *in vivo* was also investigated and compared to IV injection. It was found that IP administration led to notable nanoparticle uptake by peritoneal macrophages with subsequent transport to the omentum, where high nanoparticle accumulation was found. Results obtained in this work confirmed the importance of optimization during nanoparticle synthesis, the benefits of ultrasound when used along with combined MFH/drug in the treatment of ovarian cancer *in vitro*, and the potential of IP nanoparticle injection *in vivo* to target peritoneal macrophages. Together, these results are of utmost importance in the field of

nanoscale thermal cancer therapy, and it is expected they serve as motivation to pursue additional investigations in this field.

## **1.2 Rationale and background**

One of the greatest concerns in public health is the prevalence of cancer as the second cause of death worldwide, with 1 in 6 deaths due to cancer-related issues, and new cases are expected to increase by about 70% in the next twenty years<sup>21</sup>. In the United States, breast and ovarian cancers are included in the top five deadliest cancers among women, with 255,180 and 22,440 new cases, respectively, as estimated in 2017<sup>22</sup>. Among gynecological malignancies, ovarian cancer is the most lethal and is considered a “silent killer” since there are no early symptoms, resulting in late diagnosis at advanced stages of the disease<sup>23</sup>. In the case of breast cancer for example, easier detection methods that have become routine in women, has resulted in an overall decreased number of deaths over the past three decades when compared to other cancers such as ovarian cancer. The latter is true except for triple-negative breast cancer (TNBC) which is defined as a type of breast cancer that does not express the estrogen, progesterone, and human epidermal growth factor receptor 2 (HER2) gene receptors. The lack of expression of these genes leads to endocrine- or targeted-based therapies to fail in the treatment, thus less options are available when compared to hormone receptor positive breast cancers<sup>24</sup>. These characteristics make TNBC types more aggressive, with increased relapse patterns and affecting young women. Mammography-based breast cancer diagnostics is not a routine practice among young women thus TNBC is serious threat for young populations<sup>25</sup>.

The standard of care for both ovarian and breast cancers in most circumstances include “debulking” surgery as the initial step during therapy. Surgery is then followed by chemotherapy

in ovarian cancer and chemo/radiotherapy in the case of TNBC<sup>26,27</sup>. Depending on the specific type of cancer and its stage, age and health condition of the patient, and other factors, chemotherapy can also be applied before surgery (neoadjuvant therapy) to shrink the tumor, thus making cytoreductive surgery less extensive. IV chemotherapy for ovarian cancer currently includes a combination of cisplatin or carboplatin along with paclitaxel, administered every three weeks<sup>28</sup>. Radiotherapy following surgery in TNBC is still a common practice, as it is the administration of platinum compounds with taxanes. First- and second-line therapies of TNBC frequently include cisplatin/carboplatin plus gemcitabine or carboplatin plus paclitaxel<sup>27</sup>. Unfortunately, even when most of patients are initially responsive to these combinations, they will eventually become resistant to chemotherapy. Hence, drug resistance remains a major obstacle in the standard of care of these two cancers, promoting recurrence and reducing patient survival. In fact, attempting to improve the prognosis of patients with ovarian cancer is a real challenge because of drug resistance, and the survival rate has not improved over the past 20 years<sup>29</sup>. It is evident that new strategies are necessary to circumvent issues associated to drug resistance, and one of them is the use of heat to increase the physiological temperature of a tumor in the range 41 - 47°C<sup>30</sup>. The rationale behind this approach, known as hyperthermia, is the higher susceptibility of cancer cells to heat when compared to healthy cells. Hyperthermia is an ancient technique, and it was not implemented in the clinic until a few decades ago using three modalities: local, regional, and whole body hyperthermia<sup>31</sup>. While whole body and regional hyperthermia would seem as useful approaches for metastases and deep-seated tumors, unwanted side effects and complex heat application techniques remain as challenges<sup>3</sup>. Local hyperthermia allows for the focused treatment of tumors in smaller areas using simpler applicators, including radiofrequency, microwave, ultrasound, hot water tubes, laser fibers, and others<sup>32</sup>. Some of these

methods are often invasive, with non-uniform heat distribution or lacking specificity to tumors. An alternative that is tumor focused, minimally invasive, and capable to deliver heat at the nanoscale is the so-called magnetic fluid hyperthermia (MFH). The rationale behind MFH is the production of heat when magnetic nanoparticles are exposed to alternating magnetic fields, which is then used to induce a temperature rise in tumors<sup>32</sup>. Conversely to traditional hyperthermia, MFH produces heat only during the application of external magnetic fields, thus non-specific heating of healthy tissues is greatly reduced<sup>3</sup>. Additional advantages of MFH include the potentiation of chemotherapeutic drugs and chemosensitization of multidrug resistance cancer cell lines<sup>2,5</sup>. Therefore, MFH is an important nanotechnology-based hyperthermia approach, with multiple advantages over traditional hyperthermia and potential to become a successful adjuvant in cancer therapy.

### **1.2.1 Magnetic nanoparticles and heat dissipation**

The distinctive advantages of MFH over other techniques of local hyperthermia rely on magnetic nanoparticles and their properties. With diameters ranging between 5 and 500 nm, magnetic nanoparticles for biomedical applications consist of a magnetic core, usually iron oxides, and a functional coating. At the nanoscale, magnetic particles exhibit unique properties that are not observed for sizes other than nano. One of these properties is the superparamagnetic behavior which is characterized by magnetization which can randomly flip the direction of particles under the influence of temperature<sup>47</sup>. Superparamagnetism occurs when nanoparticles are composed of a single magnetic domain, which is possible for particle sizes below ~50 nm for iron oxide (magnetite)<sup>48</sup>. Upon the application of an external magnetic field, superparamagnetic nanoparticles tend to align along its direction, leading to a net magnetization. When the magnetic field is withdrawn the dipoles are randomly oriented leading to no net magnetization<sup>49</sup>. The most

widely used and studied magnetic nanoparticles are those made of the so-called iron oxides (magnetite and maghemite) due to their apparent lack of toxicity and biocompatibility<sup>2,50</sup>. Iron oxide nanoparticles can be chemically synthesized using various methods, including those of co-precipitation and thermal decomposition as the most commonly used and reported in the literature<sup>51</sup>. The co-precipitation of iron salts in aqueous media under an inert atmosphere, attributed to Massart<sup>52</sup>, is the preferred method because it yields substantial amounts of nanoparticles per synthesis batch. Experimental conditions including temperature, iron concentrations, surfactants, pH, ionic strength, and others, can be varied during co-precipitation synthesis to control nanoparticle size and shape<sup>53,54</sup>. Iron oxide nanoparticles synthesized by co-precipitation are inherently unstable and tend to spontaneously aggregate to minimize their high surface energies<sup>55</sup>. Colloidal stability represents the capacity of nanoparticles to remain well suspended in biological media without aggregations. Usually, the attractive forces between nanoparticles are inevitable, thus their surface must be modified to provide steric and electrostatic repulsive interactions, improving their dispersion in liquid media. Among these polymers, the most widely used include poly-ethylene glycol (PEG), poly-vinyl alcohol (PVA), chitosan, dextran and carboxymethyl dextran (CMDx)<sup>43</sup>. In addition, surface coating can also be used to anchor other molecules to provide the particle with a specific function. These functions include targeting ligands, drugs, fluorophores, nucleic acids, and others.

The energy dissipation mechanisms of magnetic nanoparticles in an alternating magnetic field are due to magnetic losses. These mechanisms can be attributed to two different phenomena: hysteresis and relaxation<sup>56</sup>. In theory, perfectly superparamagnetic nanoparticles do not have hysteresis loop, thus the predominant contribution to heat dissipation is caused by the delay in the relaxation of the magnetic moment<sup>57</sup>. Such delay can be by any of two types: Néel

and Brown mechanisms. Néel relaxation occurs when the internal dipole rotates inside the magnetic core against an energy barrier called magnetocrystalline anisotropy<sup>58</sup>. Brownian relaxation refers to the physical rotation of particles due to the alignment of dipoles with the magnetic field, and this mechanism is hindered by the viscosity that tends to counter the movement of particles in the medium, producing heat<sup>59</sup>. These mechanisms are depicted in Figure 1.1 The mechanism having the shorter relaxation time will be the dominant one, but it is important to consider that when the particle size distribution is wide, there will be a dual contribution of the two relaxation mechanisms to the total amount of heat dissipated.

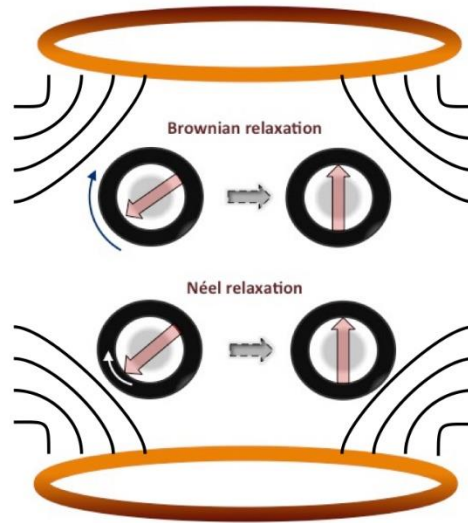


**Figure 1.1** Illustration of Brown and Néel relaxation mechanisms in magnetic nanoparticles exposed to alternating magnetic fields

The specific absorption rate (SAR), is the parameter utilized to estimate the rate of heat dissipated by the nanoparticles per unit mass of magnetic material. SAR represents the rate at

which a unit mass of biological material absorbs the electromagnetic energy. SAR is dependent on magnetic field parameters such as frequency and intensity, and also on the properties of nanoparticles such as particle size/shape, magnetic behavior, composition, and others<sup>60</sup>. SAR measurements must be performed in adiabatic conditions to avoid heat losses to the environment<sup>61</sup>. In other words, the temperature of the nanoparticle sample must equal the temperature of the surroundings when measurements start. SAR can be calculated using equation (1):

$$SAR = C_P \frac{m_s}{m_{Fe}} \frac{\Delta T}{\Delta t} \Big|_{t \rightarrow 0} \quad (1)$$

where  $m_s$  is the mass of the sample solution,  $m_{Fe}$  is the mass of iron in the sample,  $C_P$  is the heat capacity of the solvent, and  $\Delta T/\Delta t$  is the initial slope of the time-dependent heating curve. To avoid ambiguity, the SAR value can be normalized by the frequency and the intensity of the applied magnetic field, thus allowing for comparisons between different research groups. The normalized system-independent parameter is called intrinsic loss power (ILP) and it is represented by equation (2)<sup>62</sup>:

$$ILP = \frac{SAR}{H^2 f} \quad (2)$$

where  $H$  is the magnetic field intensity and  $f$  is the frequency at which calorimetric measurements are performed. As mentioned earlier in this chapter, increasing the heat dissipation rates of nanoparticles is required to achieve more efficient heating of tumors or intracellular compartments using the lowest nanoparticle concentration. In addition, it is known that when nanoparticles are injected via intravenous, only a small percentage of the original injected dose reach tumors<sup>19</sup>, thus SAR values must be as high as possible to reach therapeutic temperatures.

Efforts to increase SAR by tuning nanoparticle properties have increased in the last decade, and among these properties, nanoparticle size and shape have been studied. For example, nanoparticle shape including cubes, chain-like aggregates and “nanoflower” geometries have been reported with high heat dissipation rates<sup>63-65</sup>, most likely due to increased anisotropy and energy of magnetic dipole-dipole presumably larger than thermal energy<sup>66</sup>. A detailed literature review of studies aiming to increase SAR values of magnetic nanoparticles using various methods is presented in chapter 2 of this dissertation.

### **1.2.2 Biological aspects of cancer**

In order to understand the role of magnetic nanoparticles in MFH as a cancer treatment, it is important to review fundamental concepts about cancer. From basic definitions, cancer is the name given to a wide range of diseases characterized by accelerated and unregulated cell growth patterns<sup>33</sup>. Due to this uncontrolled growth, cells can form malignant neoplasms commonly called “tumors” which invade nearby parts of the body or even spread to other organs in the body (metastasis). In a tumor, different type of cells are present including fibroblasts, carcinoma-associated fibroblasts, tumor-associated macrophages, myofibroblasts, smooth muscle cells, endothelial cells, pericytes, neutrophils, eosinophils, basophils, etc.<sup>34</sup>

The tumor microenvironment is quite complicated. Inflammation causes “wounds that do not heal”<sup>33</sup>, speeding the cell cycle, preventing cell death and lately, increasing the size of the tumor. Such environment is characterized by vasculature with irregular architecture, poor lymphatic drainage, and the upregulation of growth factors that increase cell permeability<sup>35</sup>. Since the vasculature of a tumor is abnormal, inadequate blood supply towards the center of the tumor occurs which leads to very low oxygen concentrations (hypoxia). This condition affects the

delivery of chemotherapeutic drugs administered via IV therefore limiting efficacy of chemotherapy.

Defective endothelial cells of blood vessels in tumors have open fenestrations of 200 – 2000 nm<sup>36</sup>. Such gaps, along with the poor lymphatic drainage, promotes the accumulation and retention of nano-sized agents and macromolecular drugs inside the tumor. This phenomenon is known as the enhanced permeability and retention (EPR) effect and is the key for the transport and delivery of macromolecular chemotherapeutic drugs and particularly attractive for the delivery of nanoparticles<sup>37,38</sup>. Nanoparticles injected via IV circulate through the bloodstream and then extravasate from tumor vasculature and accumulate in the interstitial fluid. Furthermore, they are retained inside the tumor. This approach, used in nanotechnology-based cancer therapies is known as passive targeting, and it is the responsible for efficient delivery of nanoparticles to tumors<sup>39</sup>. Studies in animal models have shown that the time required to achieve an EPR effect could be several hours in circulation and the retention time for macromolecular drugs could be several days<sup>40</sup>. This is the reason why nanoparticles with long circulation times are preferred when using passive targeting. Also, the use of particles with neutral charge avoids rapid elimination by the liver<sup>41</sup>. To increase the accumulation and specificity of nanoparticles for cancer cells in tumors, the surface of particles can be loaded with ligands to target some receptors, often overexpressed in cancer cells. This approach is called active targeting<sup>42</sup>. Figure 1.2 shows a schematic depiction of the tumor microenvironment along with the active and passive nanoparticle targeting of tumors, as proposed by Latorre *et al.*

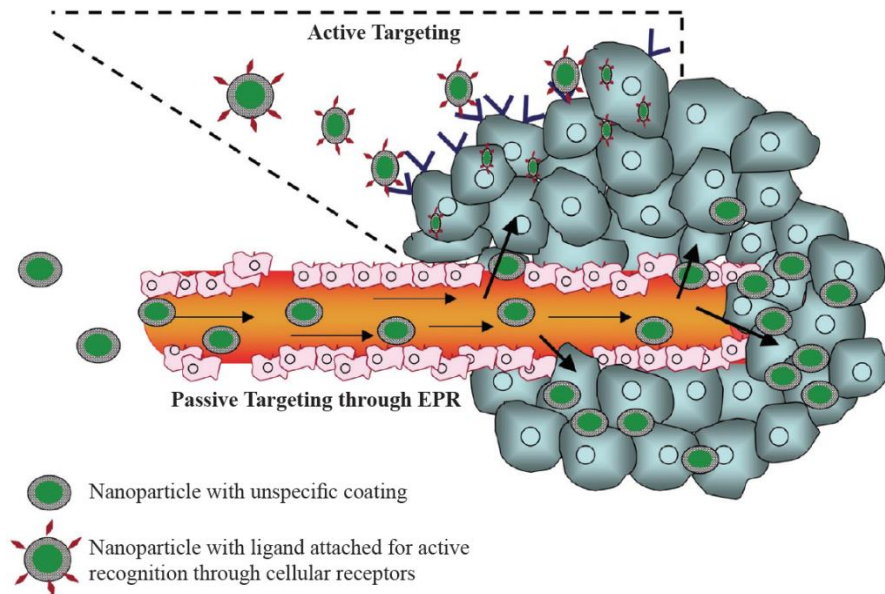


**Figure 1.2** Schematic representation of passive versus active targeting of tumors, as proposed by Latorre *et al.*<sup>43</sup>. Non-targeted nanoparticles accumulate passively via EPR effect, while active targeting is achieved by attaching ligands to the surface of nanoparticles to recognize specific surface receptors in tumor cells.

Receptors for cancer cell active targeting include transferrin, folate receptor, glycoproteins (e.g. lectins) and the epidermal growth factor receptor (EGFR)<sup>37</sup>. Receptors for endothelium include the vascular endothelial growth factors receptors (VEGR), integrins, vascular cell adhesion molecule-1 (VCAM-1) and the matrix metalloproteinases<sup>37</sup>. The tumor vasculature can be stimulated by heat, increasing its permeability thus leading to enhanced transport of macromolecules from endothelium to interstitium. There is evidence that MFH transiently increases perfusion during heating, probably due to perturbations of vascular endothelium thus promoting increased macromolecule and nanoparticle extravasation<sup>44</sup>. This is particularly attractive in order to increase the delivery of chemotherapeutic drugs, using MFH as an adjuvant in cancer therapy.

### 1.2.3 Magnetic Fluid Hyperthermia (MFH)

Based on the properties of magnetic nanoparticles and the tumor microenvironment, nanoparticle accumulation in the tumor is required for the subsequent generation of heat. This is the basic idea behind MFH as a cancer treatment. MFH involves the administration of a colloiddally stable suspension of magnetic nanoparticles, usually via intravenous (IV) but other routes of administration can also be used. Once nanoparticles accumulate in the tumor via EPR effect or via active targeting, exposure to alternating magnetic fields will cause heat dissipation. The released thermal energy from nanoparticles promotes a temperature increase in the tumor, inducing apoptotic cancer cell death<sup>45</sup>. This occurs because of the hypoxic conditions in a tumor which makes cancer cells more susceptible to damage from heat. Nanoparticle concentration and heat generation in the tumor requires being optimal to reach mild hyperthermia (< 43°C) or moderate hyperthermia (43 - 47°C) levels<sup>30</sup>. Figure 1.3 shows a schematic representation of MFH using IV injection. Nanoparticles in MFH treatments require to have appropriate size, usually between 5.5 and 200 nm to avoid renal clearance and recognition by elements of the Mononuclear Phagocytic System (MPS), respectively<sup>43</sup>. Also, adequate surface chemistry is crucial to avoid protein adsorption in the bloodstream, and to resist aggregation in biological fluids, which would lead to decreased circulation times. The goal of MFH is to cause cell damage due to a temperature increase, either by heating a whole tumor or by local heating effects in the vicinity of nanoparticles once they have been internalized by cells<sup>46</sup>. Under this approach, the intracellular environment of cancer cells could be heated without the need for a macroscopic temperature rise of the bulk tumor tissue. Therefore, the term “magnetically mediated energy delivery” (MagMED) would be more applicable to describe local heating effects leading to intracellular hyperthermia<sup>10</sup>. Some effects of MFH at the cellular level include fluidization of cell

membranes, alterations in the cytoskeletal organization, damage of lysosomal membranes, impairment on DNA replication and repair, and elevated expression of heat shock proteins<sup>30</sup>. These effects will eventually lead to cell death, including apoptotic and necrotic programmed cell death which have been widely reported in the literature.

One of the main challenges of MFH is to improve nanoparticle accumulation in tumors for optimal and uniform heat generation. Usually, only a small percentage of the injected dose reaches the tumor when nanoparticles are injected via IV, requiring the injection of large doses of nanoparticles. This increases the accumulation of nanoparticles in body organs such as the liver and the spleen, as the major clearance pathways for nanoparticles in the bloodstream. To circumvent these problems, alternative routes of administration have been proposed, which offer additional advantages to treat specific types of cancers.

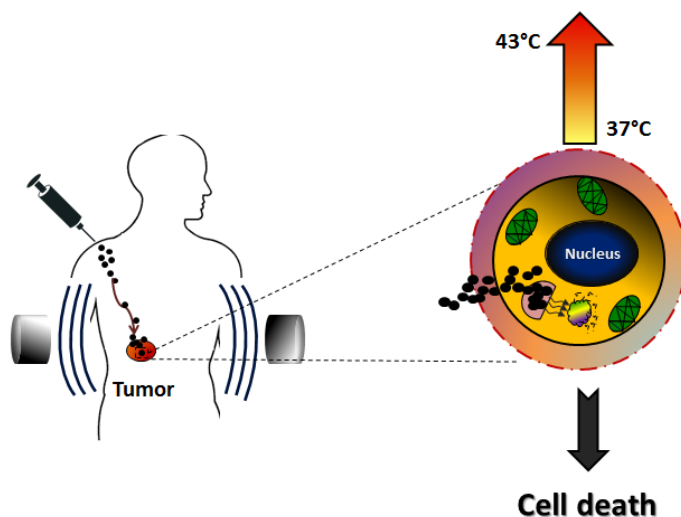


**Figure 1.3** Schematic representation of MFH for cancer treatment, using IV injection, showing subcellular thermal effects.

### 1.2.4 Intraperitoneal administration of nanoparticles and drugs

The intravenous (IV) administration of magnetic nanoparticles for *in vivo* MFH is the most commonly used approach. It has been widely used for the injection of FDA-approved commercial nanoparticle preparations used as Magnetic Resonance Imaging (MRI) contrast agents. The accumulation of nanoparticles in tumors after IV injection occurs via EPR effect but, as it has been stated before, nanoparticle recognition by elements of the MPS usually takes place. Among these alternatives, the intraperitoneal (IP) administration has received special attention, especially for MFH of cancers developing in the peritoneal region. Depending on elimination kinetics, some nanoparticles in the peritoneal cavity will eventually be absorbed to the lymphatic circulation, traveling through the lymph nodes and, depending on the particle size, smaller particles (<50 nm) enter the systemic circulation<sup>67</sup>.

The IP administration of chemotherapeutic drugs has also increased during the last years, with a good number of preclinical and clinical studies in post-operative therapies, especially for ovarian cancer<sup>68</sup>. In fact, it has been reported that cisplatin administered via IP resulted in longer median survival when compared to groups that were treated with cisplatin via IV<sup>69</sup>. Pharmacokinetics of IP administration provide a relatively high concentration of the injected agent, with longer half-life in the peritoneal cavity. Due to their size, nanoparticles have shown increased residence time in the peritoneal cavity when compared to free drug molecules. This is extremely important because the longer the nanoparticles remain in the peritoneal cavity, the easier the recognition by peritoneal macrophages. Some of the challenges of IP chemotherapy include the high interstitial fluid pressure of the peritoneal cavity. This can limit the transport of drugs to tumors, and the possibility of toxicity due to high drug concentrations in the peritoneal cavity. These challenges can be overcome by using nanoparticle-based drug delivery therapies

because of their larger size when compared to free drug molecules. Such size difference promotes the retention of nanoparticles in the peritoneal cavity, with minimal particle clearance if the particle size is adequate. In order to understand the mechanisms associated with IP nanoparticle injection and the characteristics of malignancies to be treated, the anatomy and physiology of abdominal cavity will be reviewed.

### **1.2.5 Peritoneal anatomy and the role of peritoneal macrophages**

The peritoneum is a smooth, serous membrane which lines the abdominal and pelvic cavities, supporting the abdominal organs while interconnecting blood and lymph vessels feeding such organs. This membrane separates two important regions: the peritoneal cavity (PC) which is a free-organ potential space lying between the visceral and parietal layers of the peritoneum, and the sub-peritoneal space (SPS) which comprises the mesenteries, the abdominal/pelvic organs, and their associated vessels and nerves<sup>70</sup>. Learning the differences between these two regions is crucial to understand not only the anatomical features of organs, tissues and cells, but also the pathways for pathological processes. This includes cancer progression and metastases. The peritoneum consists of two continuous layers: the parietal and visceral peritoneum, respectively. The parietal layer lines the internal surface of the abdominal/pelvic wall. The visceral peritoneum invaginates to cover the abdominal visceral organs like stomach, liver, spleen. The visceral peritoneum is a highly folded, complex structure which forms different “reflections” including the mesentery, omentum and peritoneal ligaments<sup>71</sup>. The largest of these folded sheets of visceral peritoneum which extends from the stomach to the duodenum is called omentum, which is divided in greater and lesser omentum. The double-layered greater omentum extends from the greater curvature of the stomach and the proximal part of the duodenum, and it covers the small bowel. The lesser omentum extends from the lesser curvature of the stomach,

connecting it with the duodenum and the liver<sup>72</sup>. Omental tissues are highly vascularized and some functions include lipid storage, regulation of peritoneal fluid flow and reservoir for immune cells<sup>73</sup>. Mesothelial cells in the omentum are composed of adipocytes with specific lymphoid regions rich in immune cells. These regions are known as “milky spots” and they play an important role in the clearance of foreign particles, bacteria and tumor cells from the peritoneal cavity<sup>74</sup>. Among these immune cells, peritoneal macrophages are found in significant amounts in the milky spots, which is a unique feature of this tissue. Macrophages, usually originated from blood monocytes, are a special type of phagocytic cells that migrate and circulate within virtually almost every tissue in the body. Their main function is to identify and engulf foreign particles, pathogens or dead cells. In addition, it has been also demonstrated that milky spots in the greater omentum are major implantation sites for malignant cells and tumor metastases, especially for those of the colon, ovaries and stomach<sup>74,75</sup>. Since milky spots are areas of aggregated inflammatory cells and inflammation has been associated with tumor growth, it is thought that the interaction of immune cells with tumor cells support the formation of solid tumors and their metastases. Omental tissues in humans are very similar to those of mice in terms of anatomical and physiological features. They differ only in the organs adjacent to the omentum, such as the pancreas and the spleen in the case of mice<sup>76</sup>. The localization of omental tissues in the human body is depicted in Figures 1.4 and 1.5, showing the adjacent organs and their anatomical features.

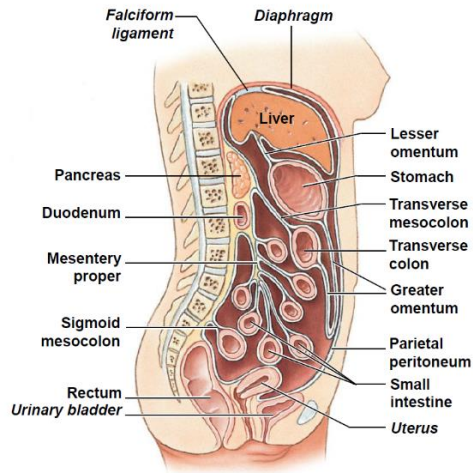


**Figure 1.4** Diagrammatic sagittal view of the human (female) abdominopelvic cavity, showing the localization of the greater and lesser greater omentum. (Reprinted by permission of ©Pearson Education, Inc., New York<sup>77</sup>)

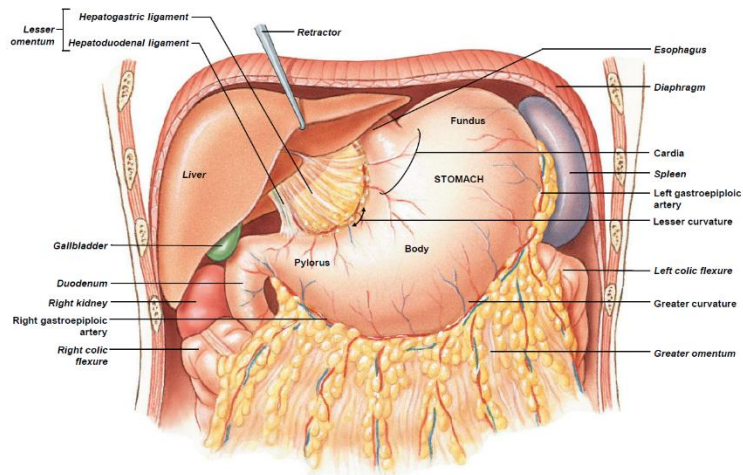


**Figure 1.5** Frontal view of the human abdominopelvic cavity, showing the surface anatomy of the greater and lesser omentum. (Reprinted by permission of ©Pearson Education, Inc., New York<sup>77</sup>)

The fluid present in the peritoneal cavity is quite small, approximately 100 mL, thus it is not visible during imaging<sup>70</sup>. Such fluid is rich in immune cells, including macrophages, B cells, dendritic cells, and others. In mice, two types of peritoneal macrophage populations can be found according to their size: large peritoneal macrophages (LPM) and small peritoneal macrophages (SPM). Both of them play a key role in infection and inflammation processes. It has been reported that LPMs have a self-renewal behavior in the peritoneal cavity whereas small macrophages originate from circulating monocytes. Remarkably, LPMs disappear from the peritoneal cavity and migrate to the omentum under inflammatory conditions<sup>78</sup>. This explains the significant abundance of peritoneal macrophages in the milky spots. The interaction between cancer and immune cells supports the formation of cancer metastases, which can be a limitation when using the omentum as a target tissue for cancer therapies. Interestingly, the migration of peritoneal macrophages to the omentum, as demonstrated in various animal experiments, is particularly important in the design of cancer therapies and new platforms for drug delivery. It has been demonstrated that peritoneal macrophages easily recognize and take up nanoparticles injected via IP, thus peritoneal macrophages can be potentially used as vehicles to transport nanoparticles to the omentum. Several studies using murine cancer models have used this approach employing various nanoparticle platforms. A detailed review and discussion on these studies is presented in Chapter 4. Other phagocytes like blood leukocytes, also recognize and internalize nanoparticles very easily, but they do not accumulate in the milky spots of the omentum as macrophages do. More interestingly, the accumulation of human peripheral blood monocytes with phagocytosed mannose-coated liposomes has been reported in the milky spots of surgically resected human omenta *ex vivo*<sup>79</sup>.

Nanoparticle recognition by peritoneal macrophages can be further increased by targeting nanoparticles to carbohydrate and scavenger receptors, usually overexpressed in macrophages<sup>80</sup>. For this purpose, nanoparticles coated with negatively charged polysaccharide-based polymers (e.g. carboxylic mannan) can be used to target mannose receptors in macrophages, thus increasing the cellular uptake of nanoparticles<sup>81</sup>.

### **1.2.6 Ultrasound and cell sonoporation**

MFH as an adjuvant in chemotherapy-based cancer therapies has been proved to thermally potentiate the mechanism of action of various chemotherapeutic agents, and to promote chemosensitization of various drug-resistant cancer cell lines<sup>2</sup>. An additional challenge that MFH faces is the low nanoparticle and drug uptake by cancer cells. Such low cellular uptake is compensated by the injection of large doses, leading to undesired accumulation and/or damage to healthy tissues. The defective architecture of blood vessels in tumors limits the systemic delivery of both nanoparticles and chemotherapeutic agents, impairing their uptake by tumor cells. One approach that is widely used to improve nanoparticle and drug uptake by cancer cells *in vitro* is the use of active targeting platforms. Molecules such as antibodies, aptamers, peptides or ligands can be covalently attached to nanoparticle-based systems. Such molecules often exhibit high specificity towards receptors overexpressed in cancer cells rather than healthy cells, promoting receptor-mediated endocytosis thus increasing nanoparticle uptake by target cells<sup>82</sup>. Unfortunately, targeted nanoparticles require complex and expensive conjugation techniques, and they are still dependent on the EPR effect to reach the tumor. Furthermore, the internalization of targeted nanoparticles occurs only when they succeed to extravasate from the systemic circulation to tumors. For this reason, nanoparticle biodistribution is not really influenced by targeting molecules and, in fact, targeted nanoparticles have been reported to have

decreased blood circulation times. Immunogenicity has been proposed as a possible reason along with other effects such as impaired tumor penetration and susceptibility to lysosomal digestion<sup>15</sup>. A different approach aiming to improve the systemic extravasation and cellular uptake of nanoparticles and drugs by cancer cells, involves the use of low intensity ultrasound. This approach is attractive because ultrasound is applied in a non-invasive way as an external stimulus. Therapeutic ultrasound has been widely used in the medical field, especially for diagnostic imaging to see internal structures of the body. These structures include organs, muscles, blood vessels and others, using sound waves at different frequencies, produced by a transducer.

Ultrasound has been approved by the FDA for therapeutic applications including tissue healing/stimulation, bone regeneration, circulatory disorders, and others<sup>83</sup>. Depending on the intensity used during ultrasound exposure, different effects can be observed in biological systems including thermal and mechanical effects. The main thermal effect at high acoustic intensities is hyperthermia which can be used for ablation of tumors and other tissues. At lower intensities, mechanical effects can be obtained which are favorable at the cellular level. This dissertation includes experimental work with low-intensity focused ultrasound (LIFU) only, thus any hyperthermia-related effect is due to magnetic hyperthermia. The intensity of ultrasound  $I$ , refers to the amount of energy that a sound wave transfers per cross-sectional area per unit time and it is represented in terms of power per area, usually in  $W/cm^2$ . Ultrasound can be applied either continuously or pulsed “on” and “off” as a train of ultrasound bursts created by modulated, continuous waves. During ultrasound exposure, different parameters can be adjusted such as the intensity ( $I$ ), frequency ( $f$ ), exposure time ( $t_{US}$ ), pulse repetition period ( $PRP$ ) and duty cycle ( $DC$ ). Pulse repetition period is the time between the start of one pulse till the start of the next

pulse, and it is measured in units of time, usually in *ms* or *μs*. The reciprocal of PRP is called pulse repetition frequency (*PRF*) and represents the number of ultrasound pulses occurring in one second. The duty cycle is the ratio between the time that ultrasound is produced (time on) and the total time that ultrasound is exposed (time on + time off), and it is given equation (3):

$$\%DC = \frac{t_{ON}}{t_{ON}+t_{OFF}} * 100 \quad (3)$$

In the biomedical research field, ultrasound has been studied to enhance the uptake of drugs and other molecules with increasing number of studies in drug and gene delivery applications. The rationale behind this ultrasound-improved cellular uptake is the transient cell membrane permeabilization caused by gas microbubbles excited by ultrasound, undergoing mechanical cavitation. This phenomenon is known as sonoporation, and it is capable of modify the structure of cell membranes, inducing the formation of microscopic pores, with no overall damage for cell proliferation. Membrane permeabilization and pore formation due to sonoporation are reversible phenomena with various temporal windows, ranging from minutes to hours depending the cell type and ultrasound parameters<sup>84</sup>. Acoustic cavitation, either stable or inertial, has been identified as the main contributor of sonoporation. The oscillation, expansion, compression, and/or collapse of gas microbubbles disturb the membrane integrity, creating a pore<sup>85</sup>. Once the membrane has been sonoporated, extracellular drugs, nanoparticles and other molecules have facilitated access to the cell's cytoplasm via passive diffusion, thus improving their internalization patterns. The pore size varies depending on parameters such as ultrasound intensity and exposure time, and it is strongly dependent on cell type. Pore diameters in the order of 0.001 – 4.31  $\mu\text{m}$  have been reported, however pore diameters above 400 nm have been associated with notable reductions in cell viability<sup>86,87</sup>. In addition, chemical and shear stresses

may induce the production of reactive oxygen species (ROS), inducing actin rearrangements in the cell membrane. This also contributes to cell membrane permeabilization and pore formation<sup>88</sup>. Other biochemical effects have been observed as a consequence of sonoporation, including activation of apoptosis signaling pathways and activation of G/M cell-cycle arrest<sup>87</sup>. The process of microbubble-mediated cell sonoporation using low-intensity ultrasound to improve the internalization of drugs and nanoparticles is depicted in Figure 1.6.

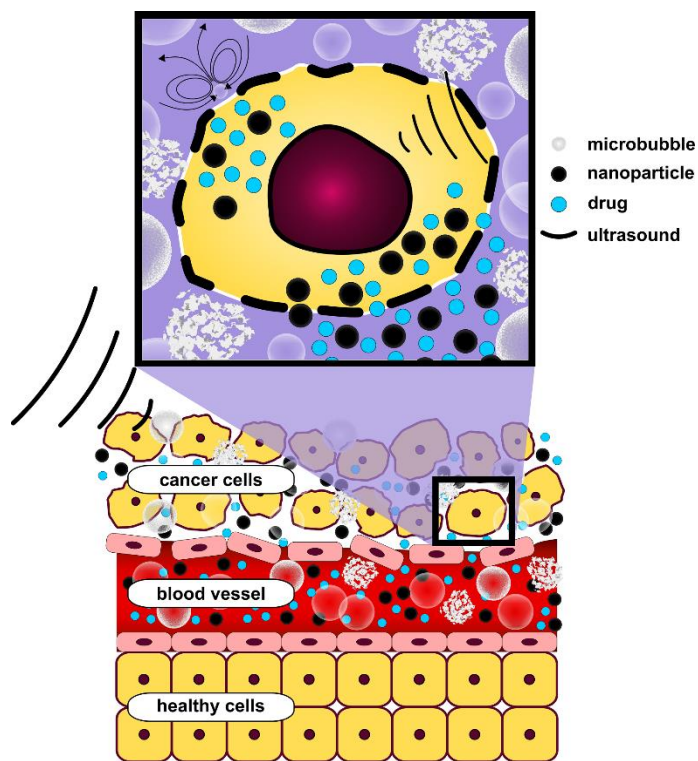


**Figure 1.6** Graphical representation of microbubble-mediated cell sonoporation for the enhanced uptake of magnetic nanoparticles and drug molecules.

In cancer therapy, the insonation of a tumor with low-intensity ultrasound waves has been proposed to improve the uptake of drugs by cancer cells while minimizing toxic effects in the surrounding healthy tissues. Different scenarios have been proposed, including chemotherapy with ultrasound alone, chemotherapy in the presence of microbubbles and ultrasound, chemotherapy-loaded microbubbles and ultrasound. All of these approaches have been suggested either with or without the use of nanoparticles/liposomes<sup>89</sup>. Several studies have been conducted both *in vitro* and *in vivo* with promising results including sono-sensitization of drug-resistant cancer cells, inhibition of tumor growth and increased animal survival times<sup>90,91</sup>. A detailed literature review on the use of low-intensity ultrasound in cancer therapy is presented in Chapter 3 of this dissertation.

Ultrasound contrast agents (UCA) consisting of gas-filled microbubbles in the order of 1 – 10  $\mu\text{m}$ , are used to increase cavitation phenomena due to their large scattering cross-sections<sup>92</sup>. UCA have been traditionally used to improve the visualization of body organs in medical sonography procedures, but their use to enhance cell membrane permeabilization by localized amplification of ultrasound effects during sonoporation continues to increase. UCA are available as commercial preparations, usually coated with lipid-, protein-, or polymer-based shells, enclosing gases like perfluorocarbon, air, or sulphur hexafluoride<sup>90</sup>. Among these preparations, Definity® (Lantheus Medical Imaging) is an FDA-approved microbubble preparation consisting of octafluoropropane-filled bubbles within a phospholipid shell. Definity® has been widely used as UCA in echocardiography<sup>93</sup> and it is the contrast agent used in the experimental work presented this dissertation.

### 1.3 Challenges and perspectives of MFH in cancer treatment

MFH is an advantageous cancer therapy aiming to potentiate the effects of chemotherapeutic drugs while improve specificity and reducing side effects. It can be stated, without doubt that significant progress has been achieved in the field of magnetic nanoparticles and magnetic hyperthermia in cancer treatment. Still, many open questions, poorly understood mechanisms and technical/biological barriers limit the incorporation of MFH in the clinic. Understanding how MFH will succeed as a novel adjuvant in cancer chemotherapy involves multidisciplinary analyses, ranging from material engineering to complex biochemical and physiological concepts. Agreement between chemists, physicists, biologists and engineers, often hard to achieve, plays a key role to face technical limitations associated with magnetic hyperthermia. Importantly, the contribution of these scientific disciplines is of utmost importance when identifying challenges and strategies for the successful translation of MFH to the clinic. Some of these challenges include improving the particle heat dissipation by optimizing the synthesis methods; improving colloidal stability and blood circulation times by selecting appropriate polymer coatings to avoid particle aggregation and/or recognition by the immune system, increasing nanoparticle uptake primarily by cancer cells upon active/passive targeting of nanoparticles to tumors, and increasing particle delivery to tumors by using other routes of administration such as intraperitoneal injection. In addition, other challenges include comparing results between *in vitro* and *in vivo* experiments by using 3D cell cultures, and improving the understanding of cellular mechanisms of chemopotiation and thermochemosensitization. All these challenges and associated opportunities are described in Table 1.1.

**Table 1.1** Challenges of magnetic nanoparticles and magnetic hyperthermia in cancer treatment

Feature	Challenges and opportunities
Heat dissipation rates	<ul style="list-style-type: none"> <li>• Optimize synthesis methods to increase SAR in a reproducible fashion.</li> <li>• Increase SAR without the use of toxic solvents and size fractionation.</li> <li>• High SAR is required to reduce the dose of injected MNPs</li> <li>• High SAR is required for MagMED to be a successful therapy regardless of the tumor size.</li> </ul>
Surface coating and functional molecules	<ul style="list-style-type: none"> <li>• Avoid protein adsorption onto MNPs in blood leading to particle aggregation.</li> <li>• Use of stabilizers to improve colloidal stability thus increasing blood circulation times.</li> <li>• Investigate additional polymer coatings to reduce particle sequestration by phagocytes.</li> <li>• Avoid immunogenicity caused by functional molecules (targeting ligands, fluorophores, drugs, etc.)</li> </ul>
Nanoparticle uptake by cancer cells	<ul style="list-style-type: none"> <li>• Increase nanoparticle internalization into cancer cells rather than healthy cells.</li> <li>• Use of simpler and cost-effective methods to obtain targeted nanoparticles.</li> <li>• Achieve maximal nanoparticle internalization into cancer cells for MagMED: Intracellular heating without the need of a macroscopic temperature rise.</li> <li>• Search for additional methods to passively increase nanoparticle internalization without the use of targeting ligands.</li> </ul>
Routes of administration of MNPs	<ul style="list-style-type: none"> <li>• Reduce nanoparticle accumulation in the liver and spleen when injected via intravenous.</li> <li>• Currently, 0.7% of ID of nanoparticles reaches the tumor with IV injection. There is a need to increase this value.</li> <li>• Improve the inhomogeneity of particle distribution in the tumor when injected via intratumoral.</li> <li>• Increase <i>in vivo</i> experiments using other routes of administration, different to that of intratumoral injection.</li> <li>• Target not only peritoneal macrophages but also tumor-associated macrophages using intraperitoneal injection.</li> </ul>
Combined MFH/chemotherapy	<ul style="list-style-type: none"> <li>• Free drug vs drug-loaded nanoparticle: Design multifunctional nanoparticles for improved, controlled drug release.</li> <li>• Evaluation of enhancement vs synergy: evidence of factual synergy is still required.</li> <li>• MagMED vs MFH: Local heating effects achieved with MagMED are required to enhance thermal potentiation of drugs.</li> <li>• Investigate additional cellular mechanisms by which thermal chemopotential of drugs and thermochemosensitization occur.</li> </ul>
<i>In vitro</i> and <i>in vivo</i> studies, and clinical trials	<ul style="list-style-type: none"> <li>• Perform additional studies with 3D cell cultures given the inconsistent results often observed between <i>in vitro</i> and <i>in vivo</i> studies.</li> <li>• Increase the study of cellular mechanisms by which either MFH or MagMED lead to cancer cell death and other subcellular effects.</li> <li>• Improve the heat distribution in tumors during clinical trials while reducing patient's discomfort at high magnetic field intensities.</li> </ul>

## 1.4 Objectives

### 1.4.1 General objective

The overall objective of this work was the investigation, development and incorporation of optimized methodologies in the field of MFH, covering the areas of material engineering, cellular response, and performance in animal models.

### 1.4.2 Specific objectives

*Optimize the co-precipitation synthesis of magnetic nanoparticles to increase the heat dissipation rates.*

- Obtain SAR values above 500 W/g<sub>Fe</sub> for nanoparticles synthesized by co-precipitation.
- Use a simple, cost-effective and scalable method with improved reproducibility between different nanoparticle synthesis batches.
- Increase SAR values for nanoparticle preparations with restriction of physical rotation.
- Coat the surface of bare iron oxide magnetic nanoparticles with PEG-Silane.

*Improve the efficacy of in vitro MFH/drug in ovarian cancer treatment using low-intensity ultrasound.*

- Determine the cytocompatibility of PEG-coated nanoparticles in ovarian cancer cell lines (A2780, HeyA8, SKOV3) and colloidal stability in biological media.

- Optimize the experimental conditions for ultrasound exposure leading to cell sonoporation with minimal effects for cell viability.
- Investigate the effects of low-intensity ultrasound on the cellular uptake of magnetic nanoparticles and the drug Pifithrin- $\mu$ .
- Improve the effects of MFH and MFH/drug combined treatments using low-intensity ultrasound to establish the triple treatment Ultrasound/MFH/drug.

***Investigate the potential of intraperitoneal administration of MNPs and their uptake by mouse peritoneal macrophages to optimize particle accumulation in tumors.***

- Study and compare pharmacokinetics and biodistribution of PEG-coated nanoparticles injected via IP and IV in athymic nude mice.
- Determine the accumulation of PEG-coated nanoparticles in breast cancer subcutaneous tumors using IP and IV injections.
- Determine, qualitative and quantitatively, the uptake of PEG-coated nanoparticles by mouse peritoneal macrophages *ex vivo*.

## **1.5 Overview of the Dissertation**

This dissertation contains results of experimental work with potential improvement opportunities, in efforts to overcome three specific challenges that MFH currently faces as an adjuvant cancer therapy. Through this chapter, the rationale and the theoretical background have been introduced, the objectives have delimited, and the expected contribution of this work in the field of magnetic hyperthermia for cancer therapy has been highlighted.

Chapter 2 presents the optimization of co-precipitation synthesis and peptization of iron oxide magnetic nanoparticle, studying the influence of temperature, total iron concentration and sonication. The physical, chemical and magnetic properties of nanoparticles were studied using various characterization techniques. SAR values of both liquid and solid nanoparticle preparations were determined by induction calorimetry and normalized by the iron concentration determined by UV/Vis spectroscopy. Reproducibility was evaluated, and predictive models were proposed using statistical linear models. Finally, iron oxide nanoparticles were coated with PEG-Silane and characterized to evaluate the presence of the polymer using thermogravimetric analysis (TGA), Fourier-transform infrared (FTIR) spectroscopy and zeta potential.

Chapter 3 presents a potential sono/thermo/chemotherapy for the treatment of ovarian cancer using the cell line Hey A8. The use of low-intensity ultrasound to induce cell sonoporation is proposed to improve the internalization of magnetic nanoparticles and the anti-cancer drug pifithrin- $\mu$  into ovarian cancer cells. Cell response to ultrasound was evaluated using cell viability ratios, and fluorescence microscopy to visualize the effects of cell membrane permeabilization. Nanoparticle internalization uptake by ovarian cancer cells was quantified using UV/Vis spectroscopy. The potentiation of pifithrin- $\mu$  and MFH as cancer therapies, either individually or combined, were studied with the incorporation low-intensity ultrasound.

Chapter 4 presents preliminary *in vivo* studies, introducing the potential of intraperitoneal administration of magnetic nanoparticles, cellular uptake by peritoneal macrophages and accumulation in subcutaneous breast tumors. A comparison of pharmacokinetics and biodistribution of nanoparticles injected via IP and IV is presented. Iron oxide concentrations in blood, body organs and tumors were quantified using electron paramagnetic resonance spectroscopy (EPRs). Mouse peritoneal macrophages were obtained using non-elicited isolation

techniques and the nanoparticle uptake by macrophages was determined qualitatively using Prussian Blue staining, and quantitatively via EPRs.

Finally, chapter 5 presents the final remarks, conclusions and contributions of this dissertation, along with recommendations for future works.

## 1.6 References

1. van der Zee, J. Heating the patient: a promising approach? *Ann. Oncol.* **13**, 1173–1184 (2002).
2. Torres-Lugo, M. & Rinaldi, C. Thermal potentiation of chemotherapy by magnetic nanoparticles. *Nanomedicine (Lond)*. **8**, 1689–707 (2013).
3. Chatterjee, D. K., Diagaradjane, P. & Krishnan, S. Nanoparticle-mediated hyperthermia in cancer therapy. *Ther. Deliv.* **2**, 1001–1014 (2011).
4. Miaskowski, A. & Krawczyk, A. Magnetic Fluid Hyperthermia for Cancer Therapy. *Electr. Rev.* 125–127 (2011).
5. Chen, B., Yanyan Ren & Chen, B. Multifunctional magnetic Fe<sub>3</sub>O<sub>4</sub> nanoparticles combined with chemotherapy and hyperthermia to overcome multidrug resistance. *Int. J. Nanomedicine* **7**, 2261 (2012).
6. Alvarez-Berríos, M. P. *et al.* Hyperthermic potentiation of cisplatin by magnetic nanoparticle heaters is correlated with an increase in cell membrane fluidity. *Int. J. Nanomedicine* **8**, 1003–1013 (2013).
7. Li, L. *et al.* Comparative *in Vitro* Cytotoxicity Study on Uncoated Magnetic

- Nanoparticles: Effects on Cell Viability, Cell Morphology, and Cellular Uptake. *J. Nanosci. Nanotechnol.* **12**, 9010–9017 (2012).
8. Salmaso, S. & Caliceti, P. Stealth Properties to Improve Therapeutic Efficacy of Drug Nanocarriers. *J. Drug Deliv.* **2013**, 1–19 (2013).
  9. Lewinski, N., Colvin, V. & Drezek, R. Cytotoxicity of Nanoparticles. *Small* **4**, 26–49 (2008).
  10. Kozissnik, B., Bohorquez, A. C., Dobson, J. & Rinaldi, C. Magnetic fluid hyperthermia: advances, challenges, and opportunity. *Int. J. Hyperthermia* **29**, 706–14 (2013).
  11. Fortin, J.-P. *et al.* Size-sorted anionic iron oxide nanomagnets as colloidal mediators for magnetic hyperthermia. *J. Am. Chem. Soc.* **129**, 2628–35 (2007).
  12. Bae, K. H. *et al.* Chitosan oligosaccharide-stabilized ferrimagnetic iron oxide nanocubes for magnetically modulated cancer hyperthermia. *ACS Nano* **6**, 5266–73 (2012).
  13. Hugounenq, P. *et al.* Iron Oxide Monocrystalline Nanoflowers for Highly Efficient Magnetic Hyperthermia. *J. Phys. Chem. C* **116**, 15702–15712 (2012).
  14. Gobbo, O. L., Sjaastad, K., Radomski, M. W., Volkov, Y. & Prina-Mello, A. Magnetic Nanoparticles in Cancer Theranostics. *Theranostics* **5**, 1249–1263 (2015).
  15. Chen, W. C., Zhang, A. X. & Li, S.-D. Limitations and niches of the active targeting approach for nanoparticle drug delivery. *Eur. J. Nanomedicine* **4**, 89–93 (2012).
  16. Wood, A. K. W. & Sehgal, C. M. A Review of Low-Intensity Ultrasound for Cancer Therapy. *Ultrasound Med. Biol.* **41**, 905–928 (2015).

17. Watson, K. D. *et al.* Ultrasound Increases Nanoparticle Delivery by Reducing Intratumoral Pressure and Increasing Transport in Epithelial and Epithelial-Mesenchymal Transition Tumors. *Cancer Res.* **72**, 1485–1493 (2012).
18. Wang, Y.-X. J. *et al.* Low-intensity pulsed ultrasound increases cellular uptake of superparamagnetic iron oxide nanomaterial: results from human osteosarcoma cell line U2OS. *J. Magn. Reson. Imaging* **31**, 1508–13 (2010).
19. Wilhelm, S. *et al.* Analysis of nanoparticle delivery to tumours. *Nat. Rev. Mater.* **1**, 16014 (2016).
20. Ikehara, Y. *et al.* A carbohydrate recognition-based drug delivery and controlled release system using intraperitoneal macrophages as a cellular vehicle. *Cancer Res.* **66**, 8740–8748 (2006).
21. Ferlay, J. *et al.* Cancer incidence and mortality worldwide: Sources, methods and major patterns in GLOBOCAN 2012. *Int. J. Cancer* **136**, E359–E386 (2015).
22. Siegel, R. L., Miller, K. D. & Jemal, A. Cancer statistics, 2017. *CA. Cancer J. Clin.* **67**, 7–30 (2017).
23. Lorusso, D. *et al.* Review role of topotecan in gynaecological cancers: current indications and perspectives. *Crit. Rev. Oncol. Hematol.* **74**, 163–74 (2010).
24. Hudis, C. A. & Gianni, L. Triple-Negative Breast Cancer: An Unmet Medical Need. *Oncologist* **16**, 1–11 (2011).
25. Bauer, K. R., Brown, M., Cress, R. D., Parise, C. A. & Caggiano, V. Descriptive analysis

- of estrogen receptor (ER)-negative, progesterone receptor (PR)-negative, and HER2-negative invasive breast cancer, the so-called triple-negative phenotype: A population-based study from the California Cancer Registry. *Cancer* **109**, 1721–1728 (2007).
26. Pepa, C. Della *et al.* Ovarian cancer standard of care: are there real alternatives? *Chin. J. Cancer* **34**, 17–27 (2015).
  27. Wahba, H. A. & El-Hadaad, H. A. Current approaches in treatment of triple-negative breast cancer. *Cancer Biol. Med.* **12**, 106–16 (2015).
  28. Goff, B. A. Advanced ovarian cancer: what should be the standard of care? *J. Gynecol. Oncol.* **24**, 83 (2013).
  29. Kigawa, J. New strategy for overcoming resistance to chemotherapy of ovarian cancer. *Yonago Acta Med.* **56**, 43–50 (2013).
  30. Hildebrandt, B., Wust, P. & Ahlers, O. The cellular and molecular basis of hyperthermia. *Crit. Rev. ...* **43**, 33–56 (2002).
  31. Chicheł, A., Skowronek, J., Kubaszewska, M. & Kanikowski, M. Hyperthermia – description of a method and a review of clinical applications. *Reports Pract. Oncol. Radiother.* **12**, 267–275 (2007).
  32. Kumar, C. S. S. R. & Mohammad, F. Magnetic nanomaterials for hyperthermia-based therapy and controlled drug delivery. *Adv. Drug Deliv. Rev.* **63**, 789–808 (2011).
  33. Albini, A. & Sporn, M. B. The tumour microenvironment as a target for chemoprevention. *Nat. Rev. Cancer* **7**, 139–1447 (2007).

34. Koontongkaew, S. The Tumor Microenvironment Contribution to Development, Growth, Invasion and Metastasis of Head and Neck Squamous Cell Carcinomas. *J. Cancer* **4**, 66–83 (2013).
35. Wong, A. D., Ye, M., Ulmschneider, M. B. & Searson, P. C. Quantitative analysis of the Enhanced Permeation and Retention (EPR) effect. *PLoS One* **10**, 1–13 (2015).
36. Moorthi, C., Manavalan, R. & Kathiresan, K. Nanotherapeutics to Overcome Conventional Cancer Chemotherapy Limitations. **14**, 67–77 (2011).
37. Danhier, F., Feron, O. & Pr at, V. To exploit the tumor microenvironment: Passive and active tumor targeting of nanocarriers for anti-cancer drug delivery. *J. Control. Release* **148**, 135–146 (2010).
38. Kobayashi, H., Watanabe, R. & Choyke, P. L. Improving Conventional Enhanced Permeability and Retention (EPR) Effects; What Is the Appropriate Target? *Theranostics* **4**, 81–89 (2014).
39. Bazak, R., Houri, M., El Achy, S., Hussein, W. & Refaat, T. Passive targeting of nanoparticles to cancer: A comprehensive review of the literature. *Mol. Clin. Oncol.* 904–908 (2014). doi:10.3892/mco.2014.356
40. Maeda, H. Macromolecular therapeutics in cancer treatment: the EPR effect and beyond. *J. Control. Release* **164**, 138–44 (2012).
41. Kim, D. K., Maria Mikhaylova, Yu Zhang & Mamoun Muhammed. Protective Coating of Superparamagnetic Iron Oxide Nanoparticles. *Chem. Mater.* **15**, 1617–1627

- (2003).
42. Chen, W. C., Zhang, A. X. & Li, S. D. Limitations and niches of the active targeting approach for nanoparticle drug delivery. *Eur. J. Nanomedicine* **4**, 89–93 (2012).
  43. Latorre, M. & Rinaldi, C. Applications of magnetic nanoparticles in medicine: magnetic fluid hyperthermia. *P. R. Health Sci. J.* **28**, 227–38 (2009).
  44. Kirui, D. K. *et al.* Tumor vascular permeabilization using localized mild hyperthermia to improve macromolecule transport. *Nanomedicine Nanotechnology, Biol. Med.* **10**, 1487–1496 (2014).
  45. Laurent, S., Dutz, S., Häfeli, U. O. & Mahmoudi, M. Magnetic fluid hyperthermia: focus on superparamagnetic iron oxide nanoparticles. *Adv. Colloid Interface Sci.* **166**, 8–23 (2011).
  46. Chiu-Lam, A. & Rinaldi, C. Nanoscale Thermal Phenomena in the Vicinity of Magnetic Nanoparticles in Alternating Magnetic Fields. *Adv. Funct. Mater.* n/a-n/a (2016). doi:10.1002/adfm.201505256
  47. Benz, M. *Superparamagnetism : Theory and Applications. Superparamagnetism : Theory and Applications* (2012).
  48. Hofmann-Antenbrink, M., von Rechenberg, B. & Hofmann, H. *Superparamagnetic nanoparticles for biomedical applications. Advanced drug delivery reviews* **65**, (2009).
  49. Bucak, S., Sezer, A. & Yavuztürk, B. *Recent Advances in Novel Drug Carrier Systems.* (InTech, 2012). doi:10.5772/2889

50. Jolivet, J.-P., Chanéac, C. & Tronc, E. Iron oxide chemistry. From molecular clusters to extended solid networks. *Chem. Commun.* 477–483 (2004). doi:10.1039/B304532N
51. Laurent, S. *et al.* Magnetic iron oxide nanoparticles: synthesis, stabilization, vectorization, physicochemical characterizations, and biological applications. *Chem. Rev.* **108**, 2064–110 (2008).
52. Massart, R. Preparation of Aqueous Magnetic Liquids in Alkaline and Acidic Media. *IEEE Trans. Magn.* **17**, 1247–1248 (1981).
53. Babes, L., Denizot, B., Tanguy, G., Le Jeune, J. J. & Jallet, P. Synthesis of Iron Oxide Nanoparticles Used as MRI Contrast Agents: A Parametric Study. *J. Colloid Interface Sci.* **212**, 474–482 (1999).
54. Vayssières, L., Chanéac, C., Tronc, E. & Jolivet, J. P. Size Tailoring of Magnetite Particles Formed by Aqueous Precipitation: An Example of Thermodynamic Stability of Nanometric Oxide Particles. *J. Colloid Interface Sci.* **205**, 205–212 (1998).
55. Andrade, Â. L., Fabris, J. D., Ardisson, J. D., Valente, M. a. & Ferreira, J. M. F. Effect of Tetramethylammonium Hydroxide on Nucleation, Surface Modification and Growth of Magnetic Nanoparticles. *J. Nanomater.* **2012**, 1–10 (2012).
56. Rosensweig, R. E. Heating magnetic fluid with alternating magnetic field. *J. Magn. Magn. Mater.* **252**, 370–374 (2002).
57. Fannin, P. C. & Charles, S. W. The study of a ferrofluid exhibiting both Brownian and Neel relaxation. *J. Phys. D. Appl. Phys.* **22**, 187–191 (1989).

58. Kötitz, R., Weitschies, W., Trahms, L. & Semmler, W. Investigation of Brownian and Néel relaxation in magnetic fluids. *J. Magn. Magn. Mater.* **201**, 102–104 (1999).
59. Erné, B. H., Butter, K., Kuipers, B. W. M. & Vroege, G. J. Rotational Diffusion in Iron Ferrofluids. *Langmuir* **19**, 8218–8225 (2003).
60. Shah, R. R., Davis, T. P., Glover, A. L., Nikles, D. E. & Brazel, C. S. Impact of magnetic field parameters and iron oxide nanoparticle properties on heat generation for use in magnetic hyperthermia Rhythm. *J. Magn. Magn. Mater.* **387**, 96–106 (2015).
61. Suto, M. *et al.* Heat dissipation mechanism of magnetite nanoparticles in magnetic fluid hyperthermia. *J. Magn. Magn. Mater.* **321**, 1493–1496 (2009).
62. Kallumadil, M. *et al.* Suitability of commercial colloids for magnetic hyperthermia. *J. Magn. Magn. Mater.* **321**, 1509–1513 (2009).
63. Lee, J.-H. *et al.* Exchange-coupled magnetic nanoparticles for efficient heat induction. *Nat. Nanotechnol.* **6**, 418–22 (2011).
64. Guardia, P. *et al.* Water-soluble iron oxide nanocubes with high values of specific absorption rate for cancer cell hyperthermia treatment. *ACS Nano* **6**, 3080–91 (2012).
65. Lartigue, L. *et al.* Cooperative organization in iron oxide multi-core nanoparticles potentiates their efficiency as heating mediators and MRI contrast agents. *ACS Nano* **6**, 10935–49 (2012).
66. Martinez-Boubeta, C. *et al.* Learning from Nature to Improve the Heat Generation of Iron-Oxide Nanoparticles for Magnetic Hyperthermia Applications. *Sci. Rep.* **3**, 1652 (2013).

67. Bajaj, G. & Yeo, Y. Drug Delivery Systems for Intraperitoneal Therapy. *Pharm. Res.* **27**, 735–738 (2010).
68. Yen, M. S. *et al.* Intraperitoneal cisplatin-based chemotherapy vs. Intravenous cisplatin-based chemotherapy for stage III optimally cytoreduced epithelial ovarian cancer. *Int. J. Gynecol. Obstet.* **72**, 55–60 (2001).
69. Alberts, D. S. *et al.* Intraperitoneal Cisplatin plus Intravenous Cyclophosphamide versus Intravenous Cisplatin plus Intravenous Cyclophosphamide for Stage III Ovarian Cancer. *N. Engl. J. Med.* **335**, 1950–1955 (1996).
70. Pannu, H. K. & Oliphant, M. The subperitoneal space and peritoneal cavity: basic concepts. *Abdom. Imaging* **40**, 2710–2722 (2015).
71. Healy, J. C. & Reznick, R. H. The peritoneum, mesenteries and omenta: normal anatomy and pathological processes. *Eur. Radiol.* **8**, 886–900 (1998).
72. Yoo, E. *et al.* Greater and Lesser Omenta: Normal Anatomy and Pathologic Processes. *RadioGraphics* **27**, 707–720 (2007).
73. Pond, C. M. Adipose tissue and the immune system. *Prostaglandins Leukot. Essent. Fat. Acids* **73**, 17–30 (2005).
74. Krist, L. F. G. *et al.* Milky spots in the greater omentum are predominant sites of local tumour cell proliferation and accumulation in the peritoneal cavity. *Cancer Immunol. Immunother.* **47**, 205–212 (1998).
75. Liu, J., Geng, X. & Li, Y. Milky spots: omental functional units and hotbeds for peritoneal

- cancer metastasis. *Tumor Biol.* **37**, 5715–5726 (2016).
76. Greten, F. R. *et al.* IKK $\beta$  links inflammation and tumorigenesis in a mouse model of colitis-associated cancer. *Cell* **118**, 285–296 (2004).
  77. Martini, F. H., Timmons, M. J. & Robert B. Tallitsch. *Human Anatomy*. (Pearson Education, Inc., 2013).
  78. Cassado, A. A., D’Império Lima, M. R. & Bortoluci, K. R. Revisiting mouse peritoneal macrophages: Heterogeneity, development, and function. *Front. Immunol.* **6**, 1–9 (2015).
  79. Matsui, M. *et al.* Targeted delivery of oligomannose-coated liposome to the omental micrometastasis by peritoneal macrophages from patients with gastric cancer. *Cancer Sci.* **101**, 1670–1677 (2010).
  80. Vu-Quang, H. *et al.* Targeted delivery of mannan-coated superparamagnetic iron oxide nanoparticles to antigen-presenting cells for magnetic resonance-based diagnosis of metastatic lymph nodes in vivo. *Acta Biomater.* **7**, 3935–3945 (2011).
  81. Vu-Quang, H. *et al.* Carboxylic mannan-coated iron oxide nanoparticles targeted to immune cells for lymph node-specific MRI in vivo. *Carbohydr. Polym.* **88**, 780–788 (2012).
  82. Bahrami, B. *et al.* Nanoparticles and targeted drug delivery in cancer therapy. *Immunol. Lett.* **190**, 64–83 (2017).
  83. ter Haar, G. Therapeutic applications of ultrasound. *Prog. Biophys. Mol. Biol.* **93**, 111–29 (2007).

84. Yudina, A., Lepetit-Coiffé, M. & Moonen, C. T. W. Evaluation of the temporal window for drug delivery following ultrasound-mediated membrane permeability enhancement. *Mol. Imaging Biol.* **13**, 239–49 (2011).
85. Lentacker, I., De Cock, I., Deckers, R., De Smedt, S. C. & Moonen, C. T. W. Understanding ultrasound induced sonoporation: Definitions and underlying mechanisms. *Adv. Drug Deliv. Rev.* **72**, 49–64 (2014).
86. Yang, F. *et al.* Experimental study on cell self-sealing during sonoporation. *J. Control. Release* **131**, 205–210 (2008).
87. Zhong, W., Sit, W. H., Wan, J. M. F. & Yu, A. C. H. Sonoporation Induces Apoptosis and Cell Cycle Arrest in Human Promyelocytic Leukemia Cells. *Ultrasound Med. Biol.* **37**, 2149–2159 (2011).
88. Juffermans, L. J. M., Kamp, O., Dijkmans, P. A., Visser, C. A. & Musters, R. J. P. Low-Intensity Ultrasound-Exposed Microbubbles Provoke Local Hyperpolarization of the Cell Membrane Via Activation of BKCa Channels. *Ultrasound Med. Biol.* **34**, 502–508 (2008).
89. Wood, A. K. W. & Sehgal, C. M. A review of low-intensity ultrasound for cancer therapy. *Ultrasound Med. Biol.* **41**, 905–928 (2015).
90. Nomikou, N. & McHale, A. P. Exploiting ultrasound-mediated effects in delivering targeted, site-specific cancer therapy. *Cancer Lett.* **296**, 133–143 (2010).
91. Yu, T., Huang, X., Hu, K., Bai, J. & Wang, Z. Treatment of transplanted adriamycin-resistant ovarian cancers in mice by combination of adriamycin and ultrasound exposure.

*Ultrason. Sonochem.* **11**, 287–291 (2004).

92. Dalecki, D. Mechanical bioeffects of ultrasound. *Annu. Rev. Biomed. Eng.* **6**, 229–48 (2004).
93. Lantheus Medical Imaging. Definity (octafluoropropane, phospholipid microspheres for injectable suspension. Full Prescribing Information. 1–18 (2011).

# Chapter 2

## ***Optimization of synthesis and peptization of magnetic nanoparticles to increase heat dissipation rates***

---

*Essential topics of this chapter were included in the study published in the Journal of Magnetism and Magnetic Materials. (Mérida et al., 2015)<sup>1</sup>*

### **2.1 Summary**

The ability of MNPs to produce heat when exposed to an external, alternating magnetic field, is a well-known phenomenon, but it has not been fully optimized<sup>2</sup>. Significant efforts have been made to increase the heat dissipation rates of these materials as a strategy to reduce the dose of particles needed to achieve a desired temperature rise in tumors *in vivo*, and to avoid excessive nanoparticle accumulation in body organs<sup>3</sup>. Even when several studies have been published attempting to optimize the synthesis of MNPs, most of them deal with the optimization of particle size<sup>4-7</sup>. Among the parameters that have been considered for these studies include media composition, injection fluxes, temperature, stirring rates, pH, molar ratios among others<sup>7-9</sup>. The increased interest to maximize the Specific Absorption Rate (SAR) and inherently, the Intrinsic Loss Power (ILP), have pushed optimization studies in that direction. It is important to note that ILP is very useful because, as explained in Chapter 1, it facilitates comparisons of measurements carried out under different field conditions. To this date, commercial nanoparticle preparations used as candidates for Magnetic Fluid Hyperthermia (MFH), have reported ILP values up to 3 nH m<sup>2</sup> kg<sup>-10</sup>. In addition, synthetic and naturally occurring iron oxide nanoparticles for potential use in the biomedical applications have typical ILP values between 3.8 and 12 nH m<sup>2</sup> kg<sup>-1</sup>, respectively<sup>11,12</sup>. This chapter features the work carried out to optimize the co-precipitation

synthesis along with the peptization step, to increase the rates of energy dissipation of iron oxide magnetic nanoparticles. It was hypothesized that by studying physicochemical parameters of synthesis and the incorporation of robust sonication conditions during the peptization step, the SAR values of nanoparticles would increase. Results revealed a set of optimal conditions to obtain magnetic nanoparticles with high SAR values in both liquid and solid matrices.

## 2.2 Introduction and literature review

There have been many recent excellent studies aiming to obtain magnetic nanoparticles with high SAR and ILP values, through the control of particle clustering, shape, and/or internal exchange interactions. These studies are summarized in Table 2.1 and discussed in detail along this section.

**Table 2.1** Summary of studies on SAR maximization

Author	Nanoparticle shape/ structure	Core material / magnetic behavior	SAR (W/g <sub>Fe</sub> )	ILP (nH m <sup>2</sup> kg <sup>-1</sup> )
Bae <i>et al.</i> <sup>13</sup>	Nanocubes	Magnetite / ferromagnetic	2,614	N/A
Guardia <i>et al.</i> <sup>14</sup>	Nanocubes	Magnetite / superparamagnetic	2,277	5.65
Alphandéry <i>et al.</i> <sup>15</sup>	Chain-shape Roughly spherical	Magnetosomes from bacteria	875	4.67
Lee <i>et al.</i>	Metallic core-shell	Maghemite; Cobalt and manganese	1,120	1.61
Hugounenq <i>et al.</i> <sup>16</sup>	Nanoflowers	Maghemite/ superparamagnetic	1,900	5.87
Lartigue <i>et al.</i> <sup>17</sup>	Cooperative multi- core	Maghemite/ superparamagnetic	1,500	3.43
Fortin <i>et al.</i> <sup>11</sup>	Roughly spherical, size sorted	Maghemite /superparamagnetic	1,650	3.80

Ferromagnetic nanocube aggregates encapsulated in biocompatible polymers have been reported with SAR values up to 2,614 W/g<sub>Fe</sub> but aggregation is a major obstacle to their use *in vivo*<sup>13,18</sup>. However, according to the authors, this exceptionally high SAR was achieved using an alternating magnetic field with frequency of 1,000 kHz and amplitude of 0.66 kA/m, which yields a highly unlikely ILP of 6,000. In another study, superparamagnetic iron oxide nanocubes with SAR values above 2,277 W/g<sub>Fe</sub> (700 kHz, 24 kA/m, ILP = 5.65) were reported, but despite their high SAR and more reliable ILP value, the authors stated that the synthesis of nanocubes in a wide size range is not straightforward<sup>14</sup>, which could limit their biomedical potential.

Other efforts aiming to achieve high heat dissipation rates have led to extract magnetic materials from living organisms. This is the case of magnetosomes isolated from AMB-1 magnetotactic bacteria as an alternative to the preparation of magnetic materials using chemical methods. The obtained chain-shaped magnetosomes have been reported to have SAR values up to 875 W/g<sub>Fe</sub> (183 kHz, 32 kA/m, ILP = 4.67). However, the isolation of individual magnetosomes from the main chain remains a challenge to their clinical applications<sup>15</sup>. An alternative approach is to tune heat dissipation rate by introducing exchange-coupling in nanoparticles with core-shell structure. For this purpose, different nanoparticle platforms such as CoFe<sub>2</sub>O<sub>4</sub>, MnFe<sub>2</sub>O<sub>4</sub>, Fe<sub>3</sub>O<sub>4</sub> and others, have been synthesized yielding SAR values up to 1,120 W/g<sub>Fe</sub> (ILP = 1.61) at 500 kHz and 37.3 kA/m for CoFe<sub>2</sub>O<sub>4</sub> (core) Fe<sub>3</sub>O<sub>4</sub> (shell) configuration<sup>19</sup>. However, to achieve this effect the biocompatibility of nanoparticles is compromised by the introduction of cobalt into their structure.

Other nanoparticle shapes have been reported to yield high energy dissipation rates. Maghemite nanoflowers obtained under high-temperature and prolonged time synthesis methods have reported SAR values of ~ 1,900 W/g<sub>Fe</sub> (700 kHz, 21.5 kA/m, ILP = 5.87) using a special

thermal decomposition procedure<sup>16</sup>. Similarly, to nanoflowers, maghemite assemblies with superparamagnetic behavior, identified as “cooperative organized multi-core nanoparticles” have reported SAR values  $\sim 1,500$  W/g<sub>Fe</sub> (520 kHz, 29 kA/m, ILP = 3.43). The reduced magnetocrystalline anisotropy and enhanced magnetic moment of these multi-core interactions helps to preserve the superparamagnetic behavior, which leads to the potentiation of thermal losses<sup>17</sup>.

Finally, and perhaps of greatest relevance to the work we have conducted, a post synthesis size-sorting method using maghemite nanoparticles was reported with SAR values of up to 1,650 W/g<sub>Fe</sub> (700 kHz, 24.8 kA/m, ILP = 3.8)<sup>11</sup>. Interestingly, without the post-synthesis treatment the heat dissipation rate of the particles dropped to 135 W/g<sub>Fe</sub> and the polydispersion index of the particles increased. Even with the good performance of maghemite, either as a clusters or after size-sorting fractionation, this iron oxide phase tends to lose its susceptibility with time<sup>20</sup>, thus nanoparticles composed by magnetite as the predominant iron oxide phase are preferred.

Despite the overall high heating efficiency provided by exchange-coupled, size-sorted and clusters of nanoparticles with different morphologies, the experimental protocols used to obtain these particles are often complex, time consuming, and can face challenges in scalability. In contrast, it is widely known that a simple, inexpensive, and efficient method for the synthesis of magnetic nanoparticles is the co-precipitation of iron salts in alkaline media under an inert atmosphere, attributed to Massart<sup>21</sup>. In addition to its simplicity, the main advantage of the co-precipitation method is the ease of scale up and very high yields. However, a major drawback in this synthesis method has been the low and non-uniform SAR values, typically ranging in 40 – 300 W/g<sub>Fe</sub><sup>22–24</sup> without post synthesis size-selective treatments, and about 10 – 100 W/g<sub>Fe</sub> for commercial nanoparticle preparations<sup>10,25</sup>. It is evident that the wide range and variability of

SAR in the co-precipitation method represent major limitations to eventual clinical translation, where consistent high-energy dissipation rates are required. As mentioned before, there are numerous studies aiming to control the physical size of nanoparticles, and even when energy dissipation is expected to be a function of physical size and magnetic properties, systematic optimization studies of the co-precipitation synthesis are required. For example, Kossatz *et al*<sup>26</sup> recently developed a post synthesis stabilization approach for nanoparticles obtained through co-precipitation with SAR values of 900 W/g<sub>Fe</sub> (435 kHz, 15.4 kA/m, ILP = 6.3) which is one of the highest values obtained without size-fractionation. Such particle stabilization approach (namely, peptization) involves the use of kerosene at high temperature which represent a safety issue during experimentation. Unfortunately, the authors did not suggest any explanation behind their improved energy dissipation rates or what they did different from previous studies in terms of experimental protocols during co-precipitation reaction. In addition, it was impossible to compare the magnetic behavior of their particles to those of others to evaluate its impact on SAR due to the lack of magnetic characterizations.

Motivated by the need to improve SAR values and the advantages of the co-precipitation synthesis, the present work aimed to demonstrate that high energy dissipating nanoparticles can be reproducibly obtained by optimizing the co-precipitation synthesis conditions and the subsequent peptization step. Three parameters were systematically studied and varied for optimization purposes: temperature, iron ion precursor concentration, and sonication conditions during peptization. These parameters were chosen based on results from our own preliminary experiments and the work of others<sup>27,28</sup>. Preliminary work revealed that improvements on SAR values took place when the synthesis was carried out at higher temperatures and a high-energy ultrasound probe was used during the peptization step while keeping a fixed iron concentration.

As a result, it was hypothesized that the combination of these parameters at different levels could lead to improvements on the heat dissipation rates and improvements in reproducibility of experiments. To test our hypothesis a series of nanoparticle synthesis batches were conducted by varying the above parameters between pre-set levels, and the combination of these levels and their factors was studied using SAR as the response variable. As a result, we found out that there was an optimal point at which SAR was significantly higher than the values we obtained during the preliminary experiments. Such point was observed when the synthesis temperature was 85°C, total iron concentration was 0.30 M and when a high-energy ultrasound probe was used in the peptization step. In terms of SAR, values up to 1,048 W/g<sub>Fe</sub> (341 kHz, 36.5 kA/m, ILP = 2.3) were obtained, which represents one of the highest values reported for iron oxide particles synthesized by co-precipitation without size-selective fractionation. Interestingly, when fixed in an agarose matrix, our particles heated up to 719 W/g<sub>Fe</sub> (341 kHz, 36.5 kA/M, ILP = 1.6), demonstrating that they were capable of significant rates of energy dissipation even when restricted from physical rotation. Reduction in energy dissipation rate due to immobilization has been identified as an obstacle to clinical translation of magnetic hyperthermia. Additional experiments were conducted using the experimental conditions identified as optimal, and high SAR values were consistently obtained, inside the limits predicted by the statistical analysis. Hence, we believe the particles we obtained while systematically optimizing both the synthesis and peptization steps, have a great potential for application in nanoscale thermal cancer therapy.

## 2.3 Experimental section

### 2.3.1 Materials

Iron (II) chloride tetrahydrate ( $\text{FeCl}_2 \cdot 4\text{H}_2\text{O}$ ) 99%, iron (III) chloride hexahydrate ( $\text{FeCl}_3 \cdot 6\text{H}_2\text{O}$ ) 99%, tetramethylammonium hydroxide (TMAOH) 25% w/v, agarose high melting point, hydroxylamine hydrochloride, sodium acetate, 1,10-phenantroline monohydrate, oleic acid, ICP iron standard, toluene, diethyl ether and acetone were purchased from Sigma-Aldrich (St. Louis, MO). Ammonium hydroxide ( $\text{NH}_4\text{OH}$ ) 29% v/v, nitric acid 70% v/v (Optima grade) and ethanol absolute were purchased from Fisher Scientific (Hampton, New Hampshire). All reagents were used as received.

### 2.3.2 Synthesis of iron oxide nanoparticles

All the different synthesis batches were carried using a scheme similar to that described by Herrera *et al.*<sup>29</sup> with modifications to incorporate the effect of the studied factors. Deionized water was degassed by vigorously bubbling nitrogen for at least 30 minutes and used to prepare aqueous solutions with different concentrations of iron (II) and iron (III) salts. The total iron concentration ( $\text{Fe}^{2+} + \text{Fe}^{3+}$ ) was varied between experiments, but the molar ratio  $\text{Fe}^{3+}/\text{Fe}^{2+}$  was kept constant at 2:1. Iron solutions were sonicated in a bath for 20 min, degassed for 5 minutes and mixed in a small 250 mL glass reactor. The reaction mixture was heated and then  $\text{NH}_4\text{OH}$  was added to the reactor, followed by one-hour reaction at the studied temperatures (80, 85 or 90°C). The pH was kept between 8.0 and 9 by adding small aliquots of  $\text{NH}_4\text{OH}$  throughout the reaction. The resultant iron oxide solution was cooled to room temperature, poured into conical tubes, centrifuged (1,500 rpm for 10 min) and then magnetically decanted. All syntheses were run in duplicate.

### **2.3.3 Peptization of iron oxide nanoparticles**

Three different schemes were used for peptization of nanoparticles, using tetramethylammonium hydroxide 25% (w/v) (TMAOH) as the peptizing agent. TMAOH was added to conical tubes containing the iron oxide (IO) nanoparticle precipitate using different IO/TMAOH volume ratios (0.5, 1 and 2). Tubes were homogenized by vortexing to disperse the iron oxide nanoparticles in the peptizing agent. Peptization was accompanied by sonication, using either a bath sonicator (FS110D, Fisher Scientific) or an ultrasound probe (XL2020, Misonix Inc.) for different time periods (20 – 60 minutes). Peptized nanoparticles were centrifuged and magnetically decanted, and then the obtained colloid was air-dried overnight. Afterwards, dried nanoparticles were suspended in water to yield aqueous nanoparticle solutions at a concentration of 100 mg/mL, which were used as stock solutions for further use. These suspensions were stored at 4°C.

### **2.3.4 Surface modification of nanoparticles**

After peptization, bare nanoparticles were coated with a hydrophobic layer of oleic acid which was subsequently exchanged by silanized polyethylene glycol (PEG-Silane). The oleic acid adsorption and the ligand exchange reaction were performed according to experimental protocols described elsewhere with slight modifications<sup>30,31</sup>. Aqueous suspensions of bare nanoparticles (25 mg/mL) were mixed with oleic acid using a 1:15 mass ratio, homogenized using a high-energy ultrasonicator for 15 minutes, and heated at 50°C for two hours under moderate stirring conditions. The mixture was washed with ethanol absolute, magnetically decanted, dried in a vacuum oven at room temperature, and subsequently, dispersed in toluene. OA-coated nanoparticles were mixed with PEG-Silane previously dissolved in toluene, using a

polymer mass excess of 5X with respect of nanoparticle mass. The nanoparticle/PEG-Silane mixture was stirred at room temperature for 72 hours, washed with cold diethyl ether and magnetically decanted. PEG-coated nanoparticles were dried in a vacuum oven at room temperature. PEG-Silane was synthesized following a scheme similar to the reported by Herrera *et al.*<sup>32</sup>, using PEG chains with molecular weight of 2 and 5 kDa.

### **2.3.5 Nanoparticle characterization**

The stock solutions mentioned before were used to prepare diluted nanoparticle suspensions for characterization purposes, using ultra-sonication for 20 minutes after the diluted suspension was prepared. Most of these characterizations were carried out with suspensions of 10 mg/mL, except for transmission electron microscopy (TEM) and dynamic light scattering (DLS), which used concentrations of 60 and 0.1 mg/mL, respectively. In addition, bath-sonication of samples was carried out for at least 20 minutes prior to each characterization technique.

#### **2.3.5.1 Dynamic light scattering and zeta potential**

Hydrodynamic diameters were determined through room temperature dynamic light scattering (DLS), using a particle size analyzer (Zeta PALS, Brookhaven Instruments, Holtsville, NY). Aqueous nanoparticle samples (500  $\mu$ L) with concentration between 0.1 and 1 mg/mL were filtered using a 0.2  $\mu$ m nylon syringe filter prior to measurements. The log-normal distribution of the volume-weighted measurements was used to obtain the mean hydrodynamic diameter and geometric deviation. The surface charge of PEG-coated nanoparticles was determined measuring the zeta potential of nanoparticles at different pH values, using phase analysis light scattering (PALS). Diluted nanoparticle suspensions in aqueous 1 mM KNO<sub>3</sub> were filtered using a 0.22  $\mu$ m

syringe filter disk, and then the pH was adjusted between 2 and 12 by adding 0.1 M KOH and HNO<sub>3</sub>.

### **2.3.5.2 Dynamic magnetic susceptibility**

The mechanism of magnetic relaxation of the nanoparticles was evaluated via dynamic magnetic susceptibility (DMS) measurements using a susceptometer (DynoMag, RISE, Kista, Sweden), in a frequency range of 1 Hz to 160 kHz at an applied field amplitude of 0.5 mT (5 G). A 200  $\mu$ L aliquot of aqueous nanoparticle suspension was used for analysis of liquid samples; the same volume was used for nanoparticles fixed in a 1.5% w/v agarose solution to analyze particles with restricted physical rotation. The agarose solution was prepared by dissolving 3 mg of high-melting point agarose in 200  $\mu$ L of aqueous nanoparticle suspension (10 mg/mL) in a glass vial. The vial was placed in a bath-sonicator at 65°C for 1 hour, to allow complete dissolution of agarose. The vials were then placed in an ice bath for a few seconds and then left to reach room temperature to obtain a solid matrix.

### **2.3.5.3 Magnetic measurements**

Equilibrium magnetic measurements were performed using a superconducting quantum interference device (SQUID) magnetometer (MPMS3, Quantum Design, San Diego, CA). One hundred microliters of sample were used to obtain magnetization curves at 300 K and magnetic field between -7 and 7 T. From these curves, the experimental saturation magnetization was obtained by averaging seven points in the maximum magnetization region. The magnetic diameter of the nanoparticles was obtained by fitting the experimental data to the Langevin model weighted using a lognormal size distribution. The blocking temperature of the samples was obtained from so-called zero-field cooled (ZFC) and field cooled (FC) curves of temperature

dependence of the magnetization at 10 Oe, in the temperature range of 4 to 400 K. Nanoparticles in powder form (10 mg) were used for this purpose. The blocking temperature was determined from the maximum of the ZFC curve, obtained using a polynomial fit to the data in that region.

#### **2.3.5.4 Iron quantification**

The iron content in liquid suspensions of nanoparticles was determined using a colorimetric assay based on complexation of  $\text{Fe}^{2+}$  with 1,10-phenanthroline. Ten microliters of aqueous nanoparticle suspension (10 mg/mL) were digested overnight at 101°C with 1 mL of 70% nitric acid (Optima Grade, Fisher Scientific) using a dry block. Subsequently, ten microliters of digested sample were evaporated at 115°C for 30 minutes, followed by addition of 46  $\mu\text{L}$  of deionized water and 30  $\mu\text{L}$  of hydroxylamine hydrochloride (8.06M). The mixture was left to react for 1 hour to reduce  $\text{Fe}^{3+}$  to  $\text{Fe}^{2+}$ . After iron reduction, 49  $\mu\text{L}$  of sodium acetate (1.22 M) was added, followed by 75  $\mu\text{L}$  of 1,10-phenanthroline monohydrate (13 mM). One hundred microliters of each sample were run in a UV-Vis spectrophotometer (UV-2600, Shimadzu Scientific Instruments, Inc., Kyoto, Japan) at 508 nm. The obtained absorbance values were used to determine the iron concentration, using a standard calibration curve. Samples and calibration standards were run in triplicate.

#### **2.3.5.5 Energy dissipation rates and specific absorption rate**

The rate of energy dissipation of nanoparticles (both in liquid and solid matrices) was obtained by exposing samples to an alternating magnetic field produced by the coil of an induction heater (EasyHeat 8310 LI, Ambrell, Hengelo, Netherlands). Liquid samples consisted of 200  $\mu\text{L}$  of aqueous nanoparticle suspension in a glass vial placed inside a glass test tube. The test tube was then positioned inside an eight-loop coil (1.2" diameter x 3.25" length). A cooling

jacket was used to thermally isolate the sample from the coil and to control the starting temperature of the measurement. A fiber optic temperature probe was used to record the temperature rise of the sample at 0.2 s intervals after the magnetic field was turned on. Another probe recorded the temperature of the coil, and during all experiments the coil temperature was lower than the sample and jacket temperature. All measurements were run in triplicate, at 36.5 kA/m and 341 kHz. Changes in temperature of the samples were recorded for a total of 120 seconds. Blanks were run to verify that there was no indirect heating of the samples. There is debate in the literature regarding the most appropriate method of quantifying the specific absorption rate (SAR) of magnetic nanoparticles. Some authors contend that measurements must be done under adiabatic conditions to ensure the measurement is accurate<sup>33</sup>, whereas others have attempted to quantify the relative rates of energy dissipation by the particles and loss to the surroundings<sup>34</sup>. In our case we follow the recommendations of Fortin *et al* who indicated that because thermal exchange with the surroundings is negligible for a sample in thermal equilibrium the SAR can be readily obtained from the initial rate of temperature rise immediately after turning on the alternating magnetic field<sup>11</sup>. As such, we calculated SAR according to the relation

$$SAR = C_P \frac{m_s}{m_{Fe}} \left. \frac{\Delta T}{\Delta t} \right|_{t \rightarrow 0} \quad (1)$$

where  $m_s$  is the mass of the sample,  $m_{Fe}$  is the mass of iron in the sample,  $C_P$  is the heat capacity of the solvent, which in the case of liquid samples was water ( $C_P = 4.185 \text{ J/}^\circ\text{C}\cdot\text{g}$ ) and in the case of solid samples was agarose 1.5% w/v ( $C_P = 3.90 \text{ J/}^\circ\text{C}\cdot\text{g}$ )<sup>35</sup>, and  $\Delta T/\Delta t$  is the initial slope of the time-dependent heating curve. The iron concentration was obtained through the colorimetric assay.

### **2.3.5.6 Physical diameter**

The size and shape of nanoparticles, both inorganic cores and PEG-coated, were determined via transmission electron microscopy (TEM), using nanoparticle suspensions with concentrations of 60 mg/mL. Carbon-coated copper grids were immersed in the nanoparticle suspensions and dried in an oven at 60°C for 15 minutes. Images were recorded using a transmission electron microscope (200CX, JEOL, Akishima, Japan) and analyzed by counting at least 200 particles per image (ImageJ 1.48v, NIH). A log-normal size distribution was used to obtain the number-weighted mean core diameter and geometric deviation.

### **2.3.5.7 Weight percentage of iron oxide core**

The weight percentage of both iron oxide core and PEG-Silane on the particle surface was determined via thermogravimetric analysis (TA Instruments Q 6000 STD, New Castle, DE), under a nitrogen atmosphere. Powder nanoparticle samples were heated from room temperature to 800°C at 20°C/min with 10 min isothermals at 200°C and 600°C for maximal desorption/decomposition of organic components. The mass loss of the polymer was recorded during the heating ramps as a function of time, and expressed as a weight percentage with respect of the initial mass of nanoparticle sample.

### **2.3.6 Experimental design and statistical analysis**

A full factorial experimental design with three factors and three center points was used to study the contribution of the studied factors at three different levels. For this design, a total of 15 synthesis runs were considered for each combination of factors and their levels, and each run was conducted in duplicate (A and B) for a total of 30 independent experiments. Factors and their

levels are summarized in Table 2.2, and the complete set of experimental runs and their combinations is shown in Table 2.3. Data were analyzed by means of the Surface Response Method (RSM) using the SAR value as response variable, and the objective of the optimization routine was to determine the optimal conditions to obtain SAR values as high as possible. R3.1.1 was used to process data and obtain all statistical information<sup>36</sup>.

**Table 2.2.** Factors and levels for the optimization study.

<b>Factor</b>	<b>Low level</b>	<b>Mid-level</b>	<b>High level</b>
Temperature (°C)	80	85	90
Total Iron Concentration (M)	0.08	0.30	1.00
Peptization	Bath-Sonication	Bath/ Ultra-Sonication	Ultra-sonication

**Table 2.3.** Experimental design for the optimization of SAR

Synthesis run (each with two replicates named A & B)	Factor-level combinations		
	Temperature	Iron concentration	Peptization
1	Low	Medium	Low
2	Low	Medium	High
3	High	Medium	Low
4	High	Medium	High
5	Medium	Low	Low
6	Medium	Low	High
7	Medium	High	Low
8	Medium	High	High
9	Low	Low	Medium
10	High	Low	Medium
11	Low	High	Medium
12	High	High	Medium
13	Medium	Medium	Medium
14	Medium	Medium	Medium
15	Medium	Medium	Medium

## 2.4 Results and discussion

This section includes results of nanoparticle characterization, optimization of synthesis conditions and reproducibility studies. From this moment on, the nomenclature used in discussion of results refers to as to “run” each of the 15 synthesis conditions depicted in Table 2.3, and A & B represent each of the two experimental replicates for each “run”.

### 2.4.1 Particle size

From TEM analysis, nanoparticle core diameters ranging from 12 to 20 nm were obtained from different syntheses carried out following the experimental design shown in Table 2.2. The images and histograms are illustrated in Figure 2.1 for three representative runs, accounting for nanoparticles with low, intermediate and high energy dissipation rates, respectively. In the

figure,  $D_P$  represents the mean physical particle diameter (core size), and  $Ln \sigma$  is the geometric deviation of the log-normal distribution. As is usual with the co-precipitation synthesis, nanoparticles were roughly spherical, somewhat polydisperse, and there was evidence of small aggregates. It was also evident that changing synthesis and peptization conditions led to changes in the primary particle size and the prevalence of aggregates in the samples. Even when the inherent nature of co-precipitation synthesis usually yields polydisperse suspensions of particles, overall well-defined single particles with only a few aggregates can be observed. Moreover, improvements on particle dispersion were obtained after the optimization of synthesis and peptization, including reductions on aggregate sizes, especially when strong sonication conditions were used in the peptization step.

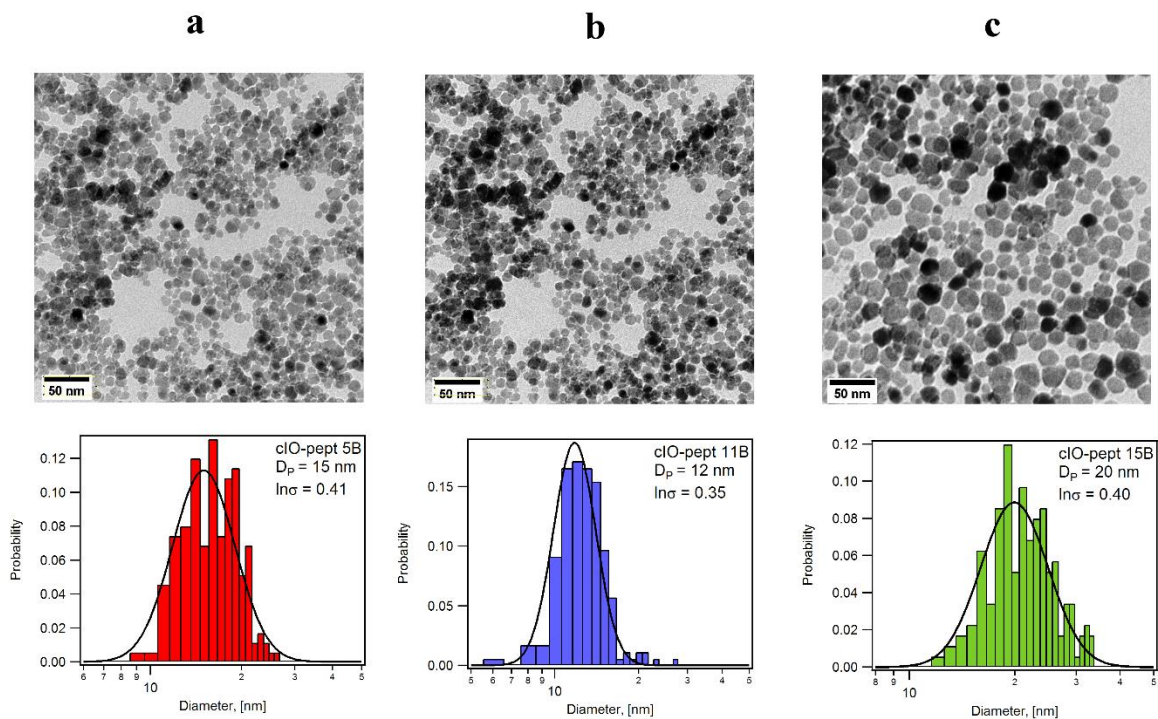


**Figure 2.1.** TEM images and size distributions of representative synthesis runs: a) 5B,  $D_P = 15 \pm 0.41$  nm; b) 11B,  $D_P = 12 \pm 0.35$  nm; c) 15B,  $D_P = 20 \pm 0.40$  nm. Continuous lines represent log-normal size distributions.

DLS measurements indicated the nanoparticles had volume-weighted hydrodynamic diameters ranging between 29 and 58 nm depending on synthesis and peptization conditions, and Figure 2.2 illustrates the log-normal distributions for three representative samples. Note that the diameters obtained from TEM are number-weighted, a factor that must be considered when comparing to the volume-weighted hydrodynamic diameters. As examples, for run 5B, the corresponding volume-weighted core diameter was 25 nm, which is smaller than the corresponding volume weighted hydrodynamic diameter of 38 nm. Similarly, for runs 11B and 15B, the volume-weighted physical diameters were 17 nm and 32 nm, and the volume-weighted hydrodynamic diameters were 36 nm and 58 nm, respectively. Because the TMAOH treatment should not significantly contribute to the hydrodynamic diameter of the particles, these larger hydrodynamic diameters were attributed to the presence of small aggregates of two or three individual particles. Similar observations applied to samples obtained under other conditions. The smallest hydrodynamic diameters were obtained for batches with low iron concentration, in agreement with previous observations by Forge *et al.*<sup>7</sup>. Overall, hydrodynamic diameters were lower when compared to those reported for nanoparticles peptized with TMOAH without any polymer coating<sup>27</sup>. The reduction in hydrodynamic diameter confirmed that the use of ultrasonication during peptization was effective in breaking larger aggregates, improving dispersion of particles.

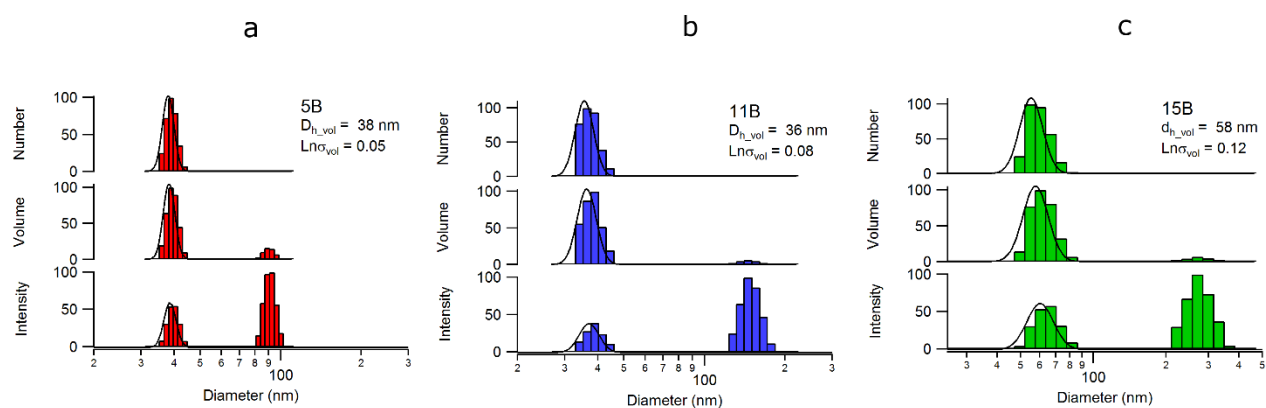


**Figure 2.2.** DLS measurements for the calculation of volume-weighted hydrodynamic diameters for three representative synthesis runs. a) 5B,  $D_h = 38$  nm,  $\text{Ln } \sigma = 0.05$ . b) 11B,  $D_h = 36$  nm,  $\text{Ln } \sigma = 0.08$ . c) 15B,  $D_h = 58$  nm,  $\text{Ln } \sigma = 0.12$ . Continuous lines represent log-normal size distributions.

## 2.4.2 Magnetic behavior

Room temperature magnetic characterization revealed nanoparticles with saturation magnetizations that were close (>83%) to the bulk value for iron, which is approximately 124.4 emu/g<sub>Fe</sub><sup>37</sup>. This implies that the method used for iron quantification was accurate. Equilibrium magnetization curves illustrated in Figure 2.3a for selected samples indicated the particles were superparamagnetic at room temperature, as no remnant magnetization was observed. By fitting the experimental magnetization values to the Langevin model weighted using a lognormal size distribution<sup>38</sup>, the magnetic diameter ( $D_m$ ) was obtained, with values ranging from 9 – 14 nm. Saturation magnetization values decreased as particles became smaller, in agreement with previous reports<sup>39,40</sup>. One possible cause is increased contribution of canting of magnetic moments on the surface of the particles<sup>41</sup>. Figure 2.3b depicts the temperature dependent magnetization under zero field-cooled (ZFC) and field-cooled (FC) conditions between 4 and 400 K. The peak of the ZFC curve represents a state where nanoparticle behavior goes from

superparamagnetism to ferromagnetism, and the temperature at which this change is observed is known as the blocking temperature<sup>42</sup>. In general terms, and as expected, an increase in blocking temperature ( $T_B$ ) was observed as particle size increased. For example, the blocking temperature was 264K for particles with a physical diameter of 12 nm, and higher than 400K for particles with a physical diameter of 20 nm. An increase in blocking temperature is expected as particle size increases due to the exponential dependence on crystal volume of the blocking temperature<sup>43</sup>.

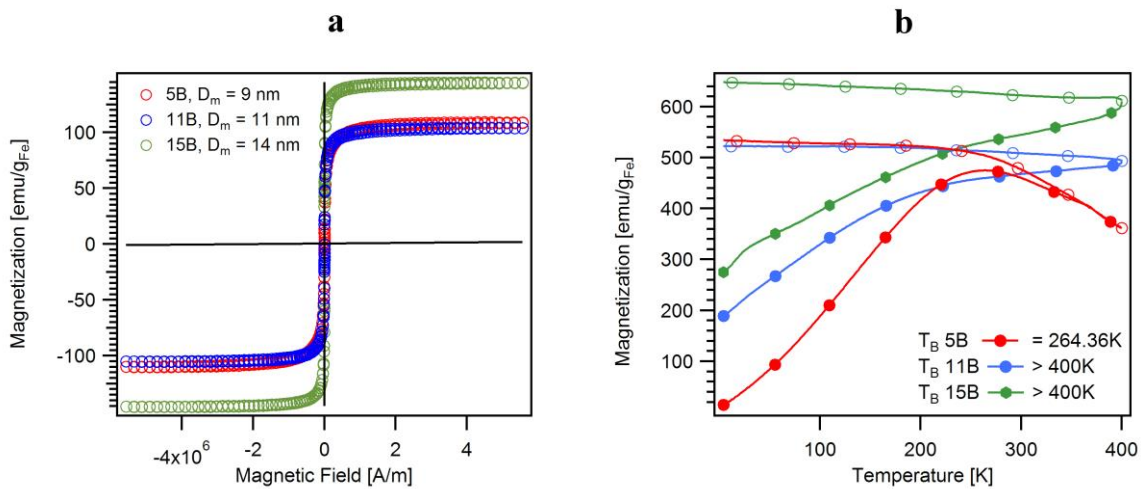


**Figure 2.3.** Magnetic characterization for representative synthesis runs. a) Equilibrium magnetization curves showing field dependence at 300K with  $M_s$  values of 109, 104 and 144 emu/g<sub>Fe</sub> for runs 5B, 11B and 15B, respectively. b) ZFC/FC magnetization curves from 4 to 400 K with  $T_B$  values of 264 K for run 5B and higher than 400K for runs 11B and 15B.

It is interesting to note that although equilibrium magnetization measurements indicated all samples are superparamagnetic at room temperature, blocking temperature values for some samples were higher than 300 K. The reason why these two techniques yield apparently

conflicting results is due to the time scales involved in each measurement, with the time scale for the ZFC-FC measurement (14 s) being shorter than the time scale than the equilibrium magnetization measurement (23 s). Hence, the blocking temperatures imply that for some samples at room temperature there is a non-negligible fraction of nanoparticles that are thermally blocked (not superparamagnetic), and should therefore contribute a Brownian relaxation component to their response to alternating magnetic fields. This was confirmed through DMS measurements, which indicated that all synthesized particles had a Brownian relaxation peak of varying intensity. Representative results are shown in Figure 2.4, for two synthesis runs (*9B* and *12B*). The presence of a peak in the out-of-phase (imaginary) component of the susceptibility at frequencies near 100 kHz (Brownian peak) was observed in all the runs, but with different peak susceptibility intensities. For particles synthesized at low iron concentration, the height of the Brownian peak decreased, while the in-phase (real) component of the susceptibility did not appear to change significantly. For run *9B*, with hydrodynamic diameter of ~29 nm and total iron concentration of 0.08M, the flat-shaped Brownian peak rises barely above  $2 \times 10^{-4}$  units of magnetic susceptibility. However, for run *12B* with total iron concentration of 1.0M and hydrodynamic diameter of ~49 nm, the Brownian peak is well defined and reaches more than  $1 \times 10^{-3}$  units of magnetic susceptibility. The distance between the curves of real and imaginary parts of the susceptibility was markedly smaller as the particle size increased, indicating a larger contribution of the Brownian relaxation mechanism.

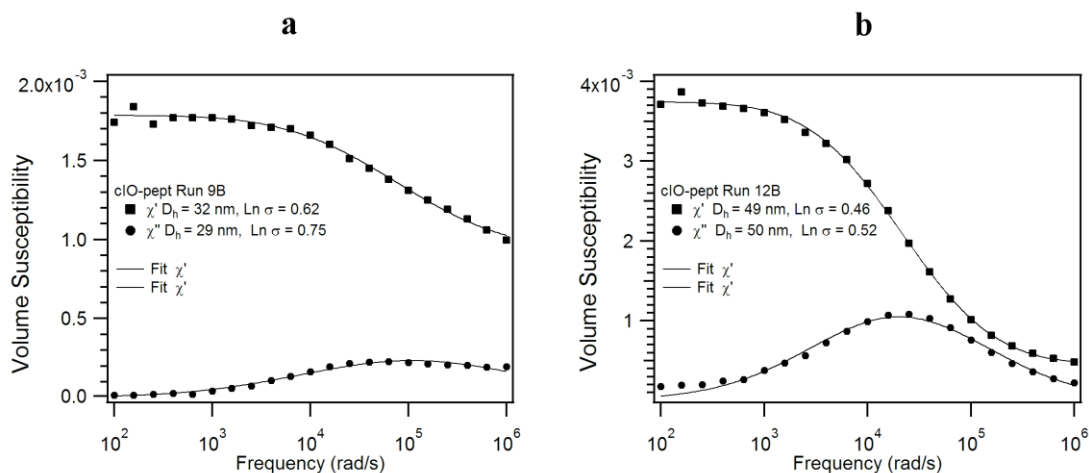


**Figure 2.4.** DMS measurements for two representative synthesis runs with different initial iron concentration. a) Run *9B* with iron concentration of 0.08M and  $D_h=32$  nm b) Run *12B* with iron concentration of 1.0M and  $D_h=50$  nm. Solid symbols represent individual measurements and continuous lines are fittings to the Langevin-Chantrell model.

Hydrodynamic diameters were also determined by fitting the Debye model to DMS measurements, using the in-phase ( $\chi'$ ) and out-of-phase ( $\chi''$ ) components of the dynamic susceptibility. Good agreement was observed when comparing hydrodynamic diameters obtained from DLS and DMS measurements, as depicted in Figure 2.5. Data points positioned along the 45° diagonal indicate quantitative agreement between hydrodynamic diameters determined from DLS and DMS measurements. It is important to note that hydrodynamic diameters obtained from  $\chi'$  and  $\chi''$  were not always the same even when the same model was applied to fit experimental data. These differences occur because the mathematical expression for  $\chi''$  has a numerator that is directly proportional to the cube of the hydrodynamic diameter, thus making  $\chi''$  more sensitive to changes in values of the hydrodynamic diameter relative to  $\chi'$ <sup>44</sup>.

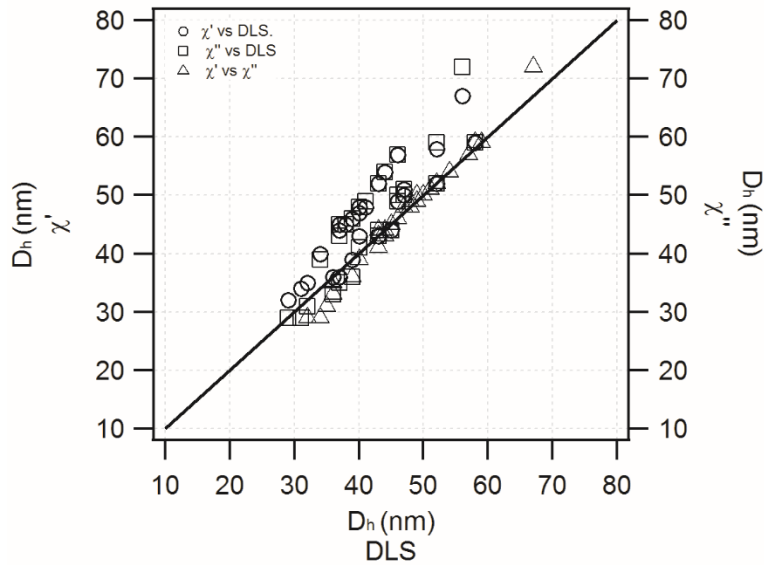


**Figure 2.5.** Parity plot for volume-weighted hydrodynamic diameters obtained from DLS and DMS measurements. Each point represents a single measurement.

### 2.4.3 SAR measurements in liquid suspensions

The SAR was calculated using the initial slope of the temperature profiles obtained under the application of the alternating magnetic field, and then normalized by iron content, according to Eq. (1). All measurements were carried out at a field amplitude of  $H_0 = 36.5$  kA/m and frequency of  $f = 341$  kHz. Figure 2.6 shows representative heating ramps of the aqueous nanoparticle suspensions including the temperature profiles of the induction coil and blank (deionized water). The initial temperature for all measurements was 25 °C, which as shown in Figure 2.6a remained unaltered for the blank in all the measurements, indicating that the sample holder was thermally isolated from the coil. The initial slope is depicted as a thick red line and was obtained by fitting a linear model to the experimental temperatures recorded during the first few seconds of heat generation. As shown in Figure 2.6b, temperature increments of up to 65 °C (corresponding to a final temperature of 90°C) were recorded for samples with the highest initial rate of temperature

rise ( $0.93^{\circ}\text{C/s}$ ), whereas temperature increments of less than  $10^{\circ}\text{C}$  were observed for other samples, for example those prepared with low iron concentration. As with many of the magnetic properties, the initial rate of temperature rise increased with particle size, with run *15B* having the highest particle size, the highest saturation magnetization, and the steepest initial rate of temperature rise. This is in agreement with previous work where the proportionality between particle size and rate of heating has been reported<sup>23</sup>.

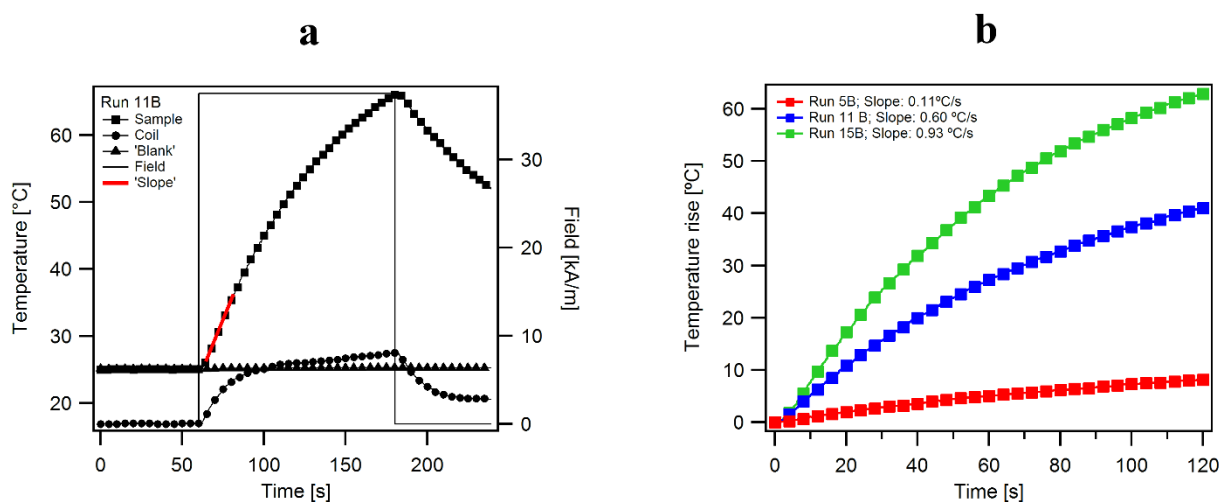


**Figure 2.6** Examples of temperature rise profiles for various samples exhibiting different heating slopes. Measurements were performed at an applied magnetic field of  $H_o = 36.5$  kA/m and  $f = 341$  kHz. Each point represents a single measurement.

A wide range of SAR values were obtained, and depended on the combination of studied factors and their levels. Figure 2.7 shows SAR values for replicates B of synthesis runs described in Table 2.3, segregated into four different groups. These groups were studied independently to understand how SAR was affected by controlling synthesis and peptization conditions. Group 1 (blue bars): SAR values obtained when working with a fixed initial iron concentration of 0.30 M. It can be noticed that SAR remained virtually unaltered by increasing the synthesis temperature

from 80°C to 90°C while keeping the same type of sonication (runs 1 and 3), but there was an improvement when ultra-sonication was used during peptization (runs 2 and 4). The use of stronger amplitudes during ultra-sonication along with higher amounts of peptizing agent, when compared to those achieved with bath-sonication, appeared to improve rupture of particle aggregates. Group 2 (brown bars): SAR values obtained by fixing the synthesis temperature at 85°C but varying the initial iron concentration from 0.08M to 1.0M, and using both bath-sonication and ultra-sonication during the peptization step. In this case, the SAR seems to be strongly affected by total iron concentration used during the reaction, while the use of ultra-sonication does not show an improvement in SAR for the same iron concentration. However, regardless of the type of sonication, there was an increase in SAR when using higher iron concentrations (runs 7 and 8), but the heat dissipation rates achieved were not as high as those achieved when using ultra-sonication along with 0.30 M of iron (i.e. run 8 vs run 4). Group 3 (orange bars): SAR values from syntheses with sonication at its medium level supports the observations made for groups 1 and 2. Even for nanoparticles with low initial iron concentration, an increase in the synthesis temperature led the SAR to rise from 235 to 409 W/g<sub>Fe</sub> (run 9 and 10). Group 4 (green bars): SAR values obtained from synthesis runs with the three factors fixed at their medium levels, and they accounted for the center points of the experimental design. These three runs, which are replicates of each other, describe the overall variability of the study described in Table 2.2, thus bars shown in Figure 2.7 do not include error bars. These runs were obtained under a synthesis temperature of 85°C, 0.30M of initial iron concentration and peptization using both bath-sonication and ultra-sonication with Fe<sub>3</sub>O<sub>4</sub>/TMAOH in 1:1 volume ratio. Notably, this group yielded the highest SAR values for the entire set of synthesis runs, with energy dissipation rates of up to 1,048 W/g<sub>Fe</sub> (run 15). The high SAR values observed for these

samples were in fact, improvements of those obtained under similar conditions observed in other groups (i.e. runs 4 and 12), demonstrating that the use of ultra-sonication during the peptization of particles is key to improving heat dissipation rates.

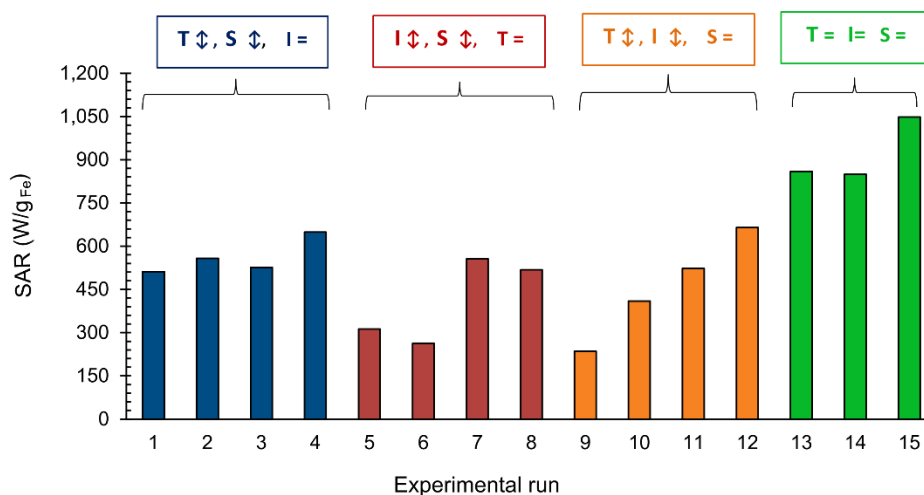


**Figure 2.7.** Comparison of SAR values of synthesis runs described in Table 2.3. Blue bars: Temperature and sonication at fixed iron concentration. Brown bars: Iron concentration and sonication at fixed temperature. Orange bars: Temperature and iron concentration at fixed sonication type. Green bars: Temperature, iron concentration and sonication at their medium levels. These three bars are the center points of the experimental design thus describing the overall variability.

As stated before, the ILP value is a convenient metric of the energy dissipation rate of iron oxide nanoparticles that allows for comparisons between nanoparticles characterized under different magnetic field conditions. In this work, values of up to  $2.3 \text{ nH}\cdot\text{m}^2\cdot\text{kg}^{-1}$  were obtained at 36.5 kA/m and 341 kHz. At the time this work was conducted, this ILP exceeded the values reported by others at similar field strengths and frequencies around 500 kHz. In fact, reported

ILP values for heat dissipation with frequencies around 500 kHz are typically below  $1 \text{ nH}\cdot\text{m}^2\cdot\text{kg}^{-1}$  with some exceptions between 4 and  $5 \text{ nH}\cdot\text{m}^2\cdot\text{kg}^{-1}$ <sup>48</sup>, and one notable recent study reporting an ILP value of  $8.7^{26}$ . Improvements on SAR under the optimized synthesis and peptization conditions is attributed to the incorporation of high energy ultra-sonication during the peptization step which induced the rupture of large aggregates. This occurred simultaneously with the adsorption of tetramethylammonium cations to the surface of the nanoparticles, In this scenario, by having smaller aggregates of single cores the surface-to-volume ratio would increase, which would require more peptizing agent to be adsorbed onto those aggregates, improving the stability of the particles. Therefore, more stable nanoparticle suspensions coupled to smaller hydrodynamic diameters led to an enhancement in heat dissipation rate. According to discussions of the relationship between SAR and particle size, lower heat dissipation rates for smaller particles are expected. This is confirmed by analyzing the hydrodynamic diameters of runs with low iron concentration (runs 5, 6, 9 and 10), which had the smallest hydrodynamic diameters among all the synthesis runs, and the lowest SAR values. A similar tendency was observed for runs with high iron concentration (runs 11 and 12), though the increase in SAR is slightly less for the same temperature increase. However, by increasing simultaneously the temperature and iron concentration during synthesis, SAR was increased by almost a factor of three, relative to the value when both factors were at their low levels (run 9 vs run 12). Moreover, it was observed that ultra-sonication increases SAR, but the simultaneous combination of iron concentration and temperature at the studied medium levels showed a synergistic effect that was not observed when these two factors had lower or higher values.

#### **2.4.4 SAR measurements in solid matrices**

Confinement of nanoparticles in intracellular vesicles and in biological tissues may limit their free rotation, which has been reported to cause a reduction in the total amount of heat dissipated<sup>45</sup>. Thus, SAR measurements in solid matrixes were carried out because they provide an estimate of the reduction in energy dissipation rate in the complex biological environment. For this purpose, we fixed nanoparticles in agarose gel and applying a magnetic field with the same intensity and frequency as used for liquid suspensions. Immobilization of particles in agarose gel was confirmed using DMS measurements, as depicted in Figure 2.8, which presents a comparison between the magnetic susceptibility of the particles suspended in water and immobilized in agarose gel for the same synthesis run. The characteristic peak of the out-of-phase component of the susceptibility, namely the Brownian peak, shows a marked reduction when particles are fixed in the solid matrix. Similar observations indicated that most of the Brownian particles were restricted from physical rotation, showing a flat curve for the out-of-phase component.

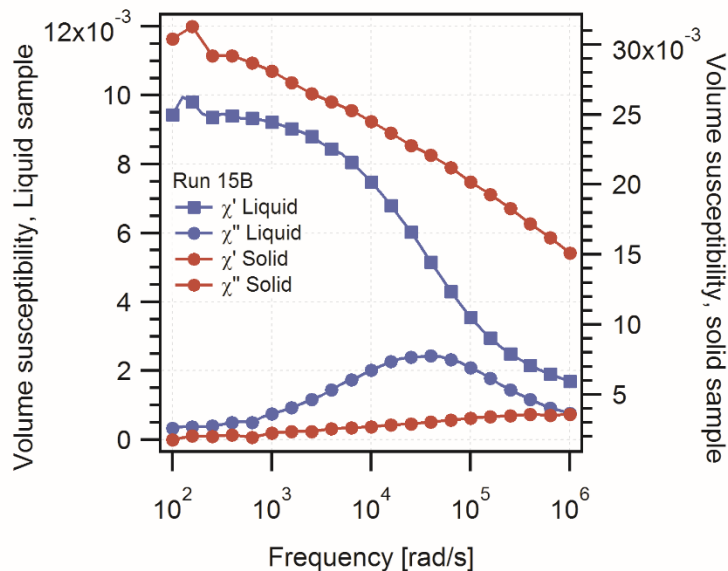


**Figure 2.8.** DMS plot for run 15B comparing data from liquid suspensions (blue markers) and data from particles fixed in agarose gel (brown markers). Each point represents a single measurement.

The immobilization of particles revealed a decrease in SAR when compared to the values reached by liquid suspensions for the same synthesis run. This reduction was attributed to suppression of the Brownian relaxation mechanism. This situation is depicted in Figure 2.9a wherein the SAR values for both liquid and solid particle preparations are presented for all synthesis runs. It is important to note that even when the total amount of heat dissipated was reduced when fixing the particles in the agarose gel, the remaining fraction still resulted in excellent SAR values. Some of the SAR values obtained for nanoparticles in solid matrices are even higher than those in liquid suspensions obtained by our research group in the past<sup>24,49</sup>. Exceptional heat dissipation rates of up to 719 W/g<sub>Fe</sub> were achieved for the immobilized nanoparticles, indicating that they are promising candidates for *in vivo* MFH application. In fact, the maximum SAR values in solid matrices reported here were higher than those reported for

liquid suspensions by other groups<sup>10</sup>. Figure 2.9b also compares the SAR and ILP values obtained under restricted nanoparticle rotation in our work with that of other representative publications. It is important to note that even when some groups report exceptionally high ILP values, care must be taken to confirm that conversion of SAR into ILP is properly done. For this purpose, it is necessary to ensure that the magnetic response of the nanoparticles is linear with the applied magnetic field. A comparison can be done between the maximum applied magnetic field amplitude and the magnetic field at which the saturation magnetization was achieved; the first must be much smaller than the latter<sup>26</sup>. In this work, from SQUID measurements the saturation magnetization was reached above 4000 kA/m, and this value is 100 times higher than the field amplitude applied during measurements, meeting the corresponding requirements of magnetic linear response.

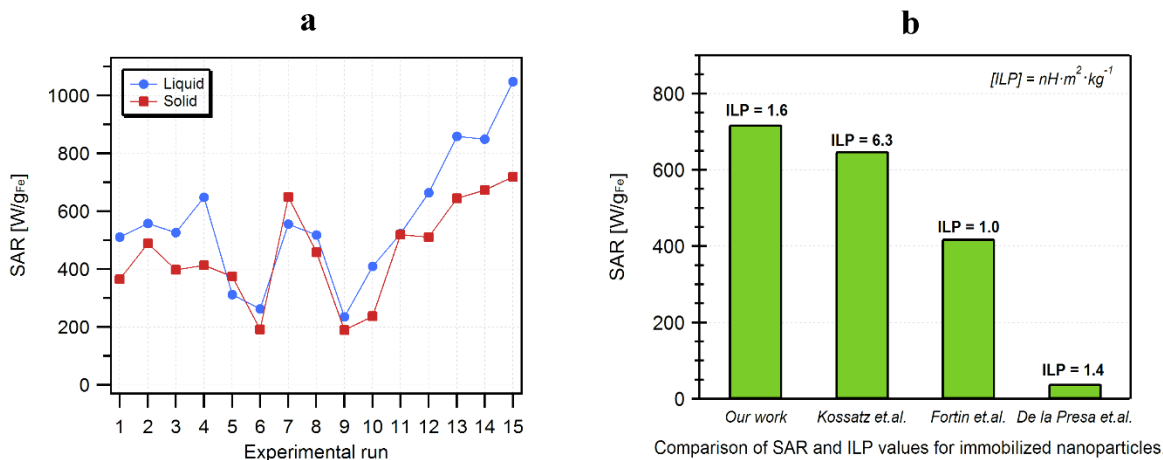


**Figure 2.9.** SAR values for particles immobilized in solid matrices. a) Comparison between suspended (blue markers) and agarose-fixed (maroon markers) nanoparticles for the different synthesis runs. b) Comparison of SAR and ILP values between our immobilized particles and those reported by other research groups<sup>11,23,26</sup>

#### 2.4.5 Optimization and reproducibility

Optimal experimental conditions were identified to produce nanoparticles with high heat dissipation rates by using the Response Surface Method (RSM)<sup>46</sup>. As discussed before, optimal results were those obtained when the temperature, iron concentration and peptization were at their medium levels. These results were optimized, and they are depicted in the contour plot shown in Figure 2.10a, which relates the different SAR values that can be obtained by moving along the different levels of temperature and iron concentration. The contour black lines represent the wide range of SAR values that were shown earlier in Figure 2.7, and the red lines represent the hydrodynamic diameters at which SAR can be obtained. The purpose to incorporate particle sizes in the contour plot is to provide a practical way to relate a factor, which was not part of the experimental design, but is a parallel consequence of modifying the experimental conditions. In addition, even when a set of conditions was experimentally found to maximize SAR, there is an optimum region under which high SAR values can be consistently obtained within some limits, while reducing variability. This region was evaluated by conducting new synthesis runs shown in Figure 2.10b where SAR is plotted versus synthesis runs under the optimized conditions. The eight syntheses are replicates of each other, and all of them were carried out using ultra-sonication during the peptization step. Another important aspect of the optimization is the establishment of the prediction interval; a predicted range for SAR values in subsequent experiments. The lower and upper limits of this interval are shown as horizontal red lines. As demonstrated, all SAR values obtained in this new series of experiments were inside the prediction interval, suggesting that the RSM successfully predicted the range of SAR values that can be obtained under optimal conditions.

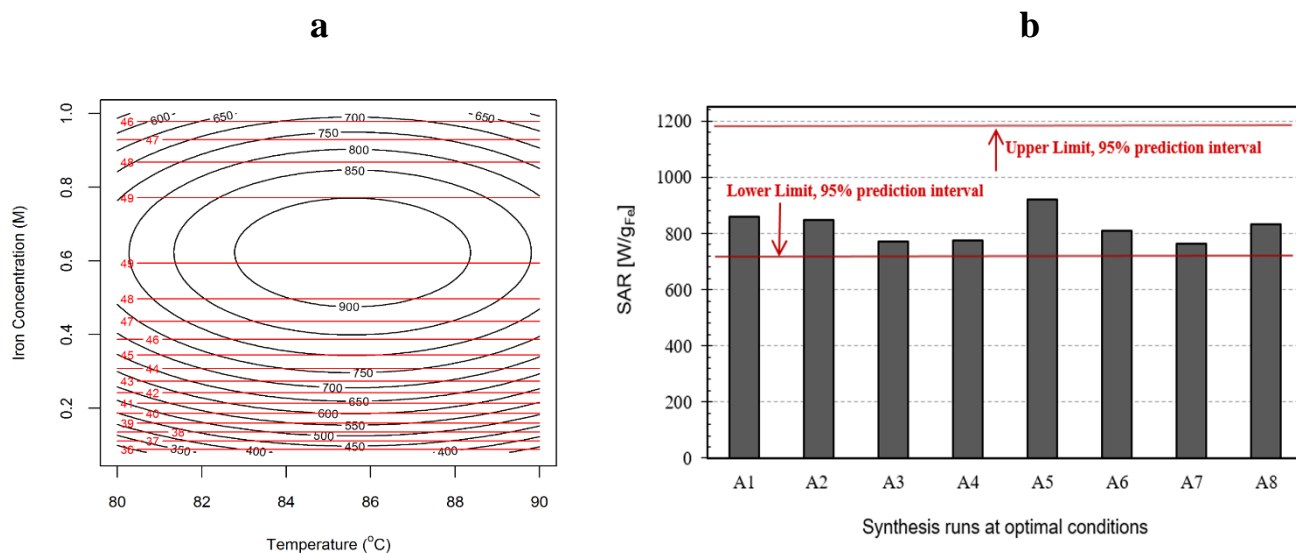


**Figure 2.10.** a) Contour plot of the response surface for SAR, b) Evaluation of the predicted behavior of SAR under optimized conditions by means of additional synthesis runs.

#### 2.4.6 Characterization of PEG-coated nanoparticles

Coating bare iron oxide nanoparticles with PEG-Silane had three main purposes: i) improve particle dispersion and stability in water and other biological media, ii) provide functionality for the conjugation of molecules, and iii) confer biocompatibility to nanoparticles for their use *in vitro* and *in vivo*. The physicochemical properties of PEG-coated nanoparticles were evaluated, including particle size, surface charge and the amount of polymer grafted to particles. Results are shown in Figure 2.11 for nanoparticles coated with PEG molecular weight 2 kDa and k 5Da. From TEM analysis it was found that the physical diameter of nanoparticles is 15 nm agrees with the range of physical size obtained for uncoated nanoparticles, discussed in section 2.4.1. It was also observed an overall improvement in the dispersion of nanoparticles when compared to TEM pictures obtained for peptized nanoparticles. Such improvement in particle dispersion is attributed to the layer of polymer grafted to the particle, providing steric repulsion between

particles. Hydrodynamic diameters obtained from DLS measurements revealed particle sizes of ~ 50 - 60 nm after the coating. When comparing these hydrodynamic diameters to those of uncoated nanoparticles, an increase of 10 – 15 nm was observed. Such increase is attributed to the presence of PEG polymer chains which explains the difference in particle size after the coating with PEG. Similar observations have been reported by others, using the same method for the ligand exchange of PEG-Silane. For example, Barrera *et al.* reported an increase of about 13 nm for iron oxide nanoparticles coated with PEG-Silane of molecular weight 2 kDa with respect of the uncoated inorganic cores<sup>47</sup>. The presence of the polymer was quantitatively determined using TGA, which revealed that particles coated with PEG-Silane molecular weight 2 kDa were comprised by approximately 18% weight of iron oxide. The remaining percentage corresponds to the PEG-Silane grafted to the particle, traces of organic solvent used during ligand exchanges and unbound polymer. For nanoparticles coated with PEG chains of molecular weight 5 kDa, it was found that the iron oxide core is approximately 9%, which was also confirmed using UV iron quantification. The reason why particles coated with PEG 5 kDa had higher weight percentage of polymer is due to the increased length of the polymer chain when compared to 2 kDa, which provides higher graft density thus more mass of polymer bound to the particle. Such differences between the two molecular weights were also observed when studying the surface charge of the particles. Zeta potential measurements revealed that PEG-coated nanoparticles are essentially neutral at pH 7, for both molecular weights, 2 and 5 kDa, respectively. This is an indication of low fractions of amine groups in the structure of the polymer coating, due to the silanol groups, and it can be confirmed by analyzing the zeta potential at pH values higher than 7. For example, at pH 12 particles coated with PEG 5 kDa remain neutral whereas those coated with PEG 2 kDa become negative because of the higher presence of deprotonated amine groups.

These findings have also been reported by others for PEG-Silanes of the same molecular weights and methods for PEG-Silane synthesis and ligand exchange similar to those used in this work.

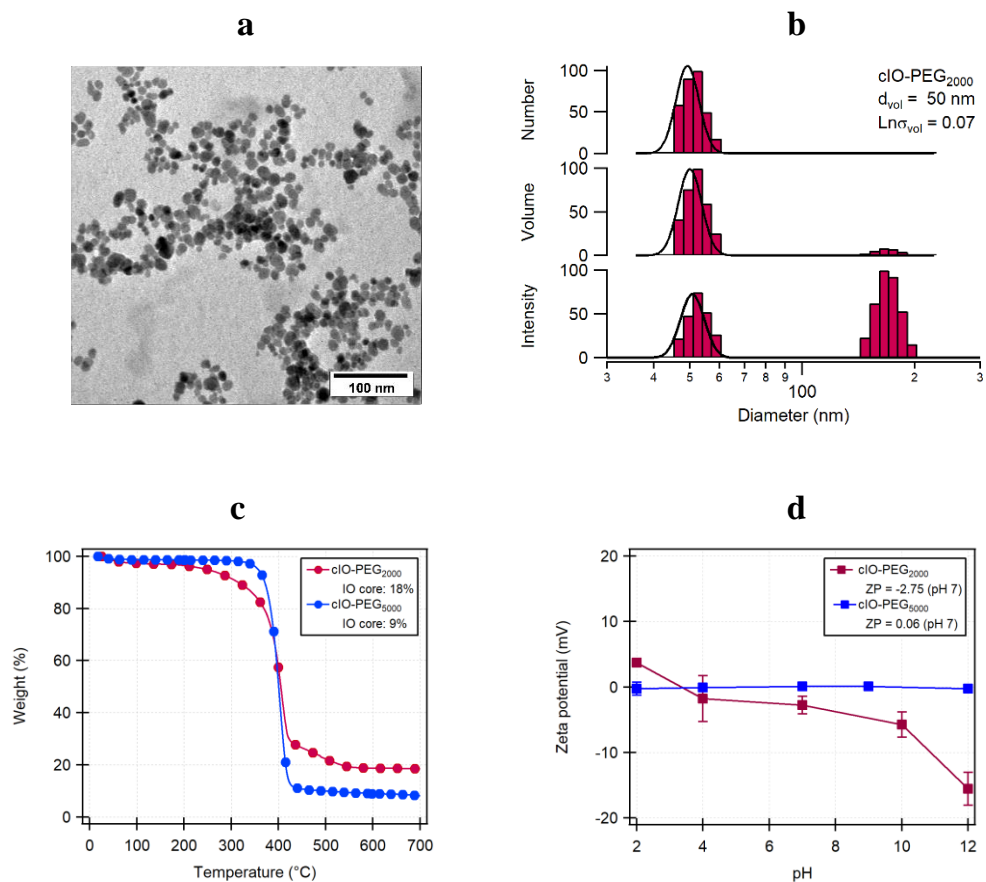


**Figure 2.11.** Characterization of PEG-coated nanoparticles. a) TEM image;  $D_p = 16$  nm, b) DLS measurements;  $D_h = 50$  nm, c) TGA curves; iron oxide core between 9 and 18%, d) zeta potential measurements at various pH values.

In addition, colloidal stability of PEG-coated nanoparticles was monitored at room temperature in various biological media, using DLS measurements. Results are presented in Table 2.4 as volume-weighted hydrodynamic diameters measured for 72 hours. As shown, PEG-

coated nanoparticles had excellent colloidal stability patterns, showing no aggregation phenomena in water, cell culture media, phosphate buffered saline (PBS) solution and sodium chloride 0.9%. These results confirm that surface modification with PEG-Silane yielded nanoparticles with good graft density, providing nanoparticles with the required steric repulsion to avoid particle aggregation.

**Table 2.4.** Colloidal stability of PEG-MNPs in biological media

Timepoint (h)	Volume-weighted hydrodynamic diameter (nm)				
	Water	PBS	DMEM <sup>1</sup> / FBS	RPMI <sup>2</sup> / FBS	NaCl 0.9%
0	50	45	48	41	45
24	42	48	46	43	43
48	41	42	44	47	49
72	39	39	*	37	43

<sup>1</sup> RPMI 1640 cell culture medium supplemented with 15% fetal bovine serum (FBS)

<sup>2</sup> DMEM cell culture medium supplemented with 10% FBS

\* Mold growth

## 2.5 Conclusions

Superparamagnetic iron oxide nanoparticles with exceptionally high heat dissipation rates were obtained *by using a simple, cost-effective and straightforward co-precipitation method*, along with an ultrasonic-assisted and enhanced peptization step. No post-synthesis treatments, size-selective separations, toxic metals or organic solvents were employed throughout the course of the experimental work, demonstrating that the simple co-precipitation protocol can be improved by tailoring key physicochemical parameters. The use of a high-energy ultrasound

probe during peptization of the nanoparticles allowed for improvements in particle dispersion, breaking the larger clusters to yield small particle aggregates which were stabilized by adsorption of tetramethylammonium hydroxide cations. Experimental observations were used to determine an optimal region under which the values of SAR can be successfully predicted, and subsequent experimentation demonstrated that SAR values were obtained as predicted and in a reproducible fashion. The achieved high heat dissipation rates were observed even when particles were fixed in agarose gel, chosen to mimic biological environments such as intracellular organelles and body tissues. In such rotation-restricted matrices, the best-performing nanoparticles dissipated up to 719 W/g<sub>Fe</sub>, a high value in comparison to other studies of heating with particles restricted from physical rotation. Overall, the reported SAR values, both in liquid suspensions and in agarose gels, exceed most values published so far for similar co-precipitation synthesis approaches to produce superparamagnetic iron oxide nanoparticles. In addition, coating nanoparticles with PEG-Silane synthesized in our laboratory led to stable colloidal dispersions in various biological media, suggesting that these particles are excellent candidates for magnetic hyperthermia applications.

## 2.6 References

1. Mérida, F. *et al.* Optimization of synthesis and peptization steps to obtain iron oxide nanoparticles with high energy dissipation rates. *J. Magn. Magn. Mater.* **394**, (2015).
2. Rosensweig, R. E. Heating magnetic fluid with alternating magnetic field. *J. Magn. Magn. Mater.* **252**, 370–374 (2002).
3. Yah, C. S., Simate, G. S. & Iyuke, S. E. Nanoparticles toxicity and their routes of exposures. **25**, 477–491 (2012).

4. Vayssières, L., Chanéac, C., Tronc, E. & Jolivet, J. P. Size Tailoring of Magnetite Particles Formed by Aqueous Precipitation: An Example of Thermodynamic Stability of Nanometric Oxide Particles. *J. Colloid Interface Sci.* **205**, 205–212 (1998).
5. Riaz, S., Bashir, M. & Naseem, S. Iron Oxide Nanoparticles Prepared by Modified Co-Precipitation Method. *IEEE Trans. Magn.* **50**, 1–4 (2014).
6. Ozkaya, T. *et al.* Synthesis of Fe<sub>3</sub>O<sub>4</sub> nanoparticles at 100°C and its magnetic characterization. *J. Alloys Compd.* **472**, 18–23 (2009).
7. Forge, D. *et al.* Optimization of the Synthesis of Superparamagnetic Contrast Agents by the Design of Experiments Method. *J. Phys. Chem. C* **112**, 19178–19185 (2008).
8. Babes, L., Denizot, B., Tanguy, G., Le Jeune, J. J. & Jallet, P. Synthesis of Iron Oxide Nanoparticles Used as MRI Contrast Agents: A Parametric Study. *J. Colloid Interface Sci.* **212**, 474–482 (1999).
9. Jolivet, J.-P., Chanéac, C. & Tronc, E. Iron oxide chemistry. From molecular clusters to extended solid networks. *Chem. Commun.* 477–483 (2004). doi:10.1039/B304532N
10. Kallumadil, M. *et al.* Suitability of commercial colloids for magnetic hyperthermia. *J. Magn. Magn. Mater.* **321**, 1509–1513 (2009).
11. Fortin, J.-P. *et al.* Size-sorted anionic iron oxide nanomagnets as colloidal mediators for magnetic hyperthermia. *J. Am. Chem. Soc.* **129**, 2628–35 (2007).
12. Hergt, R. & Dutz, S. Magnetic particle hyperthermia—biophysical limitations of a visionary tumour therapy. *J. Magn. Magn. Mater.* **311**, 187–192 (2007).
13. Bae, K. H. *et al.* Chitosan oligosaccharide-stabilized ferrimagnetic iron oxide nanocubes for magnetically modulated cancer hyperthermia. *ACS Nano* **6**, 5266–73 (2012).

14. Guardia, P. *et al.* Water-soluble iron oxide nanocubes with high values of specific absorption rate for cancer cell hyperthermia treatment. *ACS Nano* **6**, 3080–91 (2012).
15. Alphandéry, E., Faure, S., Seksek, O., Guyot, F. & Chebbi, I. Chains of magnetosomes extracted from AMB-1 magnetotactic bacteria for application in alternative magnetic field cancer therapy. *ACS Nano* **5**, 6279–96 (2011).
16. Hugounenq, P. *et al.* Iron Oxide Monocrystalline Nanoflowers for Highly Efficient Magnetic Hyperthermia. *J. Phys. Chem. C* **116**, 15702–15712 (2012).
17. Lartigue, L. *et al.* Cooperative organization in iron oxide multi-core nanoparticles potentiates their efficiency as heating mediators and MRI contrast agents. *ACS Nano* **6**, 10935–49 (2012).
18. Figuerola, A., Di Corato, R., Manna, L. & Pellegrino, T. From iron oxide nanoparticles towards advanced iron-based inorganic materials designed for biomedical applications. *Pharmacol. Res.* **62**, 126–43 (2010).
19. Lee, J.-H. *et al.* Exchange-coupled magnetic nanoparticles for efficient heat induction. *Nat. Nanotechnol.* **6**, 418–22 (2011).
20. Dronskowski, R. The Little Maghemite Story: A Classic Functional Material. *Adv. Funct. Mater.* **11**, 27–29 (2001).
21. Massart, R. Preparation of Aqueous Magnetic Liquids in Alkaline and Acidic Media. *IEEE Trans. Magn.* **17**, 1247–1248 (1981).
22. Suto, M. *et al.* Heat dissipation mechanism of magnetite nanoparticles in magnetic fluid hyperthermia. *J. Magn. Magn. Mater.* **321**, 1493–1496 (2009).
23. De la Presa, P. *et al.* Study of Heating Efficiency as a Function of Concentration, Size,

- and Applied Field in  $\gamma$ -Fe<sub>2</sub>O<sub>3</sub> Nanoparticles. *J. Phys. Chem. C* **116**, 25602–25610 (2012).
24. Rodríguez-Luccioni, H. L. *et al.* Enhanced reduction in cell viability by hyperthermia induced by magnetic nanoparticles. *Int. J. Nanomedicine* **6**, 373–80 (2011).
  25. Motoyama, J. *et al.* Size dependent heat generation of magnetite nanoparticles under AC magnetic field for cancer therapy. *Biomagn. Res. Technol.* **6**, 4 (2008).
  26. Kossatz, S. *et al.* High therapeutic efficiency of magnetic hyperthermia in xenograft models achieved with moderate temperature dosages in the tumor area. *Pharm. Res.* **31**, 3274–88 (2014).
  27. Andrade, Â. L., Fabris, J. D., Ardisson, J. D., Valente, M. a. & Ferreira, J. M. F. Effect of Tetramethylammonium Hydroxide on Nucleation, Surface Modification and Growth of Magnetic Nanoparticles. *J. Nanomater.* **2012**, 1–10 (2012).
  28. Mascolo, M., Pei, Y. & Ring, T. Room Temperature Co-Precipitation Synthesis of Magnetite Nanoparticles in a Large pH Window with Different Bases. *Materials (Basel)*. **6**, 5549–5567 (2013).
  29. Herrera, A. P., Barrera, C. & Rinaldi, C. Synthesis and functionalization of magnetite nanoparticles with aminopropylsilane and carboxymethyl dextran. *J. Mater. Chem.* **18**, 3650 (2008).
  30. van Ewijk, G. a., Vroege, G. J. & Philipse, a. P. Convenient preparation methods for magnetic colloids. *J. Magn. Magn. Mater.* **201**, 31–33 (1999).
  31. De Palma, R. *et al.* Silane Ligand Exchange to Make Hydrophobic Superparamagnetic Nanoparticles Water-Dispersible. *Chem. Mater.* **19**, 1821–1831 (2007).
  32. Barrera, C., Herrera, A. P. & Rinaldi, C. Colloidal dispersions of monodisperse magnetite

- nanoparticles modified with poly(ethylene glycol). *J. Colloid Interface Sci.* **329**, 107–13 (2009).
33. Natividad, E., Castro, M. & Mediano, A. Accurate measurement of the specific absorption rate using a suitable adiabatic magnetothermal setup. *Appl. Phys. Lett.* **92**, 93116 (2008).
  34. Huang, S., Wang, S.-Y., Gupta, A., Borca-Tasciuc, D. & Salon, S. J. On the measurement technique for specific absorption rate of nanoparticles in an alternating electromagnetic field. *Meas. Sci. Technol.* **23**, 35701 (2012).
  35. Bates, O. K. Thermal Conductivity of Liquid Silicones. *Ind. Eng. Chem.* **41**, 1966–1968 (1949).
  36. R Core Team, R: A language and environment for statistical computing. R Foundation for Statistical Computing. (2014).
  37. Khandhar, A. P., Ferguson, R. M. & Krishnan, K. M. Monodispersed magnetite nanoparticles optimized for magnetic fluid hyperthermia: Implications in biological systems. *J. Appl. Phys.* **109**, 07B310 (2011).
  38. Chantrell, R., Popplewell, J. & Charles, S. Measurements of particle size distribution parameters in ferrofluids. *IEEE Trans. Magn.* **14**, 975–977 (1978).
  39. Gnanaprakash, G. *et al.* Effect of initial pH and temperature of iron salt solutions on formation of magnetite nanoparticles. *Mater. Chem. Phys.* **103**, 168–175 (2007).
  40. Zhao, S. & Asuha, S. One-pot synthesis of magnetite nanopowder and their magnetic properties. *Powder Technol.* **197**, 295–297 (2010).
  41. Morales, M. P. *et al.* Surface and Internal Spin Canting in  $\gamma$ -Fe<sub>2</sub>O<sub>3</sub> Nanoparticles. *Chem. Mater.* **11**, 3058–3064 (1999).

42. Calero-DdelC, V. L. & Rinaldi, C. Synthesis and magnetic characterization of cobalt-substituted ferrite ( $\text{Co}_x\text{Fe}_{3-x}\text{O}_4$ ) nanoparticles. *J. Magn. Magn. Mater.* **314**, 60–67 (2007).
43. del Castillo, V. L. C.-D. & Rinaldi, C. Effect of Sample Concentration on the Determination of the Anisotropy Constant of Magnetic Nanoparticles. *IEEE Trans. Magn.* **46**, 852–859 (2010).
44. Bohorquez, A. C. & Rinaldi, C. In Situ Evaluation of Nanoparticle-Protein Interactions by Dynamic Magnetic Susceptibility Measurements. *Part. Part. Syst. Charact.* **31**, 561–570 (2014).
45. Laurent, S., Dutz, S., Häfeli, U. O. & Mahmoudi, M. Magnetic fluid hyperthermia: focus on superparamagnetic iron oxide nanoparticles. *Adv. Colloid Interface Sci.* **166**, 8–23 (2011).
46. Box, G. E. P., Hunter, J. S. & Hunter, W. G. *Statistics for Experimenters: design, innovation, and discovery*. (John Wiley & Sons, Inc., New York, NY., 2005).
47. Barrera, C., Herrera, A., Zayas, Y. & Rinaldi, C. Surface modification of magnetite nanoparticles for biomedical applications. *J. Magn. Magn. Mater.* **321**, 1397–1399 (2009).
48. Cervadoro, A. *et al.* Design Maps for the Hyperthermic Treatment of Tumors with Superparamagnetic Nanoparticles. *PLoS One* **8**, e57332 (2013).
49. Alvarez-Berríos, M. P., Castillo, A., Rinaldi, C. & Torres-Lugo, M. Magnetic fluid hyperthermia enhances cytotoxicity of bortezomib in sensitive and resistant cancer cell lines. *Int. J. Nanomedicine* **9**, 145–53 (2014).

# Chapter 3

## *In vitro* ultrasonic potentiation of 2-phenylethanesulfonamide/magnetic fluid hyperthermia combination treatments for ovarian cancer

---

### 3.1 Summary

Thermal energy produced by magnetic fluid hyperthermia (MFH) can be delivered either by convective heat transfer of the bulk heating of fluids and tissues surrounding cancer cells, or by the intracellular heating at the nanoscale. The delivered thermal energy triggers a series of subcellular events resulting in cytotoxic effects often leading to cancer cell death, mainly by apoptosis. *In vitro* and *in vivo* studies have demonstrated that, when MFH is used as adjuvant in cancer chemotherapy, the mechanism of action of several chemotherapeutic agents are potentiated<sup>1</sup>. The phenomenon often occurs at mild hyperthermia temperatures (~41°C). This is of particular interest because reaching hyperthermia temperatures (> 43°C) in tumors remains a challenge, as it requires large nanoparticle doses, increasing the risk of toxicity. It is thought that, synergy between chemotherapeutic drugs and the release of thermal energy could still be possible even if temperatures at the hyperthermia range are not achieved. In this sense, thermal potentiation of drugs can also occur via local heating effects produced by nanoparticles internalized into, without the need of bulk macroscopic temperature rise of tumors. A widely used strategy to induce the internalization of nanoparticles and drugs into cancer cells via receptor-mediated endocytosis is the use of targeted nanoparticles, both for MFH and drug delivery applications. Unfortunately, targeted platforms involve complex methods leading to low-efficiency conjugations, and various *in vivo* drawbacks including immunogenicity and susceptibility to nanoparticle lysosomal degradation. As an alternative, FDA-approved low-

intensity focused ultrasound (LIFU) and microbubble contrast agents can be used to induce cell sonoporation. The rationale behind sonoporation is the formation of reversible micropores across the cell membrane, which instantaneously facilitates the cellular uptake of nanoparticles and chemotherapeutic drugs. Therefore, the passive transport of nanoparticles and drug molecules into cancer cells is increased by using external stimuli rather than targeted nanoparticle platforms. This chapter features the work carried out by microbubble-assisted ultrasound to improve the cellular uptake of magnetic nanoparticles and the chemotherapeutic agent 2-phenylethynylsulfonamide (PES). It was hypothesized that ultrasound would potentiate the cell killing profile of PES/MFH combination treatments in ovarian cancer therapy. Results revealed that LIFU is a promising alternative in the treatment of *in vitro* ovarian cancer, potentiating the effects of MFH and PES, both individually and combined.

### **3.2 Introduction and literature review**

The use of heat to improve the effects of chemotherapy has been reported both *in vitro* and *in vivo*, using conventional hyperthermia. For example, enhanced cytotoxicity of cisplatin and bortezomib was reported using hot water hyperthermia (HWH) in mouse leukemia and human breast cancer cells<sup>3,4</sup>. Also, microwave- and radiofrequency-based hyperthermia in combination with cisplatin in dogs and patients from clinical trials, respectively, have led to enhanced potentiation of the drug's therapeutic effect<sup>5,6</sup>. Unfortunately, increased incidence of vomits, skin burns, tissue necrosis, and other side effects limit the use of regional hyperthermia approaches. To alleviate these problems, the use of MFH has emerged as an alternative to induce local hyperthermia, reducing non-specific heating (e.g. healthy tissues), yet enhancing the cytotoxic profiles of chemotherapeutic drugs. Therefore, the potentiation of chemotherapy via local release of thermal energy has been explored by means of various MFH/drug combination treatments<sup>7</sup>.

Most of these studies have demonstrated enhanced cytotoxic profiles with MFH as an adjuvant in chemotherapy when compared to MFH and/or administration of drug, separately. A detailed review of MFH/drug combined systems along with relevant findings was reported by Torres-Lugo and Rinaldi, highlighting opportunities and challenges<sup>2</sup>.

The interest in evaluating additional MFH/drug combination treatments has increased, with a growing number of *in vitro* and *in vivo* studies using various drugs and cancer models. Among the *in vitro* studies, synergistic effects between drug and MFH have been reported along with chemosensitization of cancer cells with heat. For example, Lee *et al.* reported enhanced cytotoxic effects in colon cancer cells with MFH/cisplatin combined treatments, using a lower cisplatin concentration compared to that used in experiments with drug in the absence of MFH<sup>8</sup>. Alvarez-Berrios *et al.* reported the hyperthermic potentiation of cisplatin and bortezomib using carboxymethyl-dextran-coated magnetic nanoparticles. Notably, the co-administration of MFH and bortezomib induced sensitivity in resistant cancer cells thus demonstrating that chemosensitivity can be induced via MFH<sup>9,10</sup>. Other chemotherapeutic agents have been also studied in combination with MFH to evaluate thermal potentiation profiles. For example, Eynali *et al.* reported enhanced cytotoxic effects on colon cancer cells, using 5-fluorouracil (5-FU) embedded on PLGA-coated iron oxide nanoparticles, leading to chemosensitization of resistant cancer cells<sup>11</sup>. Qu *et al.* reported synergistic profiles on MFH/ Camptothecin (CPT) combined treatments in ovarian and hepatic cancer cells, using PLA-coated iron oxide nanoparticles loaded with CPT. The authors highlighted the enhanced cellular uptake due to efficient MFH and up-regulation of heat shock proteins (HSP70) expression<sup>1</sup>. When evaluated *in vivo*, some of the drugs discussed before have shown to be synergistically improved by MFH. For example, Yang *et al.* demonstrated that cisplatin-loaded, PGLA-coated magnetic nanoparticles synergistically

improved the antitumor effect in hepatic tumor-bearing rabbits, leading to coagulative necrosis and hyperthermic ablation of tumors<sup>12</sup>. Other drugs such as doxorubicin have led to significant tumor volume reductions in mice bearing human hepatoma tumors when the drug has been loaded in magnetic nanocarriers. The effects of MFH/doxorubicin were significantly better compared to free drug treatments<sup>13</sup>. Recently, Court *et al.* performed a gene expression study identifying target genes that, when inhibited, could enhance the toxicity of certain drugs, such as the HSP70 inhibitor 2-phenylethanesulfonamide (PES), both *in vitro* and *in vivo*. The combined MFH/PES treatment was synergistic, leading to significantly higher ovarian cancer cell death when compared to MFH or PES individual treatments at temperatures of 41 and 43°C. In addition, significant tumor volume reductions were observed after MFH/PES administration in mice bearing intraperitoneal ovarian tumors, indicating a successful and synergistic profile between PES and MFH, and excellent agreement between the *in vitro* and the *in vivo* observations<sup>14</sup>.

One of the limitations for the clinical translation of MFH is the required hyperthermia temperatures, which are difficult to attain *in vivo*. This is a consequence of impaired nanoparticle accumulation in tumors and subsequent low internalization into cancer cells after intravenous (IV) nanoparticle administration<sup>15</sup>. Hence, additional efforts must be done to improve the cellular uptake of nanoparticles aiming to release the thermal energy intracellularly. Despite the theoretical arguments against nanoscale thermal phenomena, experimental evidence of localized heating effects has been highlighted, emphasizing biologically relevant responses<sup>16</sup>. For example, Creixell *et al.* demonstrated that exceptional killing profile of breast cancer cells without any macroscopic temperature rise of the bulk medium can be achieved, using iron oxide nanoparticles targeted for epidermal growth factor receptor (EGFR)<sup>17,18</sup>. Domenech *et al.*

supported those findings, suggesting that lysosomal membrane permeabilization is one of the mechanism leading to cell death due to local heating effects when using nanoparticles targeted for EGFR<sup>19</sup>. The intracellular magnetic release of drugs without temperature changes in bulk media also support the evidence of local heating effects. Despite the benefits of targeted platforms to improve drug and nanoparticle internalization into cells, some drawbacks including accelerated blood clearance, impaired tumor penetration and lysosomal digestion of cargo drugs have been reported<sup>20</sup>. In fact, nanoparticle biodistribution is not influenced by targeting ligands and they are still dependent on the enhanced permeability and retention (EPR) effect. In other words, high specificity for cancer cells is provided but nanoparticles still have to extravasate into the leaky vasculature of tumors, just as non-targeted nanoparticles do<sup>21</sup>. Physical methods rather than chemical conjugations have been proposed for the transient, structural alteration of endothelial barriers and cell membranes<sup>22</sup>. The aim of these methods is facilitating extravasation of particles and drug molecules to tumors and their subsequent internalization into tumor cells. FDA-approved therapeutic ultrasound used simultaneously with microbubble contrast agents has been suggested to promote cell sonoporation, aiming to increase the cellular uptake of drugs and nanoparticles<sup>23</sup>. Effects of cell sonoporation have been previously studied, indicating that structural alteration of cell membranes is strongly dependent on cell type and ultrasound experimental conditions. For example, Yudina *et al.* reported cell membrane permeabilization effects for up to 24 hours in C6 rat glioma cells, using fluorescence microscopy. Half-lives of approximately 8 hours were reported for fluorescent dyes and US-induced permeability was found to slowly decrease with time<sup>24</sup>. Spectroscopic techniques have been also used to demonstrate the alteration of cell membrane after sonoporation, demonstrating that sonoporation is a reversible process, minimally affecting cell viability<sup>25</sup>.

There is an increased interest in using sonoporation to enhance the intracellular delivery of chemotherapeutic drugs, aiming to boost their mechanisms of action for improved efficacy in anti-cancer therapies. Some *in vitro* studies are summarized in Table 3.1 highlighting drug/microbubble platforms, ultrasound parameters and relevant findings. In addition to the physical effects of the cell membrane, cavitation produced by microbubble-assisted LIFU can be used to stimulate endothelial walls thus increasing drug extravasation for increased drug accumulation in tumors<sup>26</sup>. Some mechanisms associated to ultrasound-enhanced drug extravasation include stimulation of paracellular and transcellular pathways, especially disruption of tight junctions and transcytosis, the latter hypothesized to occur as a consequence of transient vasoconstriction<sup>27,28</sup>. Improved extravasation is also required for nanoparticles injected via IV given the low extravasation profiles often exhibited, which contributes to their poor accumulation in tumors<sup>29</sup>. An additional challenge for efficient drug uptake by cancer cells is the chemical composition of the drug molecule, especially for hydrophilic molecules with unpredictable active uptake pathways<sup>30</sup>. Microbubble-assisted ultrasound can circumvent these issues because, as demonstrated by Juffermans *et al.*, reporting local hyperpolarization of the cell membrane, leading to the formation of transient hydrophilic pores thus facilitating the passage of hydrophilic drugs<sup>31</sup>. The performance of various microbubble-assisted ultrasound chemotherapy systems have been evaluated both *in vitro* and *in vivo*, along with a growing number of preclinical experiments, as compiled by Lammertink *et al.*<sup>22</sup>. Overall, increased intracellular drug concentrations leading to improved cancer cell killing profiles have been achieved with sonoporation. Drugs like doxorubicin and paclitaxel loaded on lipid- and alginate-based microbubbles, using continuous ultrasound have shown to provide enhanced cytotoxicity in ovarian cancer cells when compared to drug internalization without sonoporation<sup>32,33</sup>. Other

studies report the use of drug and microbubbles, separately, using commercial microbubble contrast agents along with pulsed ultrasound. Similarly to drug-loaded microbubbles, increased cancer cell death patterns have been described when compared to non-US conditions for drugs like paclitaxel, cisplatin, doxorubicin and cetuximab<sup>34-36</sup>. Similar improvements have also been observed *in vivo*, revealing significant tumor volume reductions, decreased accumulation of drugs in the liver and prolonged median survival of animal models, compared to ultrasound-free chemotherapy<sup>22</sup>.

**Table 3.1.** Literature review on *in vitro* sonoporation-assisted internalization chemotherapeutic drugs.

Author	Microbubble (MB)/ drug	Cell lines	Ultrasound (US) parameters	Results (compared to non-US)
Baghbani <i>et al.</i> <sup>32</sup>	Doxorubicin-loaded, alginate PHF	A2780 ovarian carcinoma	<ul style="list-style-type: none"> <li>• Continuous US</li> <li>• <math>I = 2 \text{ W/cm}^2</math></li> <li>• <math>f = \text{Up to } 1 \text{ MHz}</math></li> <li>• <math>t_{\text{US}} = \text{N/A}</math></li> </ul>	Drug release was higher at low frequency. No comparison to free drug or non-US conditions
Sun <i>et al.</i> <sup>33</sup>	Paclitaxel-loaded, lipid MB	SKOV3 ovarian carcinoma	<ul style="list-style-type: none"> <li>• Continuous US</li> <li>• <math>I = 0.5 \text{ W/cm}^2</math></li> <li>• <math>t_{\text{US}} = 15 \text{ s}</math></li> </ul>	Increased cell death with US-assisted drug-loaded and enhanced drug uptake.
Escoffre <i>et al.</i> <sup>34</sup>	Doxorubicin / SonoVue, Vevo, Polylactide shelled (PlyS), PlyS-PEG	U-87 MG, MDA-MB-231 glioblastoma and breast carcinoma	<ul style="list-style-type: none"> <li>• PRP – 100 <math>\mu\text{s}</math></li> <li>• <math>t_{\text{US}} = 30 \text{ s}</math></li> <li>• <math>P = 0.4 - 0.8 \text{ MPa}</math></li> <li>• DC 40%</li> </ul>	Increased cell death with US-assisted drug uptake. PlyS and Vevo MB showed higher performance than commercial MB.
Sorace <i>et al.</i> <sup>35</sup>	Definity / Paclitaxel	2LMP breast - lung metastatic pooled cells	<ul style="list-style-type: none"> <li>• <math>P = 1 \text{ MPa PNP}</math></li> <li>• DC = 20%</li> <li>• <math>t_{\text{US}} = 5 \text{ min}</math></li> </ul>	US-assisted drug uptake led to 50% more cancer cell death.
Heath <i>et al.</i> <sup>36</sup>	Definity/ Cisplatin and Cetuximab	SCC-1, SCC-5, Cal27, FaDu head and neck cancer cells	<ul style="list-style-type: none"> <li>• <math>MI = 0.5</math></li> <li>• PRP = 10 MS</li> <li>• DC = 20%</li> <li>• <math>t_{\text{US}} = 5 \text{ min}</math></li> </ul>	28% more cetuximab and 9% more cisplatin uptake with US-assisted therapy.

The use of LIFU to increase the uptake of magnetic nanoparticles has been reported for various applications in the biomedical field. The studies are summarized in Table 3.2 highlighting nanoparticle platforms, ultrasound parameters and relevant findings. For example, Kolarova *et al.* showed that one-minute sonoporation led to iron uptake of approximately 8.3  $\mu\text{g}/\text{cell}$  when compared to 6.76  $\mu\text{g}/\text{cell}$  achieved with 24-hour standard incubation without ultrasound. Even when improvements on iron uptake were not statistically significant, this study demonstrated that sonoporation has an immediate effect compared with non-specific uptake at long incubation times<sup>37</sup>. Other studies involved the use of LIFU to investigate mechanisms associated with internalization of nanoparticles through cell pores. For example, Yang *et al.* reported that sonoporation led to non-internalizing uptake routes, reducing the oxidative stress thus minimizing long-term cytotoxicity of nanoparticles in healthy cells.<sup>38</sup> Additionally, the potential of using nanoparticles embedded in ultrasound microbubbles has been studied, as reported by Yang *et al.* using liver cancer cells. The study reported that ultrasound led to higher nanoparticle uptake by cells when compared to sonoporation using nanoparticles and microbubbles, separately<sup>39</sup>. Perhaps of higher relevance, the use of LIFU to increase the cellular uptake of magnetic nanoparticles has been suggested for imaging applications, especially those of magnetic resonance imaging (MRI). Also, improved nanoparticle uptake patterns are useful for tumor cell labeling during cancer migration studies and other diagnostic applications. For example, Cheng *et al.* reported enhanced localization of antineoplastic drugs via MRI of brain tumors, by using LIFU and magnetic nanoparticles<sup>40</sup>. Similarly, Xiang *et al.* reported enhanced nanoparticle internalization into human osteosarcoma cells after LIFU at various exposure times. MRI of cell pellets showed significant enhancements for cells with increased nanoparticle uptake after ultrasound exposure, with iron quantification via Prussian Blue staining<sup>41</sup>. The optimization

of ultrasound experimental conditions is critical to ensure that cell membranes are reversibly permeabilized/porated yet causing minimal damage to cell viability. This balance is achieved by tuning the ultrasound experimental conditions, including acoustic intensity, exposure time and type of pulse. For example, Mo *et al.* investigated the use of LIFU with magnetic nanoparticles for magnetic labelling of mouse hepatoma cells. It was found that labelling efficiency increased as a function of intracellular nanoparticle concentrations, which was strongly influenced by acoustic pressure and exposure time.

**Table 3.2.** Literature review on sonoporation-assisted internalization of magnetic nanoparticles.

Author	Nanoparticle system	Cell lines / Animal model	Ultrasound parameters	Results
Kolarova <i>et al.</i> <sup>37</sup>	Iron oxide – Poly(acrylic-co-maleic) acid-coated	Fibroblasts	<ul style="list-style-type: none"> <li>• Continuous US</li> <li>• I = 0.1 W/cm<sup>2</sup></li> <li>• t<sub>US</sub> = 60 s</li> <li>•</li> </ul>	Enhanced MNP uptake 1-minute post sonications.
Yang <i>et al.</i> <sup>38</sup>	Iron oxide – APTS coated	HepG2 human carcinoma	<ul style="list-style-type: none"> <li>• PVA MB</li> <li>• P = 0.25 MPa</li> <li>• PRP = 10 ms</li> </ul>	Low levels of ROS for MB-mediated sonoporation
Yang <i>et al.</i> <sup>39</sup>	Iron oxide embedded in PVA	SMMC-7721 human liver carcinoma	<ul style="list-style-type: none"> <li>• I = Up to 0.75 W/cm<sup>2</sup></li> <li>• PRP = 1 ms</li> <li>• t<sub>US</sub> = 40 s</li> </ul>	Improved nanoparticle uptake when embedded in microbubbles
Chen <i>et al.</i> <sup>40</sup>	Iron oxide – Nitrosourea loaded	C6 rat glioma	<ul style="list-style-type: none"> <li>• Sonovue MB</li> <li>• P = 0.7 MPa</li> <li>• PRP = 10 ms</li> <li>• t<sub>US</sub> = 30 s</li> </ul>	Enhanced localization of drug-loaded nanoparticles via MRI.
Xiang <i>et al.</i> <sup>41</sup>	Iron oxide – Silica coated	Osteosarcoma	<ul style="list-style-type: none"> <li>• I = 30 mW/cm<sup>2</sup></li> <li>• PRP = 1 ms</li> <li>• DC = 40%</li> </ul>	Increased MNP uptake in exposure-duration-dependent manner
Mo <i>et al.</i> <sup>42</sup>	Iron oxide – Dextran coated	H-22 mouse hepatoma	<ul style="list-style-type: none"> <li>• Continuous US</li> <li>• t<sub>US</sub> = 60 s</li> <li>• Power: 2 W</li> </ul>	Increased MNP uptake for magnetic labelling

Undoubtedly, sonoporation is a useful technique to improve the cytotoxicity of chemotherapeutic agents and to enhance magnetic particle imaging. However, the potential of LIFU for MFH applications has not been reported at the moment this document was written. Therefore, motivated by the need to improve the effects of MFH and MFH/drug combined treatments, this work features the use of microbubble-assisted LIFU to induce sonoporation in ovarian cancer cells. The overall goal is to improve the cellular uptake of PEG-coated nanoparticles and the HSP70 inhibitor, PES. It was hypothesized that ultrasound exposure of cells in the presence of nanoparticles and PES would increase their intracellular concentrations thus leading to superior cancer cell killing profile after exposure to AMF. To test our hypothesis, a systematic experimental design was proposed, evaluating the three individual therapies: ultrasound (US), hyperthermia (MFH), and drug (PES). Subsequently, these three individual therapies were combined in dual treatments, to finally have the triple US/PES/MFH group as the subject of our hypothesis. It was found when ultrasound was incorporated, for example US+PES and US+MFH groups, cell viability decreased when compared to PES alone or MFH alone. As expected, notable reductions in cell viability were observed for the US+PES+MFH group, with improved cell killing profile when compared to PES+MFH which has been previously reported as synergistic when compared to PES alone and MFH alone, respectively. Increased lysosomal disruption caused by elevated intracellular concentrations, attained via sonoporation and potentiated by MFH was proposed as one of the cell death pathways. Hence, it is expected microbubble-assisted ultrasound becomes an innovative, non-invasive actuator to enhance the effects of MFH, with potential to develop a sono-thermo-chemotherapy in the treatment of ovarian cancer.

### **3.3 Experimental section**

#### **3.3.1 Materials**

RPMI 1640 culture medium, sodium bicarbonate, gentamicin solution, phosphate buffered saline (PBS), Trypan Blue, Trypsin-EDTA 0.25%, hydroxylamine hydrochloride, sodium acetate, 1,10-phenanthroline monohydrate, ICP iron standard, EDTA 5Mm solution, and 2-phenylethanesulfonamide (PES) were purchased from Sigma Aldrich (St. Louis, MO). Nitric acid 70% v/v (Optima grade) and ethanol absolute were purchased from Fisher Scientific (Hampton, New Hampshire). Fetal bovine serum (FBS), Sytox Green nucleic acid stain, Hoechst® 3342, DiD Vibrant cell-labeling solution, and Hanks balanced salt solution (HBSS) were purchased from Life Technologies/Thermo Fisher Scientific (Waltham, MA). Calcein-AM and acridine orange/propidium iodide staining kits were purchased from Nexcelom Biosciences (Lawrence, Massachusetts). CellTiter Blue® cell viability assay was purchased from Promega Corporation (Madison, Wisconsin). EZ4U cell proliferation assay was purchased from Biomedica Immunoassays (Salem, New Hampshire). Definity® microbubbles were donated by Lantheus Medical Imaging (North Billerica, MA). Iron oxide magnetic nanoparticles were synthesized and coated with poly ethylene glycol, as described in Chapter 2 of this dissertation. PEG-coated nanoparticles conjugated with Alexa Fluor 488® were donated by Dr. Carlos Rinaldi from department of Biomedical Engineering, University of Florida. All reagents were used as received or as indicated by the manufacturer.

#### **3.3.2 Cell cultures**

A2780 ip-1, Hey A8 ip1 and SKOV3 sc2 human ovarian carcinoma cells were provided by Dr. Edna Mora from the Comprehensive Cancer Center of Puerto Rico. Cells were cultured on

75 cm<sup>2</sup> flasks (Eppendorf, Hamburg, Germany) with Roswell Park Memorial Institute (RPMI) 1640 medium supplemented with 15% FBS, 2 g/L sodium bicarbonate, 0.1% gentamicin and maintained at 37°C and 5% CO<sub>2</sub> as described elsewhere<sup>14</sup>. Cells were split every three days at 1:3 split ratio with an 80-90% of confluence, keeping passage numbers below twenty.

### **3.3.3 Cytotoxicity of PEG-coated nanoparticles and Definity® microbubbles**

Cytotoxic effects of PEG-coated nanoparticles and Definity® ultrasound contrast agents, were studied in the three ovarian cancer cell lines, according to the following experimental protocols.

#### **3.3.3.1 Nanoparticle cytotoxicity**

Five-thousand cells were seeded in 96-well plates (Costar, Corning, NY) and incubated at 37°C and 5% CO<sub>2</sub> for 18 hours. PEG-coated nanoparticles suspended in RPMI 1640 and supplemented with 15% FBS were added to cells (200µL/well) at different iron oxide concentrations [0.12 – 4.00 mg/mL]. Cells were incubated at 37°C and 5% CO<sub>2</sub> for up to 48 hours, washed twice with PBS and incubated for twenty-four additional hours with RPMI/FBS medium. Cells were washed with PBS and then cell viability was determined using the CellTiter Blue® viability assay, following the manufacturer instructions along with a fluorescence microplate reader (SpectraMax Gemini EM, Molecular Devices, San Jose, CA). Three independent experiments for each cell line were carried out, with each experiment having n = 6.

#### **3.3.3.2 Definity® microbubbles cytotoxicity**

Definity® microbubbles were activated for 45 seconds, following the manufacturer instructions. Microbubble liquid suspensions in RPMI/FBS were prepared from dilutions of the

original stock with concentrations ranging 0.06 -  $4.00 \times 10^8$  microbubbles/mL (MB/mL). Two-milliliter of each concentration were added to 35 mm culture dishes (Eppendorf, Hamburg, Germany), seeded with  $2.75 \times 10^5$  cells 18 hours before the experiment. Petri dishes were incubated at 37°C and 5% CO<sub>2</sub> for up to 48 hours. Cells were washed with PBS, trypsinized and counted with an automated cell counter (Auto T4, Nexcelom Biosciences, Boston, MA) using Trypan Blue live/dead cell exclusion. Experiments were performed in triplicate.

### **3.3.4 Nanoparticle internalization in ovarian cancer cells**

#### **3.3.4.1 UV/Vis iron quantification**

One million cells were seeded in 6-well plates (Eppendorf, Germany) 18 hours prior to the experiment. Two milliliters of PEG-coated nanoparticle suspensions at iron oxide concentration of 0.6 mg/mL in RPMI/FBS 15% were added to each well and then, cells were incubated at 37°C and 5% CO<sub>2</sub> for different exposure times (i.e. 3, 6, 12 hours). Cells were washed twice with PBS, rinsed with EDTA 5 mM, incubated for 20 minutes, and detached using vigorous pipetting. Suspended cells were collected in conical tubes and an aliquot of 40 µL of cell suspension was taken for cell counts, using an automated cell counter and Trypan Blue live/dead cell exclusion. The remaining cell suspensions were centrifuged at 3,300 rpm for 8 minutes. After supernatant removal, nitric acid 70% was added to cell pellets using a proportion of one-mL of nitric acid per million-cell. Cells were digested in a dry heat block (Isotemp 2001, Fisher Scientific, Hampton, New Hampshire) at 101°C overnight until complete acid evaporation and then, UV-iron quantification was performed as described in Chapter 2 using a UV/Vis absorbance microplate reader (Infinite M200 PRO, Tecan, Männedorf, Switzerland). All experiments were performed in triplicate.

### **3.3.4.2 Confocal microscopy**

Seventy-five thousand cells were seeded in 2-well glass chamber slides (Model 155380, Thermo Scientific, Waltham, MA) twenty-four hours prior to the experiment. One milliliter of PEG-coated nanoparticle suspension with or without fluorescent nanoparticles (iron oxide concentrations of 0.2 mg/mL) in RPMI/FBS 15%, was added to each chamber and incubated for 1.5 hours at 37°C and 5% CO<sub>2</sub>. The nuclear and membrane dyes Hoechst 33342 (10 µg/mL) and DiD (5 µg/mL) were added to each chamber and incubated for an additional 30 minutes, and further washed with PBS. Once the exposure time finished, pictures of the slide chambers were captured with an Olympus Spinning Disk (3i system, Denver, CO) confocal microscope (Olympus IX81, Denver, CO) equipped with a Xenon fluorescence source for visualization. Images were obtained using a 60X objective and Rolera EM-C2 camera (Quantitative Imaging Corporation). The red, green and blue filters allowed to visualize cell membrane, nanoparticles and nuclei, respectively. Experiments were performed in duplicated.

### **3.3.5 Focused ultrasound design and calibration**

A single-element focused ultrasound transducer (model H-115) was purchased from Sonic Concepts® (Bothell, WA), consisting of a single-element spherical piezoelectric crystal. A coupling, truncated cone was placed onto the transducer and filled with degassed, deionized water to avoid ultrasound attenuation and bubble cavitation between the concave plate and the target region (the tip of the truncated cone). A truncated conical design with a circular top surface of 35 mm internal diameter, defined as the target region, was chosen in order to hold petri dishes of the same diameter to directly sonicate cell monolayers adhered to dishes. Hence, the target region rises 40 mm above the concave region of the transducer, along the focal distance.

The transducer-cone assembly was characterized using a HNR-100 needle hydrophone (Onda Corp, Sunnyvale, CA) to experimentally determine the position on the circular target region at which the ultrasound intensity is maximum. The experimental setup for the calibration is very similar to that reported by Rodríguez-Negrón<sup>43</sup> with slight modifications. Briefly, the transducer/cone assembly was filled with degassed water and sealed with a latex membrane at the target region and placed at the bottom of a container filled with tap water. A manual micro-manipulator was used to place the hydrophone at the target region and connected to a digital oscilloscope (Agilent Technologies, Santa Clara, CA). Short sinusoidal pulses were delivered by an arbitrary waveform generator, connected to an E&I® 100W RF power amplifier (Rochester, NY), which was subsequently connected to an impedance matching network before reaching the transducer. Pressure measurements were performed along circular target region and also in the vertical axis, starting at 40 mm from the transducer up to 60 mm. All measurements were performed at steps of 1 mm, at a fixed amplitude of 1 V and center frequency of 1.1 MHz. Acoustic intensity values were obtained from the pressure values, using equation 3.1:

$$I = \frac{P^2}{2 * Z * (100)^2} \quad (3.1)$$

where  $P$  is the peak pressure,  $Z$  is the acoustic impedance of water ( $1.48 \text{ kg/s} \cdot \text{m}^2$ ), and  $100^2$  is the correction factor required to express the acoustic intensity in  $\text{W/cm}^2$ . When using pulsed ultrasound, the acoustic intensity varies with time thus it is reported as the spatial peak temporal average intensity,  $I_{\text{SPTA}}$ , which is obtained when equation 3.1 is multiplied by the duty cycle. The acoustic intensity mapping of the transducer at the target region is shown in Figures A.1 and A.2 (Appendix).

### **3.3.6 Optimization of ultrasound parameters for cell sonoporation**

#### **3.3.6.1 Effect of continuous/pulsed ultrasound, intensity and ultrasound exposure time**

HeyA8 cells ( $1.5 - 2.0 \times 10^6$  cells) were seeded in 35 mm petri dishes 18 hours before experiments. Definity® microbubbles suspended in RPMI/FBS 15% at concentrations between  $1.0 - 2.5 \times 10^7$  MB/mL (13 – 33 MB/cell) were added to cells. The ultrasound transducer was filled with deionized, degassed water and sealed with a latex membrane to which, a thin layer of ultrasound coupling gel was applied right before each sonication. Petri dishes were placed on top of the transducer and exposed to ultrasound, either continuous or pulsed for times ranging in 30 – 60 seconds, at intensities ranging from 2 to 5 W/cm<sup>2</sup>. For pulsed ultrasound, the pulsed repetition period (PRP) and duty cycle (DC) were fixed to 1.0 ms and 30%. Once sonicated, petri dishes were incubated for 30 minutes at 37°C and 5% CO<sub>2</sub>, detached with trypsin and counted with an automated cell counter (Auto T4, Nexcelom Bioscience, Lawrence, MA) using Trypan Blue live/dead cell exclusion. Results were processed as viability ratio with respect of control groups without ultrasound exposure. Experiments were performed in triplicate.

#### **3.3.6.2 Effect of cell numbers at various intensity values**

The experimental procedure was similar to that described in the previous section, with some differences to account for the variables to be studied. Three groups with different cell numbers ( $1 \times 10^5$ ,  $5 \times 10^5$  and  $1 \times 10^6$  cells) were used at intensity values ranging from 3.0 to 16.3 W/cm<sup>2</sup> (I<sub>SPTA</sub> 0.9 – 4.9 W/cm<sup>2</sup>). The ultrasound exposure time and microbubble-to-cell ratio were fixed to 30 s and 66 MB/cell. After ultrasound exposure, cells were incubated, detached and counted as described in the previous section. Experiments were performed in triplicate.

### 3.3.7 Assessment of cell membrane permeabilization

Five hundred thousand HeyA8 cells were seeded in 35 mm petri dishes 18 hours before the experiments. A cocktail of 2  $\mu$ M SYTOX Green®, Hoechst 33342 (10 mg/mL) and Definity® microbubbles (66 MB/cell) was added to petri dishes, followed by exposure to pulsed ultrasound (PRP = 1.0 ms, DC = 30%) in the dark. Four separate groups were studied varying the intensity ( $I$ ) and the ultrasound exposure time ( $t_{us}$ ), according to the experimental design shown in Table 3.3. After ultrasound exposure, cells were incubated at 37°C and 37% CO<sub>2</sub> for 30 minutes in the dark, washed with HBSS four times, and subsequently imaged using an inverted fluorescence microscope (CKX53, Olympus, Tokyo, Japan). Pictures were taken using a 20X objective and cooled, color camera (DP74 CMOS, Olympus, Tokyo, Japan). Images were processed using CellSens standard imaging software version 1.14 (CellSens, Zuid-Holland, Netherlands) showing all cells in blue and viable cells with permeabilized cell membranes as green fluorescent cells. Experiments were performed in duplicated.

**Table 3.3.** Experimental design for assessment of cell membrane permeabilization  
Response variable: green fluorescence intensity

<b>Factor</b>	<b>Low level</b>	<b>High level</b>
Intensity (W/cm <sup>2</sup> )	6.0	8.5
I <sub>SPTA</sub> (W/cm <sup>2</sup> )	1.8	2.5
US exposure time (s)	20	40

### **3.3.8 Ultrasound-assisted nanoparticle internalization**

One million cells were seeded in 35 mm petri dishes 24 hours prior to the experiments. The number of cells was chosen to account for the limit of quantification, as reported elsewhere<sup>44</sup>. Definity® microbubbles (66 MB/cell) were suspended in a PEG-coated nanoparticle suspension at iron oxide concentration of 0.6 mg/mL in RPMI/FBS 15% and added to petri dishes. Cells were sonicated at different intensities and ultrasound exposure times (see Table 3.2) and incubated for 5 and 12 hours at 37°C and 5% CO<sub>2</sub>. Cells were washed twice with RPMI/FBS 15%, rinsed with EDTA 5 mM, incubated for 20 minutes, and detached using vigorous pipetting. Detached cells were treated as described in section 3.3.4.2, yielding iron uptake values normalized by the total cell counts. Experiments were run in triplicate.

### **3.3.9 *In vitro* MFH and combined ultrasound-drug-MFH experiments**

#### **3.3.9.1 PES dose-response curve**

Seven-thousand cells were seeded in 96-well plates 18 hours prior to the experiment. PES solutions with concentration ranging from 0 – 50 µM were prepared in RPMI 1640 and supplemented with 15% FBS. Two-hundred microliters of each drug concentration stock were added to plates and incubated at 37°C and 5% CO<sub>2</sub> for up to 72 hours. Cells were washed twice with PBS and then, cell viability was determined using the EZ4U cell proliferation assay, following the manufacturer instructions along with a UV/Vis microplate reader (Infinite M200 PRO, Tecan, Männedorf, Switzerland). Experiments were performed in triplicate.

### 3.3.9.2 US/PES/MFH experiments

Five hundred thousand cells were seeded in 35 mm petri dishes 24 hours before the experiment. Nanoparticles, Definity® microbubbles and/or PES at concentrations 0.6 mg iron oxide/mL, 66 MB/cell and 10  $\mu$ M, respectively, were added to cells. Various experimental groups were created based on the individual treatments (PES, MFH and ultrasound) and their combinations, according to the experimental design shown in Figure 3.1. Sonications were performed using pulsed ultrasound (PRP = 1.0 ms,  $t_{US}$  = 60 s, DC = 30%,  $I_{SPTA}$  = 1.8 W/cm<sup>2</sup>), based on the optimization of ultrasound experimental conditions. Petri dishes were gently rotated along the diameter of the target region during ultrasound exposure. Cells were incubated either for 0.5 or 12 hours at 37°C and 5% CO<sub>2</sub> and then, exposed to an alternating magnetic field using an induction heater (EasyHeat 8310 LI, Ambrell, Scottsville, NY). Petri dishes were positioned at the midpoint of a six-loop coil (2.5” diameter x 2” length) cooled by tap water at 14°C. Fiber optic temperature probes (model 5TC-TT-T-40-72, Omega, Stamford, CT) were used to record the temperatures of liquid media inside petri dishes, the coil, and the surrounding temperature which was set to be 37°C. For this purpose, a hot plate (Isotemp, Fisher Scientific, Waltham, MA) paced inside a plexiglass incubator equipped with a fan to enable air circulation at 37°C. Magnetic exposure was performed for 30 minutes at magnetic  $f$  = 245 kHz and field intensity  $H_o$  = 13 – 15 kA/m to achieve sustained temperatures of 41 or 43°C. Once the magnetic exposure finished, cells were washed with RPMI/FBS 15% to remove nanoparticles, drug and microbubbles, and then fresh culture medium and/or drug were added, followed by incubation for 48 hours at 37°C and 5% CO<sub>2</sub>. Cells were washed, detached with trypsin and counted using two methods: a) manual cell count with Trypan Blue live/dead exclusion, and b) automatic, fluorescent cell count (Vision, Nexcelom Bioscience, Lawrence, MA) using Calcein-AM dye to

identify cells metabolically emitting green fluorescence (see Appendix, Figure A.3). Cell viability ratio were determined with respect of the control (cells without any treatment). All experiments were run in triplicate.

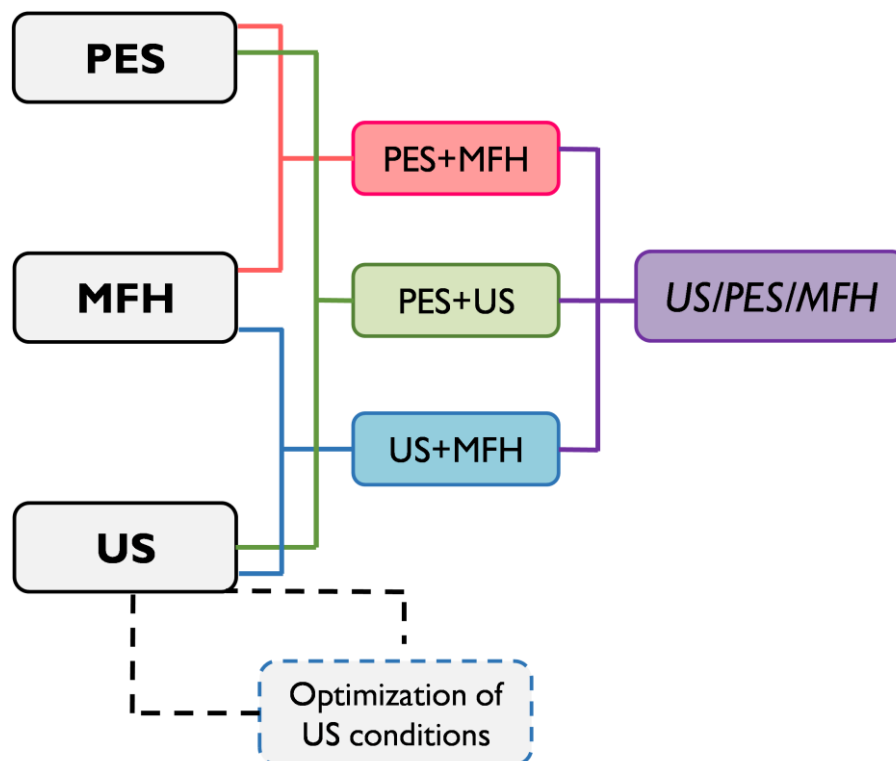


**Figure 3.1.** Overview of experimental design for combined ultrasound-drug-magnetic fluid hyperthermia experiments. Acronyms are defined as follows: 2-phenylethanesulfonamide (PES), magnetic fluid hyperthermia (MFH) and ultrasound (US). Response variable is cell viability.

### 3.4 Results and discussion

This section features results and discussion of *in vitro* experiments aiming to evaluate the response of ovarian cancer cell lines to three therapeutic platforms: MFH, microbubble-mediated

ultrasound and the drug 2-phenylethanesulfonamide. Results include cytotoxicity assessments, optimization of ultrasound conditions, nanoparticle internalization, and magnetic hyperthermia combined with ultrasound and PES.

### **3.4.1 Cytotoxicity of PEG-coated nanoparticles and Definity® microbubbles**

The biocompatibility of PEG-coated nanoparticles (MNP) and Definity® microbubbles (MB) was assessed in A2780, HeyA8 and SKOV3 ovarian cancer cell lines for 48 hours. Results are shown in Figure 3.2 with MNP and MB concentrations expressed in milligrams of iron oxide per milliliter and number of microbubbles per milliliter, respectively. It was found that cell viability remained nearly unaffected in most of the studied concentration range, for both MNP and MB. In the case of MNP, concentrations above 2 mg/mL led to reductions of more than 50% of cell populations (inhibitory concentration, IC<sub>50</sub>), and higher iron oxide concentrations impacted cell viability, as shown in Figure 3.2a. Cytotoxic effects occurred in a cell-dependent fashion, with SKOV3 cells being less affected to high iron oxide concentrations when compared to HeyA8 cells. Iron oxide concentrations below 1 mg/mL are practically non-toxic for cells, thus indicating a safe concentration range for further experiments. One possible cause for the observed cytotoxicity at high nanoparticle concentrations could be hypertonic effects caused by PEG grafted on the surface of nanoparticles, which becomes higher as nanoparticle concentration increases. For example, Choi *et al.* reported that hypertonic environments induce the activation of cell death pathways, including lysosomal rupture and release of cathepsin B to the cytosol, causing cell death<sup>45</sup>. In addition, it is possible that nanoparticle stability in culture medium decreases at high nanoparticle concentrations, leading formation of particle aggregates thus affecting cell viability. In the case of Definity® microbubbles, an overall good biocompatibility at concentrations below 1x10<sup>8</sup> MB/mL was observed, as shown in Figure 3.2b. Higher MB

concentrations led to reductions in cell viability, though the  $IC_{50}$  was not observed even at the maximum studied concentration,  $4 \times 10^8$  MB/mL. Perflutren-containing Definity® microbubbles are coated with various lipid shells, along with PEG chains, molecular weight 5kDa. Therefore, hypertonicity caused by lipid and polymeric shells grafted on MB at higher concentrations may have caused reductions in cell viability. In addition, it has been reported that the stability of Definity® microbubbles is affected by temperature<sup>46</sup>. Therefore, the 48-hour incubation at 37°C could have induced microbubble dissolution, increasing the free lipid and perflutren concentrations in culture media thus aggravating hypertonic effects. Based on results of the present cytotoxic assessment and unless otherwise stated, iron oxide concentration of 0.6 mg/mL and MB concentration ranging in  $1.0 - 3.0 \times 10^8$  MB/mL were chosen for subsequent experiments.

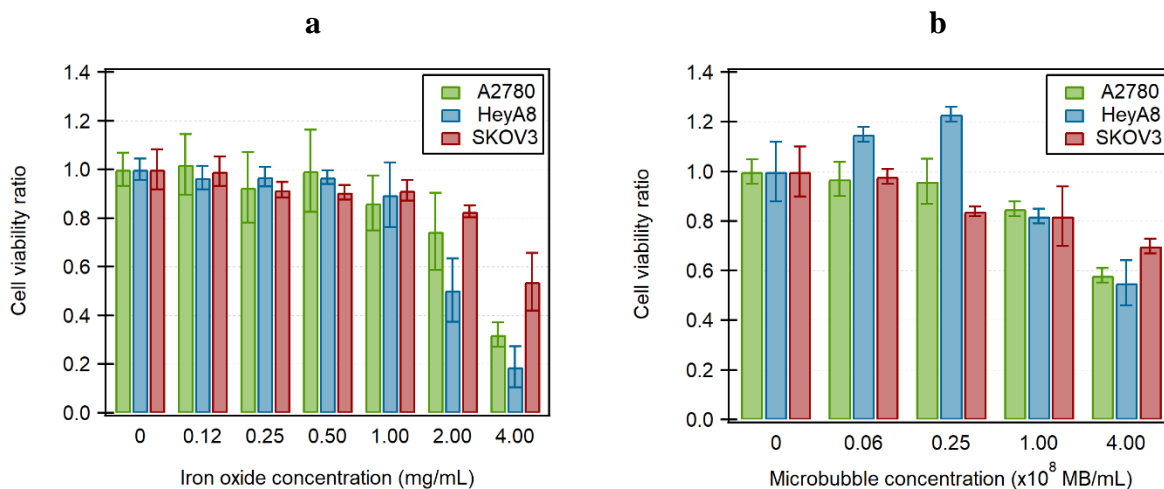


**Figure 3.2.** Cytotoxicity assessments in three ovarian cancer cell lines for 48 hours. a) PEG-coated nanoparticles. Error bars represent standard deviations of  $n = 18$  of three independent experiments b) Definity® microbubbles. Error bars represent the standard deviation of 3 independent experiments.

### **3.4.2 Optimization of ultrasound conditions**

Microbubble-mediated ultrasound aims to maximize cell membrane poration and/or permeabilization, transiently altering the structure of cell membranes without affecting cell viability. To this end, effects of ultrasound pulse type, acoustic intensity ( $I$ ), exposure time ( $t_{US}$ ), and cell numbers were studied on HeyA8 cells, to optimize the ultrasound experimental conditions. Two response variables were monitored: cell viability and cell membrane permeabilization, measured immediately after ultrasound exposure.

#### **3.4.2.1 Effect of LIFU on cell viability**

Cells were sonicated at various acoustic intensities and exposure times, using continuous and pulsed ultrasound. Additionally, the effect low, medium or high cell populations during ultrasound exposure was also evaluated. As shown in Figure 3.3, continuous ultrasound caused cell detachment leading to reductions in the number of adherent cells, even at acoustic intensities as low as  $2 \text{ W/cm}^2$ . Cell detachment increased with acoustic intensity, reducing cell viability to 60% at  $5 \text{ W/cm}^2$ . Similar observations have been reported by others, suggesting that cell detachment due to continuous pulses is influenced by experimental conditions but it is also a cell type-dependent phenomenon<sup>47</sup>. Ultrasound-induced hyperthermia and inertial cavitation of microbubbles have also been identified as contributors for cell damage during ultrasound exposure, often associated with continuous pulses and/or high acoustic intensities<sup>48</sup>. Differently, a single application of pulsed ultrasound did induce cell detachment at the studied intensity values and exposure times thus making it potentially useful for further experiments.

Pulsed ultrasound is the most widely used platform in microbubble-mediated ultrasound due to the beneficial non-thermal mechanisms to induce cell sonoporation<sup>49</sup>. A second application of

pulsed ultrasound was performed one hour later to investigate the effect of consecutive ultrasound exposure. Compared to one-single pulse exposure, cell detachment occurred indicating that subsequent ultrasound exposures are not recommended. It is thought that after the first sonication, cell membranes and cytoskeletons are structurally affected and further sonications, even when pulsed, affect cell-to-cell interactions, leading to cell detachment. In addition, some studies report that in drug delivery applications, consecutive ultrasound exposure may lead to exocytosis of particles/molecules internalized into cells via ultrasound<sup>31</sup>. The exposure time was adjusted as a function of acoustic intensity, using smaller exposure times as the intensity increased. No major patterns were observed either at low or high exposure times, being intensity and pulse type the parameters mostly influencing cell viability. All these experiments were carried out with cell populations ranging in  $1.5 - 2.0 \times 10^6$  cells, therefore the effect of having other cell numbers during ultrasound exposure was also investigated. As shown in Figure 3.5b, low cell populations (e.g.  $1 \times 10^5$  cells) were susceptible to cell detachment when sonicated at ultrasound intensities above  $3 \text{ W/cm}^2$  ( $I_{\text{SPTA}} > 0.9 \text{ W/cm}^2$ ). As the intensity increased, major cell detachment occurred which led to significant reductions of cell viability. Groups that were less affected were those with  $5 \times 10^5$  cells, for which intensity of  $8.5 \text{ W/cm}^2$  ( $I_{\text{SPTA}} = 2.5 \text{ W/cm}^2$ ) was identified as the threshold without major cell detachment issues. Larger cell populations (e.g.  $1 \times 10^6$  cells) were observed to withstand intensity values as high as  $12 \text{ W/cm}^2$ , but beyond that point, major cell detachment was observed even for large cell populations. Such observations indicate that cell-to-cell interactions play an important role in response to stresses caused by microbubble cavitation. One possible reason behind ultrasound-induced cell detachment is the irreversible disassembly in tubulin networks as a consequence of disruption of microtubule integrity<sup>50</sup>. Low cell populations with disrupted microtubules have less

chance of overcoming cytoskeleton damage compared to higher cell densities where the increased cell proximity stabilizes cell-to-cell interactions, possibly reversing tubulin disassembly.

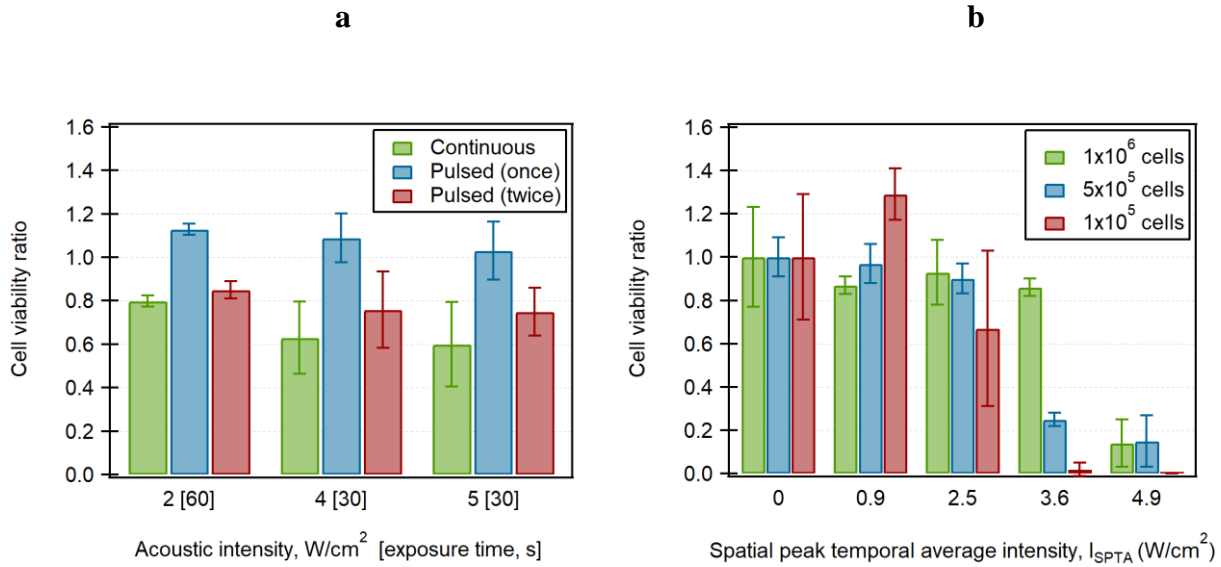


**Figure 3.3.** Effect of ultrasound experimental conditions on viability of HeyA8 cells. a) effect of pulse type at various acoustic intensities and exposure times. b) effect of cell numbers at various spatial peak temporal average intensities. Error bars represent the standard deviation of three independent experiments.

### 3.4.2.2 Effect of LIFU on cell membrane permeability

Ultrasound-induced cell membrane permeabilization was assessed via Sytox Green uptake by HeyA8 cells at various combinations of acoustic intensity and exposure times. Sytox Green is a molecule virtually non-fluorescent in aqueous solutions and impermeable to intact cell membranes. When cells have temporally or permanently compromised membranes, the dye easily penetrates cells emitting brilliant, green fluorescence upon binding to nucleic acids. As

shown in Figure 3.4, green fluorescence was observed in cells treated with different regimens of ultrasound (conditions A to D) when compared to non-sonicated cells. Hoechst 33342 was simultaneously used to stain nuclei of all cells for visualization purposes. The highest levels of green fluorescence were visualized in cells that exposed to ultrasound at  $I_{SPTA} = 1.8 \text{ W/cm}^2$  for 40 seconds (condition B) while higher intensities led to reductions in green fluorescence. Therefore, condition B represents the combination of acoustic intensity and exposure time to induce optimal cell membrane permeabilization in cells. As for the ultrasound exposure time, condition B showed slightly higher fluorescence in cells sonicated for 40 seconds, compared to those exposed for 20 seconds. At  $I_{SPTA}$  of  $2.5 \text{ W/cm}^2$  (conditions C and D), the effect of exposure time becomes irrelevant since the levels of green fluorescence decreased when compared to conditions A and B, regardless of the time that cells were exposed to ultrasound. Even when the chance of labeling dead cells with green fluorescence exists, fluorescence levels between viable and dead cells are different, which allows to distinguish between live and dead cells. Studies have demonstrated that green fluorescence levels emitted by Sytox Green in viable, sonoporated cells are significantly higher than those emitted by passive loading of the dye in dead cells by diffusion<sup>24</sup>. In addition, this work demonstrated that reductions in cell viability immediately after ultrasound exposure were mostly due to cell detachment. Detached cells during sonication were eliminated along with the excess of fluorescent dyes via extensive washing prior to imaging. Therefore, green fluorescence observed during in all groups was emitted virtually only by viable cells.

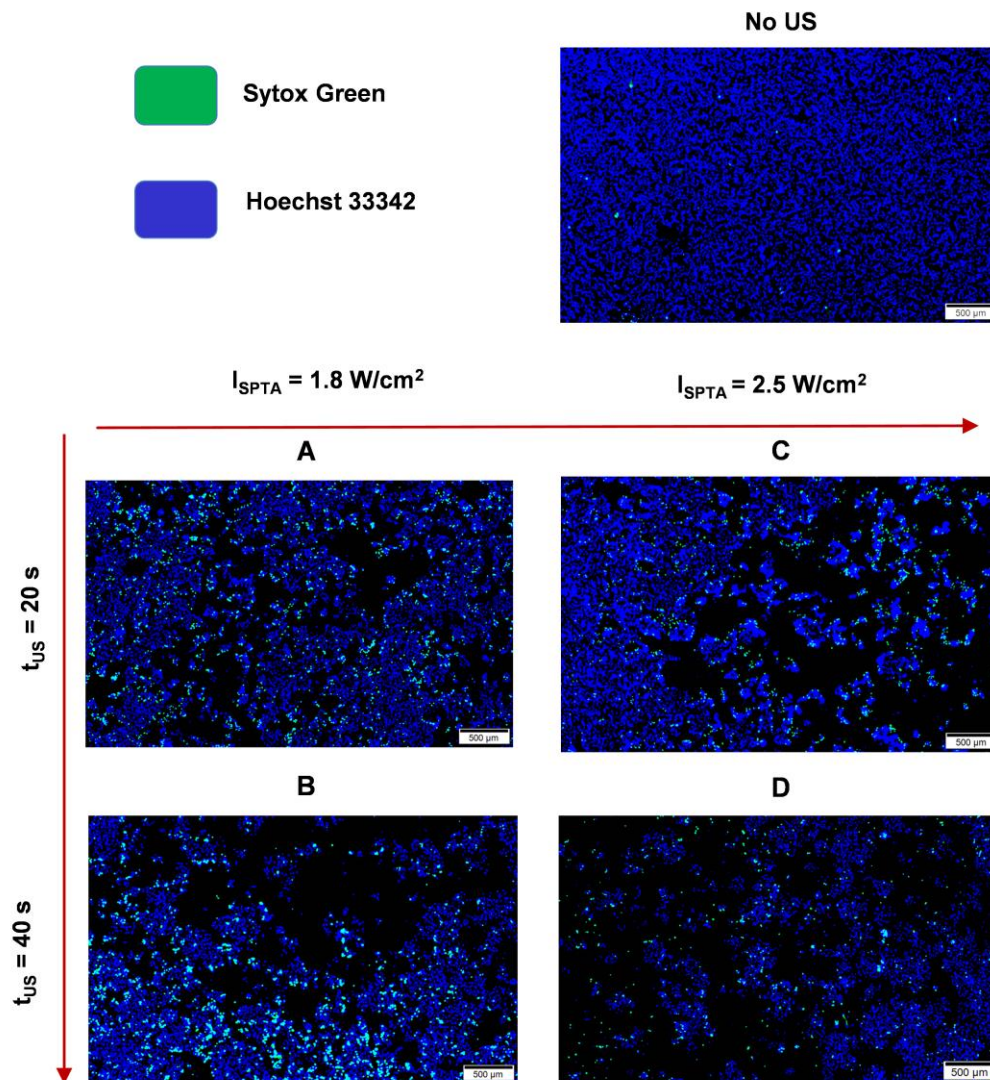


**Figure 3.4.** Live-cell fluorescence microscopy for the assessment ultrasound-mediated cell membrane permeabilization via Sytox Green uptake by HeyA8 cells. Conditions A to D represent various combinations of  $I_{SPTA}$  values and exposure time. Images show one of four representative areas evaluated per each sample. Error bars represent 500  $\mu\text{m}$ .

### 3.4.3 Nanoparticle internalization via non-specific uptake

Ovarian cancer cells incubated with colloidal suspensions of PEG-coated nanoparticles (0.6 mg iron oxide/mL) for up to 6 hours showed cell type- and time-dependent internalization

patterns, as depicted in Figure 3.5. Nanoparticle uptake by cells via non-specific uptake increased with time, resulting in iron uptake values up to 5  $\mu\text{g}_{\text{Fe}}/\text{cell}$  for HeyA8 cells, and 2 – 3  $\mu\text{g}_{\text{Fe}}/\text{cell}$  for A2780 and SKOV3 cells. The observed non-specific uptake of nanoparticles coated by PEG-Silane may be associated to a relatively low negative charge (zeta potential  $\sim -3$  mV at pH 7.4). Differences in iron uptake patterns among the studied cell lines may be associated with endocytic pathways. For example, Behzadi *et al.* suggests that PEG polymer coatings of nanoparticles induce their uptake via clathrin- and caveolae-mediated endocytosis<sup>51</sup>. The amount of clathrin and caveolin proteins mediating endocytic pathways may be different between cell lines thus intracellular accumulation of nanoparticles will not be the same for all cell lines. These common endocytic pathways have been reported by Feng *et al.* for the uptake of PEG-coated nanoparticles by SKOV3 cells, suggesting that upon internalization via non-specific uptake pathways, nanoparticles are subsequently located in endosomes and lysosomes<sup>52</sup>.

In addition, nanoparticle internalization was qualitatively assessed via confocal laser scanning microscopy, to observe nanoparticle localization within the cell. Results are shown in Figure 3.6 for control and experimental groups comprised of cells incubated with and without nanoparticles, respectively. In the pictures, the colors red, blue and green are fluorescence emitted by cell membrane, nuclei and nanoparticles, respectively, when stained/labelled with various fluorescent dyes. SKOV3 cells were incubated with Alexa Fluor® 488-labelled, PEG-coated nanoparticles (0.1 mg iron oxide/mL) for 1 hour. Green-fluorescent nanoparticles were visualized dispersedly in the cytoplasm, but also as brilliant dots, presumably as nanoparticle clusters inside endosomes or lysosomes. This assumption is supported by the work of Schweiger *et al.* who reported negatively charged iron oxide nanoparticles in endosomes and lysosomes after various incubation times with lung cancer cells<sup>53</sup>.

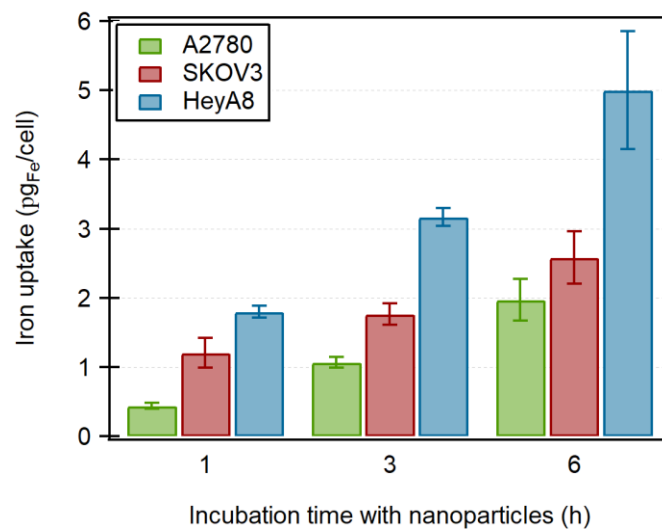


**Figure 3.5.** Cellular uptake of PEG-coated nanoparticles ( $0.6 \text{ mg}_{\text{IO}}/\text{mL}$ ) by ovarian cancer cells as quantified by UV/Vis spectroscopy. Error bars represent standard deviations of three independent experiments.

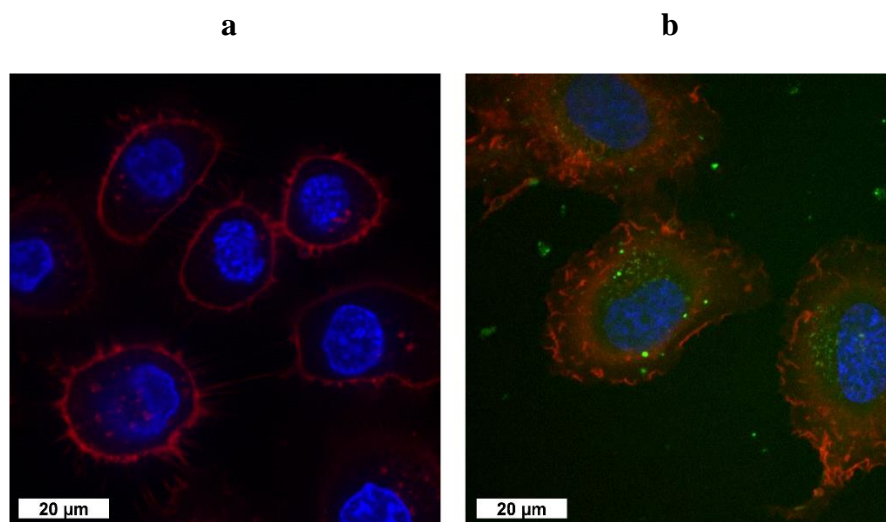


**Figure 3.6.** Localization of PEG-coated nanoparticles in SKOV3 cells, via confocal microscopy. a) cells without nanoparticles, b) cells incubated with nanoparticles ( $0.1 \text{ mg}_{\text{IO}}/\text{mL}$ ) for 1 hour. Nanoparticles, cell membranes and nuclei are depicted by green, red and blue fluorescence, respectively.

#### **3.4.4 Ultrasound-assisted nanoparticle internalization**

The effect of ultrasound on the cellular uptake of magnetic nanoparticles was studied under the same intensity-exposure time combinations used for Sytox Green uptake experiments. This allowed to quantitatively confirm whether optimal conditions that led to maximal uptake of Sytox Green are applicable to improve nanoparticle internalization. After ultrasound exposure in the presence of nanoparticles, cells were incubated for 5 or 12 hours to investigate the effect of cumulative internalization. Results are shown in Figure 3.7, where it can be noted that in the absence of ultrasound, non-specific uptake of nanoparticles by cells is a time-dependent phenomenon, as discussed in section 3.4.3. When compared to the control group (no ultrasound), cells that were sonicated showed improvements on nanoparticle internalization at the four intensity-exposure time combinations. However, cells sonicated at  $I_{SPTA}$  of  $1.8 \text{ W/cm}^2$  for 40 seconds showed significant improvements on nanoparticle internalization, with iron uptakes up to 3.7 and  $11.4 \text{ pg}_{\text{Fe}}/\text{cell}$  for 5 and 12 hours of incubation time with nanoparticles, respectively. This confirmed that ultrasound conditions identified as optimal for the uptake of Sytox Green were also those leading to optimal nanoparticle internalization.

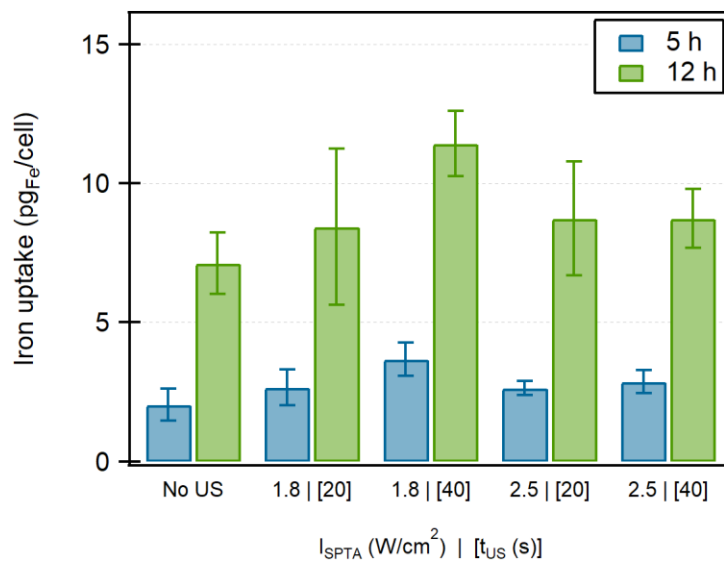


**Figure 3.7.** Ultrasound-assisted nanoparticle internalization into HeyA8 cells as a function of various  $I_{SPTA}$  values | [exposure time] conditions. Cells were incubated with nanoparticles for 5 or 12 hours. Error bars represent the standard deviation of three independent experiments.

Even when non-specific uptake occurred in a time-dependent fashion, the net improvement on iron uptake was similar regardless of the total incubation time with nanoparticles. As shown in Table 3.4, iron uptake ratios of 1.6 – 1.8 (sonication/no sonication) were obtained for cells incubated with nanoparticles either for 5 or 12 hours. In other words, even when the non-specific cellular uptake of iron time-dependent, the improved internalization patterns due to ultrasound occurred independently of the total incubation time with nanoparticles. This would suggest that improvements on nanoparticle internalization with the use of ultrasound could take place in the short term.

**Table 3.4.** Normalized iron uptake values expressed as the ratio between uptake achieved with ultrasound, divided by that obtained in the absence of ultrasound.

<b>I<sub>SPTA</sub>, W/cm<sup>2</sup>   [t<sub>US</sub>, s]</b>	<b>5 hours</b>	<b>12 hours</b>
1.8   [20]	1.3	1.2
1.8   [40]	1.8	1.6
2.5   [20]	1.3	1.2
2.5   [40]	1.4	1.2

The work of Kolarova *et al.* is an example, with improvements on iron uptake determined as fast as one minute-post sonication when compared to 24-hour internalization without ultrasound<sup>37</sup>. The reduced uptake patterns in sonications carried out at 8.5 W/cm<sup>2</sup> (continuous ultrasound) could be the result of impaired equilibria between facilitated internalization and exocytosis during resealing of cell membranes. As explained by Lentacker *et al.*, resealing of membrane pores may trigger exocytosis because of reduced membrane tension and intracellular vesicle trafficking<sup>26</sup>. McNeil *et al.* explain that self-sealing of pores on cell membranes usually occurred only for small pores<sup>54</sup>. Therefore, higher intensities could induce the formation of bigger pores which are unable to self-seal with time, leading to losses of internalized molecules or nanoparticles. Yet, it has been demonstrated that optimized ultrasound conditions led to significant improvements on the cellular uptake of drug models (Sytox Green) and magnetic nanoparticles. The obtained results are of special relevance for the design of drug/MFH combined therapies, using ultrasound for improved drug/nanoparticle internalization profiles.

### **3.4.5 MFH and ultrasound-assisted PES/MFH combined therapies**

This section features the effects of MFH-induced heat in ovarian cancer cells, both as a single therapy and with the incorporation of PES and LIFU. All magnetic treatments were performed for 30 min at magnetic field intensity ( $H_o$ ) ranging in 15 – 20 kA/m and frequency ( $f$ ) of 245 kHz, and cell viabilities were analyzed 48 hours after MFH.

#### **3.4.5.1 Cytotoxicity of MFH and PES as individual treatments**

Exposure to alternating magnetic fields (AMF) and to 2-phenylethanesulfonamide (PES) was studied separately, to evaluate cytotoxic effects of the magnetic and chemical therapies, respectively. For MFH experiments, the magnetic field intensity ( $H_o$ ) was adjusted to achieve sustained temperatures of 43° and 45°C for the 30-min exposure time. For PES cytotoxicity evaluation, cells were incubated with various drug concentrations for up to 72 hours. Results are shown in Figure 3.8 As a response to MFH therapy, reductions on cell viability were observed 48 hours after magnetic treatments for the three cell lines in cell type- and temperature-dependent patterns (Figure 3.7a). Even when cell types responded differently to heat stresses, apoptotic cell death occurred, as it has been demonstrated elsewhere<sup>55</sup>. However, other modes of cell death have been reported such as immunogenic effects of heat-shock proteins (HSP), signal transduction, necrosis, and others<sup>56</sup>. All cell lines showed significant cytotoxic effects with MFH treatment at 43°C, and even stronger effects at 45°C, with cell viabilities reduced down to 7% in some cases. Similar results have been reported for A2780 and HeyA8 cells using comparable experimental conditions for carboxymethyl dextran-coated nanoparticles<sup>14</sup>. As for the cytotoxic effect of MFH among the evaluated cell lines it was found that cells responded differently to hyperthermia, with cell viabilities in the order SKOV3 > HeyA8 > A2780 at both 43 and 45°C.

This behavior has been previously reported by Hatakeyama *et al.* for these and other ovarian cancer cells, classifying SKOV3 and A2780 as hyperthermia-resistant and hyperthermia-sensitive, respectively<sup>57</sup>. In addition, no cytotoxic effects were observed for cells incubated with magnetic nanoparticles in the absence of magnetic fields, or exposure of cells to AMF without nanoparticles. This confirms that cell death during MFH is due to only to heat released by nanoparticles when exposed to AMF rather than toxic effects of nanoparticles or non-specific heating.

Incubation of HeyA8 cells with various concentrations of PES resulted in decreased cell viability as PES concentrations and incubation times were increased. Results are presented as the dose-response curve shown in Figure 3.8b. Yet, inhibitory concentration ( $IC_{50}$ ) values could not be determined for 24- and 48-hour incubation times because cell viabilities were not decreased below 75% in the entire range of drug concentration. Incubation for 72 hours showed increased cytotoxic effect with  $IC_{50}$  of approximately 28  $\mu\text{M}$  and reductions on cell viability down to 40% for PES concentration of 50  $\mu\text{M}$ . Among the intracellular effects of PES, inhibition of the HSP70 function has been reported to trigger some cell death pathways including protein aggregation, impaired autophagy and inhibition of lysosomal function<sup>58</sup>. From the dose-response curve, 10  $\mu\text{M}$  was chosen as the non-cytotoxic drug concentration, intended to be potentiated by hyperthermia and/or ultrasound.

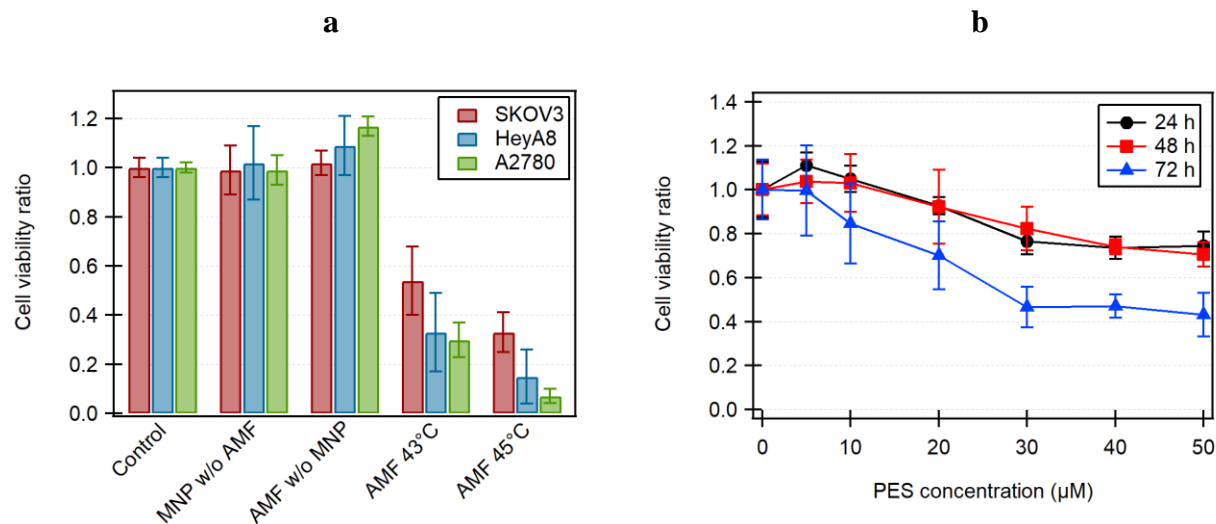


**Figure 3.8.** Viability ratio of ovarian cancer cells after exposure to MFH and PES. a) AMF ( $H_o = 15 - 20$  kA/m,  $f = 245$  kHz) exposure for 30 min. Control groups represent cells incubated at  $37^\circ\text{C}$ , “MNP w/o AMF” group represents cells incubated with MNP in the absence of AMF, and “AMF w/o MNP” represents cells exposed to AMF in the absence of MNP. Error bars represent the standard deviation of three independent experiments. b) Incubation of HeyA8 cells with various PES concentrations for up to 72 hours. Error bars represent the standard deviation of  $n = 6$ .

### 3.4.5.2 Ultrasound-assisted PES/MFH combined therapies

Once suitable ultrasound (US) conditions and drug (PES) concentrations were identified without major effects on ovarian cancer cell viability, their incorporation with MFH platforms was pursued. Since moderate hyperthermia temperatures ( $T \geq 43^\circ\text{C}$ ) strongly decreased cell viability, mild hyperthermia conditions were suggested for combination treatments. Some studies report that viability of HeyA8 are either minimally or not affected at all during exposure to MFH at  $41^\circ\text{C}$  for up to 60 min<sup>14,57</sup>. Therefore, a comparison of mild and moderate hyperthermia for 30 minutes was carried out, evaluating the sono-, chemo-, and thermo-therapies as individual, dual combinations, and triple combinations. Results are depicted in Figure 3.9 showing the viability ratio of HeyA8 cells exposed to ultrasound (US) and subsequently (12 hours later) exposed to

MFH at sustained temperatures of 41 and 43°C for 30 min. Small reductions on cell viability were observed for MFH at 41°C, whereas PES concentrations did not have any effect on cells, as observed in previous experiments. The rationale behind using mild hyperthermia conditions without major effects on cells made easier to investigate the impact of US and PES on MFH. In other words, once demonstrated that the three therapies are not toxic for cells applied individually, it was hypothesized that combined therapies would potentiate their effects on cancer cell viability. When cells were sonicated in the presence of the drug (US+PES), significant reductions on cell viability were observed when compared to non-cytotoxic effects of cells incubated with PES. Hence, it was demonstrated that US potentiates the effect of otherwise non-cytotoxic drug concentrations due to sonoporation-increased intracellular drug concentrations. When cells were incubated with PES for twelve hours and subsequently exposed to MFH at 41 and 43°C (PES+MFH), significant reductions were observed with respect of PES and MFH individual treatments, respectively. These results confirmed the observations made by Court *et al.* demonstrating that potentiation of PES with MFH was consistently obtained. Notably, sonication of cells with PES and nanoparticles, and subsequently exposed to MFH at 41 and 43°C twelve hours later, significantly increased cell death when compared to PES+MFH, at both temperatures. Such observations tested the hypothesis that improved cancer cell killing profiles could be achieved when using ultrasound to enhance the effects of MFH and PES, both individually and combined. Such improvements were more perceptible at hyperthermia temperatures of 41°C, with significant differences between PES+MFH and US+PES+MFH. In the case of MFH at 43°C, the tendency of increased cell death was also evident in the two mentioned groups, yet not statistically significant. As mentioned before, MFH at 43°C is more aggressive for cells as a single treatment, greatly reducing viability of cell populations. With the

incorporation of additional treatments, the cell killing effect is enhanced thus cell populations are further reduced. Therefore, comparisons between groups with very small number of viable cells makes it difficult to distinguish whether significant differences are obtained or not, thus disguising relevant findings. For this reason, it was decided to continue subsequent studies with MFH at 41°C, which in addition is a representative temperature of hyperthermia levels achievable *in vivo*.

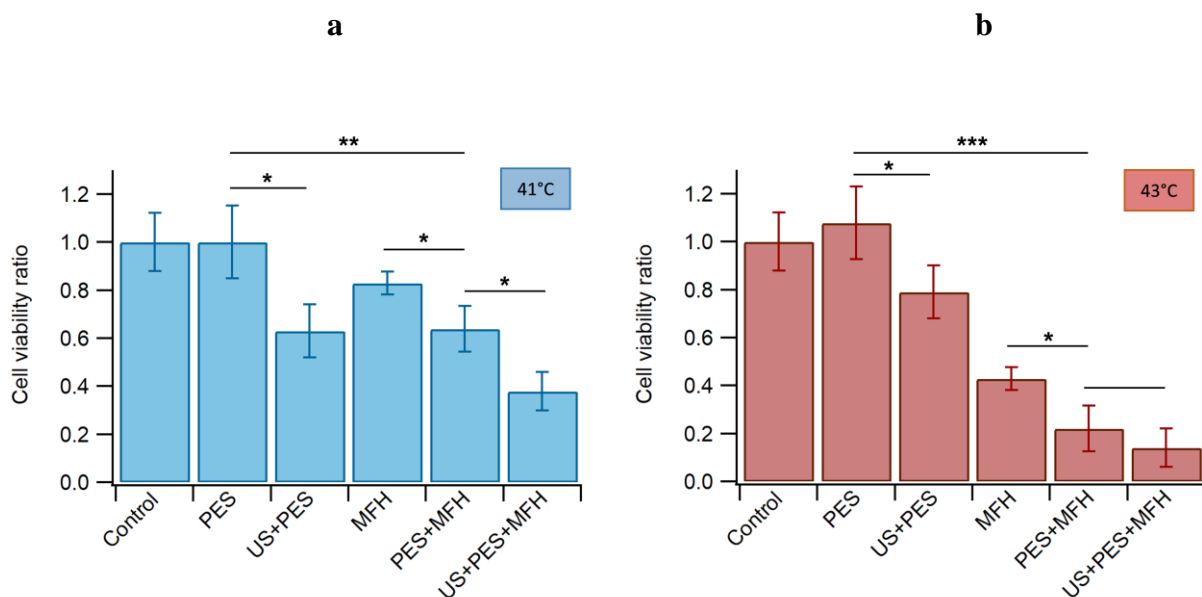


**Figure 3.9.** Viability ratio of HeyA8 cells after combination treatments of ultrasound (US), drug (PES) and hyperthermia (MFH). a) MFH at 41°C and, b) MFH at 43°C. AMF conditions were  $H_o = 15 - 20$  kA/m,  $f = 245$  kHz, exposure time: 30 min. Cells were sonicated twelve hours before AMF exposure. Error bars represent the standard deviation of three independent experiments.

The idea of exposing cells to AMF twelve hours after sonications was to allow sufficient time for nanoparticles to cross permeabilized membranes, via non-specific uptake and transport across pores in membranes, hence maximizing their internalization into cells. To test the effect of

ultrasound-assisted nanoparticle internalization, additional experiments were conducted by removing nanoparticles twelve-hour after incubation, right before exposure to AMF. In this case, no perceptible temperature rise was expected in the bulk medium because of the lack of nanoparticles in the bulk medium. Therefore, energy delivery should be due to heat dissipated by internalized nanoparticles only and/or those crossing the cell membrane. Results are shown in Figure 3.10, comparing cell viabilities of groups with AMF exposure with bulk heating (MFH, 41°C) and those without macroscopic heating (MagMED, 37°C). Cells exposed to AMF as MagMED showed decreased viability with respect of the control, suggesting local heating effects of internalized nanoparticles via non-specific uptake took place. This can be confirmed by comparing the group AMF with group AMF w/o MNP in Figure 3.8a, which consisted of cells that exposed to AMF in the absence of magnetic nanoparticles. Importantly, the temperature of the bulk medium in groups with MagMED never exceeded 37°C, which was the temperature of the surroundings during the execution of experiments. Viability of cells treated with US+PES+MagMED showed an additional decrease when compared to AMF group, indicating the additional effect of ultrasound-assisted internalization. When compared to their MFH counterpart, no major improvements on cell killing profiles were observed, indicating the cellular damage produced by local heating effects was not significantly different. This can be confirmed by comparing cell viabilities of groups AMF and US+AMF (MagMED) which in average, were comparable patterns of cell damage. Conversely, by comparing the same groups in MFH platform, it can be noted that ultrasound significantly improved cell killing profile with macroscopic heating.

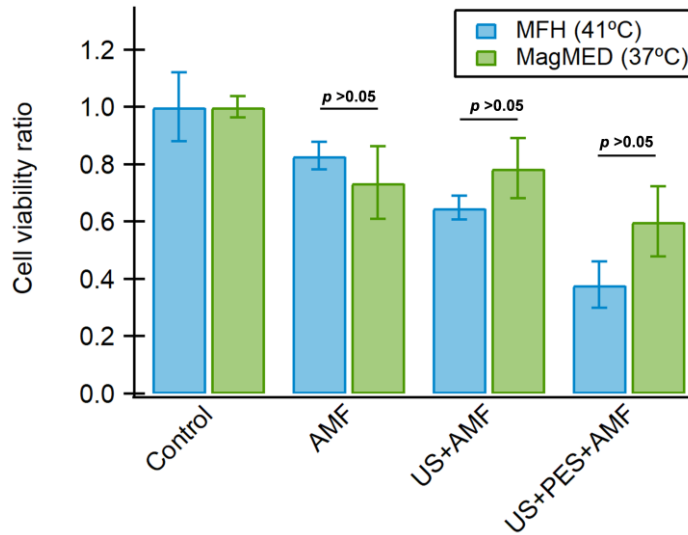


**Figure 3.10.** Comparison of cell viability upon alternating magnetic fields (AMF) exposure between cells groups with nanoparticles in the bulk medium (MFH at 41°C) and groups with removed nanoparticles (MagMED 37°C). Cells were sonicated (US) 12 hours before AMF exposure ( $H_o = 15 - 20$  kA/m,  $f = 245$  kHz, exposure time = 30 min). Error bars represent the standard deviation of three independent experiments.

Comparisons between heating effects platforms suggest that cellular damage induced by US+PES+MFH combination therapies is the result of increased intracellular PES concentrations via ultrasound. In addition, it was demonstrated that net improvements on nanoparticle internalization were similar regardless of the total incubation time with nanoparticles. In such case case, it would seem like it is not necessary to incubate cells with nanoparticles and PES for long time periods after ultrasound exposure. To test this hypothesis, MFH experiments at 41°C were conducted in a similar fashion as those previously discussed, but cells were sonicated 30 minutes before exposure to AMF. As shown in Figure 3.11, the tendency of the various combination treatments is essentially the same as that observed when cells were sonicated twelve hours before exposure to AMF. Importantly, no significant differences were observed for the treatments when ultrasound is applied either 12 hours or 30 minutes before AMF exposure. Therefore, it was confirmed that ultrasound can be applied right before AMF exposure yet

having the same outcome. The simultaneous application of ultrasound, PES and MFH was observed to induce major cell death when compared to individual or dual treatments, regardless of the time spent between sonication of cells and exposure to AMF. The use of low-intensity ultrasound to enhance the cellular uptake of PES and nanoparticles was confirmed, potentiating the cytotoxic effect of PES or MFH as individual therapies. More importantly, sonosensitivity of PES was demonstrated, and it was subsequently potentiated when incorporating heat dissipated by magnetic nanoparticles. It is evident that increased intracellular concentrations of PES and nanoparticles can be achieved with ultrasound, and it was demonstrated in this work.

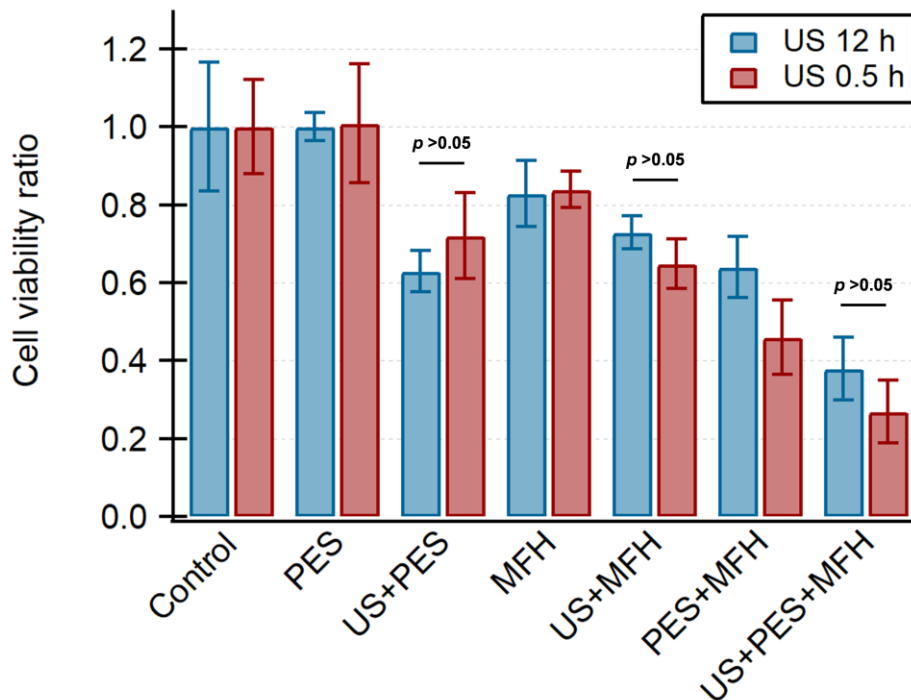


**Figure 3.11.** Comparison of US/PES/MFH combination therapies with bulk heating at 41°C. Cells were sonicated either 12 hours (blue bars) or 30 minutes (red bars) before exposure to AMF ( $H_o = 15 - 20$  kA/m,  $f = 245$  kHz, exposure time = 30 min). Error bars represent the standard deviation of three independent experiments.

The improved cell killing profiles of US+PES+MFH combination treatments are due to increased disruption of lysosomal membranes, as a consequence of higher intracellular PES concentrations via ultrasound. Upon lysosomal membrane disruption, significant amounts of lysosomal contents are released in the cytoplasm, inducing apoptotic and/or necrotic cell death. Earlier in this Chapter it was mentioned that PES inhibits the function of stress-inducible HSP70 proteins, which supports lysosome membrane integrity<sup>59</sup>. Therefore, higher concentrations of PES achieved via sonoporation increased the inhibitory effect on HSP70 function, causing significant damage to lysosomal membranes, which is potentiated by thermal effects. Yet, demonstrating these and additional mechanisms by which the sono/thermal potentiation of PES leads to substantial cancer cell death may be the subject of further investigations.

### **3.5 Conclusions**

Substantial improvements in ovarian cancer cell killing profiles were observed via ultrasonic potentiation of MFH/PES combined therapies. The use of ultrasound improved the cell killing profile of PES and MFH, both separately and as combined therapies, respectively, demonstrating ultrasound-enhanced cellular uptake of PES and magnetic nanoparticles. These improvements were achieved after a systematic optimization of ultrasound conditions, to achieve maximum cell membrane permeability and minimum damage to cells during ultrasound exposure. To the best of our knowledge, this is the first time that low-intensity focused ultrasound is used to potentiate the effects of magnetic fluid hyperthermia as adjuvant in cancer chemotherapy. It was demonstrated that the cytotoxic profile of the novel chemotherapeutic agent PES can be greatly potentiated by the concomitant administration of heat and ultrasound, using an *in vitro* ovarian cancer model. Hence, it is expected that the work presented here has the potential to be considered as a part of a novel sono-thermo-chemotherapy.

### 3.6 References

1. Qu, Y. *et al.* Enhanced synergism of thermo-chemotherapy by combining highly efficient magnetic hyperthermia with magnetothermally-facilitated drug release. *Nanoscale* **6**, 12408–12413 (2014).
2. Torres-Lugo, M. & Rinaldi, C. Thermal potentiation of chemotherapy by magnetic nanoparticles. *Nanomedicine (Lond)*. **8**, 1689–707 (2013).
3. Ohno, S., Siddik, Z. H., Kido, Y., Zwelling, L. A. & Bull, J. M. C. Thermal enhancement of drug uptake and DNA adducts as a possible mechanism for the effect of sequencing hyperthermia on cisplatin-induced cytotoxicity in L1210 cells. *Cancer Chemother. Pharmacol.* **34**, 302–306 (1994).
4. Xu, H., Ju, D., Jarois, T. & Xie, Y. Diminished feedback regulation of proteasome expression and resistance to proteasome inhibitors in breast cancer cells. *Breast Cancer Res. Treat.* **107**, 267–274 (2008).
5. Zakris, E. L. *et al.* Pharmacokinetics and toxicity of intraperitoneal cisplatin combined with regional hyperthermia. *J. Clin. Oncol.* **5**, 1613–1620 (1987).
6. Rietbroek, R. C. *et al.* Phase II trial of weekly locoregional hyperthermia and cisplatin in patients with a previously irradiated recurrent carcinoma of the uterine cervix. *Cancer* **79**, 935–43 (1997).
7. Gobbo, O. L., Sjaastad, K., Radomski, M. W., Volkov, Y. & Prina-Mello, A. Magnetic Nanoparticles in Cancer Theranostics. *Theranostics* **5**, 1249–1263 (2015).

8. Lee, J. S. *et al.* Hyperthermia Induced by Magnetic Nanoparticles Improves the Effectiveness of the Anticancer Drug cis-Diamminedichloroplatinum. *J. Nanosci. Nanotechnol.* **11**, 4153–4157 (2011).
9. Alvarez-Berrios, M. P. *et al.* Hyperthermic potentiation of cisplatin by magnetic nanoparticle heaters is correlated with an increase in cell membrane fluidity. *Int. J. Nanomedicine* **8**, 1003–1013 (2013).
10. Alvarez-Berrios, M. P., Castillo, A., Rinaldi, C. & Torres-Lugo, M. Magnetic fluid hyperthermia enhances cytotoxicity of bortezomib in sensitive and resistant cancer cell lines. *Int. J. Nanomedicine* **9**, 145–53 (2014).
11. Eynali, S., Khoei, S., Khoei, S. & Esmaelbeygi, E. Evaluation of the cytotoxic effects of hyperthermia and 5-fluorouracil-loaded magnetic nanoparticles on human colon cancer cell line HT-29. *Int. J. Hyperth.* **33**, 327–335 (2017).
12. Yang, Y. *et al.* Injectable PLGA/Fe<sub>3</sub>O<sub>4</sub> implants carrying cisplatin for synergistic magnetic hyperthermal ablation of rabbit VX2 tumor. *PLoS One* **12**, e0177049 (2017).
13. Li, M. *et al.* Enhanced synergism of thermo-chemotherapy for liver cancer with magnetothermally responsive nanocarriers. *Theranostics* **8**, 693–709 (2018).
14. Court, K. A. *et al.* HSP70 Inhibition Synergistically Enhances the Effects of Magnetic Fluid Hyperthermia in Ovarian Cancer. *Mol. Cancer Ther.* **16**, 966–976 (2017).
15. Arami, H., Khandhar, A., Liggitt, D. & Krishnan, K. M. In vivo delivery, pharmacokinetics, biodistribution and toxicity of iron oxide nanoparticles. *Chem. Soc.*

- Rev.* **44**, 8576–8607 (2015).
16. Chiu-Lam, A. & Rinaldi, C. Nanoscale Thermal Phenomena in the Vicinity of Magnetic Nanoparticles in Alternating Magnetic Fields. *Adv. Funct. Mater.* n/a-n/a (2016). doi:10.1002/adfm.201505256
  17. Creixell, M. *et al.* Preparation of epidermal growth factor (EGF) conjugated iron oxide nanoparticles and their internalization into colon cancer cells. *J. Magn. Magn. Mater.* **322**, 2244–2250 (2010).
  18. Creixell, M., Bohórquez, A. C., Torres-lugo, M. & Rinaldi, C. EGFR-Targeted Magnetic Nanoparticle Heaters Kill Cancer Cells Without A Sensible Temperature Rise . 3–8
  19. Domenech, M., Marrero-Berrios, I., Torres-Lugo, M. & Rinaldi, C. Lysosomal membrane permeabilization by targeted magnetic nanoparticles in alternating magnetic fields. *ACS Nano* **7**, 5091–101 (2013).
  20. Chen, W. C., Zhang, A. X. & Li, S. D. Limitations and niches of the active targeting approach for nanoparticle drug delivery. *Eur. J. Nanomedicine* **4**, 89–93 (2012).
  21. Li, S. D., Chen, Y. C., Hackett, M. J. & Huang, L. Tumor-targeted delivery of siRNA by self-assembled nanoparticles. *Mol. Ther.* **16**, 163–169 (2008).
  22. Lammertink, B. H. A. *et al.* Sonochemotherapy: From bench to bedside. *Front. Pharmacol.* **6**, (2015).
  23. Paliwal, S. & Mitragotri, S. Therapeutic opportunities in biological responses of ultrasound. *Ultrasonics* **48**, 271–8 (2008).

24. Yudina, A., Lepetit-Coiffé, M. & Moonen, C. T. W. Evaluation of the temporal window for drug delivery following ultrasound-mediated membrane permeability enhancement. *Mol. Imaging Biol.* **13**, 239–49 (2011).
25. Domenici, F. *et al.* Structural and permeability sensitivity of cells to low intensity ultrasound: Infrared and fluorescence evidence in vitro. *Ultrasonics* **54**, 1020–8 (2014).
26. Lentacker, I., De Cock, I., Deckers, R., De Smedt, S. C. & Moonen, C. T. W. Understanding ultrasound induced sonoporation: Definitions and underlying mechanisms. *Adv. Drug Deliv. Rev.* **72**, 49–64 (2014).
27. Kooiman, K., Emmer, M., Foppen-Harteveld, M., Van Wamel, A. & De Jong, N. Increasing the endothelial layer permeability through ultrasound-activated microbubbles. *IEEE Trans. Biomed. Eng.* **57**, 29–32 (2010).
28. Sheikov, N., McDannold, N., Vykhodtseva, N., Jolesz, F. & Hynynen, K. Cellular mechanisms of the blood-brain barrier opening induced by ultrasound in presence of microbubbles. *Ultrasound Med. Biol.* **30**, 979–989 (2004).
29. Blanco, E., Shen, H. & Ferrari, M. Principles of nanoparticles design for overcoming biological barriers for drug delivery. *Nat Biotechnol* **33**, 941–951 (2015).
30. Minchinton, A. I. & Tannock, I. F. Drug penetration in solid tumours. *Nat. Rev. Cancer* **6**, 583–592 (2006).
31. Juffermans, L. J. M., Kamp, O., Dijkmans, P. A., Visser, C. A. & Musters, R. J. P. Low-Intensity Ultrasound-Exposed Microbubbles Provoke Local Hyperpolarization of the Cell

- Membrane Via Activation of BKCa Channels. *Ultrasound Med. Biol.* **34**, 502–508 (2008).
32. Baghbani, F. & Moztarzadeh, F. Bypassing multidrug resistant ovarian cancer using ultrasound responsive doxorubicin/curcumin co-deliver alginate nanodroplets. *Colloids Surfaces B Biointerfaces* **153**, 132–140 (2017).
  33. Sun, J. *et al.* Ultrasound-mediated destruction of oxygen and paclitaxel loaded lipid microbubbles for combination therapy in hypoxic ovarian cancer cells. *Ultrason. Sonochem.* **28**, 319–326 (2016).
  34. Escoffre, J. M., Piron, J., Novell, A. & Bouakaz, A. Doxorubicin delivery into tumor cells with ultrasound and microbubbles. *Mol. Pharm.* **8**, 799–806 (2011).
  35. Sorace, A. G., Warram, J. M., Umphrey, H. & Hoyt, K. Microbubble-mediated ultrasonic techniques for improved chemotherapeutic delivery in cancer. *J. Drug Target.* **20**, 43–54 (2012).
  36. Heath, C. H., Sorace, A., Knowles, J., Rosenthal, E. & Hoyt, K. Microbubble Therapy Enhances Anti-tumor Properties of Cisplatin and Cetuximab In Vitro and In Vivo. *Otolaryngol. Neck Surg.* **146**, 938–945 (2012).
  37. Kolářová, M. *et al.* Rapid Cellular Uptake of Superparamagnetic Iron Oxide Nanoparticles By Using Low-Intensity Ultrasound. (2013).
  38. Yang, F. *et al.* Altering the response of intracellular reactive oxygen to magnetic nanoparticles using ultrasound and microbubbles. *Sci. China Mater.* **58**, 467–480 (2015).
  39. Yang, F. *et al.* Controlled release of Fe<sub>3</sub>O<sub>4</sub> nanoparticles in encapsulated microbubbles to

- tumor cells via sonoporation and associated cellular bioeffects. *Small* **7**, 902–10 (2011).
40. Chen, P.-Y. *et al.* Novel magnetic/ultrasound focusing system enhances nanoparticle drug delivery for glioma treatment. *Neuro. Oncol.* **12**, 1050–60 (2010).
  41. Wang, Y.-X. J. *et al.* Low-intensity pulsed ultrasound increases cellular uptake of superparamagnetic iron oxide nanomaterial: Results from human osteosarcoma cell line U2OS. *J. Magn. Reson. Imaging* **31**, 1508–1513 (2010).
  42. Mo, R., Yang, J., Wu, E. X. & Lin, S. Instant magnetic labeling of tumor cells by ultrasound in vitro. *J. Magn. Mater.* **323**, 2287–2294 (2011).
  43. Rodríguez Negrón, L. Physiological effects of focused ultrasound pulsation schemes on amphibian peripheral nerve structures. (University of Puerto Rico, Mayagüez Campus, 2016).
  44. Santiago-Rodríguez, L. *et al.* Synthesis, stability, cellular uptake, and blood circulation time of carboxymethyl-inulin coated magnetic nanoparticles. *J. Mater. Chem. B* **1**, 2807 (2013).
  45. Choi, S. Y. *et al.* Multiple cell death pathways are independently activated by lethal hypertonicity in renal epithelial cells. *AJP Cell Physiol.* **305**, C1011–C1020 (2013).
  46. Shekhar, H., Smith, N. J., Raymond, J. L. & Holland, C. K. Effect of Temperature on the Size Distribution, Shell Properties, and Stability of Definity<sup>®</sup>. *Ultrasound Med. Biol.* **44**, 434–446 (2017).
  47. Yu, H. & Xu, L. Cell experimental studies on sonoporation: State of the art and remaining

- problems. *J. Control. Release* **174**, 151–160 (2014).
48. Dalecki, D. Mechanical bioeffects of ultrasound. *Annu. Rev. Biomed. Eng.* **6**, 229–48 (2004).
  49. ter Haar, G. Therapeutic applications of ultrasound. *Prog. Biophys. Mol. Biol.* **93**, 111–29 (2007).
  50. Fan, P. *et al.* Cell-cycle-specific Cellular Responses to Sonoporation. *Theranostics* **7**, 4894–4908 (2017).
  51. Behzadi, S. *et al.* Cellular uptake of nanoparticles: journey inside the cell. *Chem. Soc. Rev.* **46**, 4218–4244 (2017).
  52. Feng, Q. *et al.* Uptake, distribution, clearance, and toxicity of iron oxide nanoparticles with different sizes and coatings. *Sci. Rep.* **8**, 1–13 (2018).
  53. Schweiger, C. *et al.* Quantification of the internalization patterns of superparamagnetic iron oxide nanoparticles with opposite charge. *J. Nanobiotechnology* **10**, 1–11 (2012).
  54. McNeil, P. L. & Steinhardt, R. A. Plasma Membrane Disruption: Repair, Prevention, Adaptation. *Annu. Rev. Cell Dev. Biol.* **19**, 697–731 (2003).
  55. Rodríguez-Luccioni, H. L. *et al.* Enhanced reduction in cell viability by hyperthermia induced by magnetic nanoparticles. *Int. J. Nanomedicine* **6**, 373–80 (2011).
  56. Hildebrandt, B., Wust, P. & Ahlers, O. The cellular and molecular basis of hyperthermia. *Crit. Rev. ...* **43**, 33–56 (2002).

57. Hatakeyama, H. *et al.* Role of CTGF in Sensitivity to Hyperthermia in Ovarian and Uterine Cancers. *Cell Rep.* **17**, 1621–1631 (2016).
58. Leu, J. I.-J., Pimkina, J., Frank, A., Murphy, M. E. & George, D. L. A Small Molecule Inhibitor of Inducible Heat Shock Protein 70. *Mol. Cell* **36**, 15–27 (2009).
59. Granato, M. *et al.* HSP70 inhibition by 2-phenylethanesulfonamide induces lysosomal cathepsin D release and immunogenic cell death in primary effusion lymphoma. *Cell Death Dis.* **4**, 1–9 (2013).

# Chapter 4

## ***Intraperitoneal administration of magnetic nanoparticles and their uptake by mouse peritoneal macrophages.***

---

### **4.1 Summary**

The intravenous (IV) injection of magnetic nanoparticles has been a commonly used approach for *in vivo* Magnetic Fluid Hyperthermia (MFH) and other biomedical applications, by which nanoparticles are allowed to travel through the systemic circulation after their injection. Under this approach, nanoparticle extravasation from vasculature occurs with subsequent retention, mostly in tumors rather than healthy tissues, due to the leaky tumor neovasculature and inefficient lymphatic drainage<sup>1</sup>. This phenomenon is used to passively target magnetic nanoparticles to tumors in cancer therapy, and as described in Chapter 1, and it is known as the Enhanced Permeability and Retention (EPR) effect<sup>2</sup>. A major drawback of IV injection is the low delivery efficiency in tumors, characterized by a very small percentage of the nanoparticle dose originally injected. In fact, it has been reported that only ~ 0.7% of the injected dose (ID) reach tumors and such efficiency has remained the same in the past ten years<sup>3</sup>. Nanoparticles with targeting ligands have been engineered to actively target overexpressed receptors or growth factors in cancer cells, improving specificity thus increasing nanoparticle accumulation in tumors. Yet, targeted nanoparticles injected via IV face three major limitations: immunogenicity, impaired tumor penetration, and high susceptibility to lysosomal degradation, and such limitations have led to decreased blood circulation times<sup>4</sup>. Upon IV injection, circulating monocytes in the bloodstream sequester nanoparticles and take them to the liver and spleen where nanoparticles are finally phagocytosed by tissue-resident macrophages for further

metabolism. Coating nanoparticles with biocompatible polymers such as polyethylene glycol (PEG) minimizes the uptake by the tissue-residents macrophages in the liver. However, depending on the nanoparticle physical properties, further accumulation in the spleen can occur as a consequence of plasma protein adsorption onto nanoparticles<sup>5</sup>. Intratumoral (IT) injection of nanoparticles has also been used for *in vivo* MFH, aiming to accumulate higher nanoparticle concentrations in the tumor to achieve temperatures at the hyperthermia levels<sup>6</sup>. From a clinical point of view, IT injection is highly invasive especially for deep tumors in which an adequate tumor coverage cannot be achieved. IT injection then becomes unrealistic when treating small metastatic tumors<sup>7</sup>. One alternative is the intraperitoneal (IP) administration of nanoparticles which is an attractive approach especially for cancers developing in the peritoneal cavity such as ovarian and gastric cancers<sup>8</sup>. The rationale behind IP injection of nanoparticles is to promote macrophage-mediated transport of nanoparticles to intraperitoneal tumors thus enhancing the effects of MFH. This chapter features the work carried out with an *in vivo* breast cancer model, comparing pharmacokinetics and biodistribution of nanoparticles injected via IP and IV. Furthermore, IP nanoparticle injection was used to investigate the cellular uptake of nanoparticles by peritoneal macrophages. It was hypothesized that nanoparticle accumulation in tumors using IP injection would be lower than that achieved with IV injection. However, it was expected that high nanoparticle accumulation would take place in peritoneal regions such as omental tissues and inside peritoneal macrophages, via IP injection. Results revealed that IP administration of nanoparticles is a promising alternative to immune cells in the peritoneal cavity, thus promoting the cellular uptake of nanoparticles by peritoneal macrophages.

## 4.2 Introduction and literature review

The IP route of administration provides a pharmacokinetic benefit: a relatively high concentration and longer half-life of the injected agent in the peritoneal cavity<sup>8</sup>. The latter occurs because nanoparticles are bigger when compared to free molecules which reduces nanoparticle clearance from the IP cavity thus increasing their residence time. The development of intraperitoneal cancers is characterized by the attachment of cancer cells to the omentum, specifically in regions of aggregated inflammatory cells known as “milky spots” which are also rich in macrophages<sup>9</sup>. These milky spots facilitate the adhesion of cancer cells cleared from the intraperitoneal cavity thus promoting the formation of solid tumors in the omentum. As the tumor continues to grow, more macrophages from the peritoneal cavity are recruited to the tumor site, especially large peritoneal macrophages (LPM), which migrate towards the omentum as a result of inflammatory responses caused by cancer<sup>10</sup>. Consequently, the migration of peritoneal macrophages to the omentum has been suggested as a potential transport system for nanoparticles and other anticancer drugs. Conversely to IV injection, the recognition of nanoparticles by macrophages is extremely useful in the case of nanoparticles administered via IP. There is an increasing interest in trafficking nanoparticles across the peritoneal cavity to target primary intraperitoneal tumors but also metastatic tumors in the omentum. Ikehara *et al* observed the accumulation of cancer cells at the milky spots in the omentum, six hours after their injection via IP injection, resulting in the establishment of metastases and demonstrating that cancer cells do migrate to the omentum. More importantly, they demonstrated that oligomannose-coated liposomes encasing iron oxide magnetic nanoparticles injected via IP were efficiently taken up by peritoneal macrophages and transported to the omentum, with significant tumor suppression after MFH was applied<sup>11</sup>. Similar observations were made by Toraya-Brown

*et al* studying the IP and IV injection of different carbohydrate-coated magnetic nanoparticles to mice with intraperitoneal tumors and applying MFH after nanoparticle accumulation in the tumor. Results revealed that even when nanoparticles were not internalized into cancer cells at a great extent, there was a large nanoparticle accumulation in the tumor, and such accumulation was the result of nanoparticle trafficking by macrophages. Also, IP injection led to increased and deeper accumulation in the tumor when compared to IV injection, thus leading to significant heating and reduction of the tumor size after MFH treatment<sup>12</sup>.

One important aspect for nanoparticles to be effectively recognized and taken up by peritoneal macrophages is their polymeric coating. While polymers like PEG help to diminish such recognition in the systemic circulation when nanoparticles are injected via IV, carbohydrate-based polymers promote the recognition of nanoparticles by macrophages. This occurs because macrophages are rich in sugar and scavenger receptors, especially mannose receptors which have been reported and studied in the literature<sup>13-15</sup>. For example, mannan- and dextran-containing polymers have been reported as good coating alternatives for different nanoparticle platforms, and their potential for macrophage recognition and further uptake has been investigated both *in vitro* and *in vivo*. Carboxylic mannan- and dextran-coated nanoparticles were found to achieve high internalization patterns in mouse macrophages when compared to nanoparticles coated with other polymers that do not contain carbohydrate molecules<sup>16,17</sup>. The potential of IP injection of nanoparticles is currently investigated to treat other type of cancers such as brain and testis cancer, because it has been demonstrated that nanoparticles injected via IP can pass the blood-brain- and blood-testis-barriers<sup>18</sup>.

Our group has previously worked with subcutaneous cancer models and IT nanoparticle injections, and more recently, a peritoneal ovarian cancer model was successfully developed for

MFH studies using nanoparticles administered via IP. Using carboxymethyl dextran-coated nanoparticles, it was found that significant nanoparticle accumulation in the tumor occurred after IP injection as demonstrated by histological analysis, and synergy between MFH and the Hsp70 protein function inhibitor was also found<sup>19</sup>. However, determining the most appropriate route of administration of magnetic nanoparticles *in vivo* depends on the type of cancer model, nanoparticle properties and the expected outcomes of the study. Investigations on nanoparticle accumulation in different tumor models and using different injection approaches show that results are strongly dependent on nanoparticle properties, especially the surface charge. For example, a comparison study of IV and IP injections of gold nanoparticles in mice with subcutaneous ovarian cancer tumors revealed that neutral and zwitterionic coatings had longer circulation times regardless of the route of administration. As for accumulation in tumors, it was found that nanoparticles with either positive or negative charge had better accumulation in tumors with IV injection whereas nanoparticle distribution in body organs was higher with IP injection rather than IV<sup>20</sup>. Similarly, Harivardhan *et al* investigated the influence of the route of administration of etoposide-loaded solid lipid nanoparticles with negative charge in Dalton's lymphoma subcutaneous models in mice. At different time points after nanoparticle injection, biodistribution of nanoparticles in body organs such as liver, spleen and lungs was in the order IV > IP > IT, but the tumor uptake was in the order of IT > IP > IV<sup>21</sup>. Such results are different than those obtained by Arvizo *et al* with tumor uptake in the order IV > IP. However, and as stated before, care must be taken when doing comparisons because of the differences between cancer models, nanoparticle platforms, concentrations and physicochemical properties, mouse strain and age, and other factors which influence nanoparticle kinetics once injected in animals. Yet, agreement exist among other studies regarding nanoparticle biodistribution in key body

organs such as liver and spleen, which is expected to be higher for nanoparticles administered via IV. Jung *et al* observed significantly high nanoparticle accumulation in the liver with IV injection whereas nanoparticle accumulation in the spleen was greatly increased when nanoparticles were injected via IP<sup>22</sup>. From these studies, it is evident that IV injection consistently led to greater accumulation in the liver regardless of the polymeric coating, but results are conflicting in terms of what nanoparticle injection platform is better to achieve the highest accumulation in tumors.

Motivated by a need for alternatives to maximize the nanoparticle accumulation in tumors or regions where tumors grow, the present work investigated the potential of IP nanoparticle injection using a subcutaneous model of triple negative breast cancer (TNBC). The hypothesis of the study included two components. The first one was related to nanoparticle accumulation in subcutaneous tumors which was hypothesized to be higher for nanoparticles administered via IP than that for administration via IV. The second one involved nanoparticle accumulation in omental tissues along with uptake by peritoneal macrophages, which was hypothesized to be observed only with IP nanoparticle administration. A comprehensive study was carried out to investigate the pharmacokinetics (PK), biodistribution (BD) and tumor uptake of PEG-coated nanoparticle, using both IP and IV nanoparticle injections. Subsequently, the uptake of nanoparticles by peritoneal macrophages was investigated both qualitative and quantitatively. Results demonstrated that IP injection led to a gradual increase of iron in blood, followed by a subsequent exponential-decay clearance like that observed with IV injection. Also, IV injection led to higher nanoparticle accumulation in the liver and spleen, whereas IP injection promoted a substantial nanoparticle accumulation in the omentum. In addition, significant amounts of the original nanoparticle dose administered via IP is taken up by peritoneal macrophages and

consequently transported to the omentum. The presence of nanoparticles in peritoneal macrophages was confirmed using bright field microscopy images showing nanoparticle clusters inside cells, and also by Prussian Blue staining which revealed intense blue colorations for macrophages isolated from mice injected with nanoparticles. Therefore, the potential of the intraperitoneal route of administration was investigated and demonstrated for PEG-coated nanoparticles, and its utilization with orthotopic cancer models in the peritoneal region is strongly recommended for future experiments.

### **4.3 Experimental section**

#### **4.3.1 Materials**

Dubelco's modified eagle medium (DMEM), Roswell Park Memorial Institute (RPMI) 1640, phosphate buffered saline (PBS) solution, fetal bovine serum (FBS), L-glutamine, sodium bicarbonate, penicillin, streptomycin and Prussian Blue iron stain kit were purchased from Sigma-Aldrich (St. Louis, MO). All culture media and kits were prepared or used following the instructions of the manufacturer.

#### **4.3.2 Nanoparticles**

Iron oxide magnetic nanoparticles coated with polyethylene glycol (PEG) were prepared as described in the experimental section of Chapter 2 of this dissertation. Filter-sterilized aqueous nanoparticle suspensions were concentrated using centrifugal filter units (Amicon, Sigma Aldrich, St. Louis, MO) under aseptic conditions to yield concentrations of approximately 20 mg<sub>Fe</sub>/mL. The concentrated suspension was mixed with an equal volume of sterile PBS 0.02 M to yield a final nanoparticle suspension of approximately 10 mg<sub>Fe</sub>/mL. Nanoparticles were

injected via tail vein or in the abdomen of mice using 200  $\mu\text{L}$  of the nanoparticle suspension to yield a dose of approximately 100 mg/kg of mouse weight.

#### **4.3.3 Cell culture and subcutaneous breast cancer xenografts**

MDA-MB-231 4175 LM2 cells were donated by Dr. Dietmar W. Simann from the College of Medicine, University of Florida. Cells were cultured in DMEM culture medium, supplemented with 10% fetal bovine serum, 1% penicillin/streptomycin, 0.584 g/L of L-glutamine and 3.7 g/L of sodium bicarbonate. Cell cultures were kept at 37°C under a 5% CO<sub>2</sub> atmosphere, and split using a 1:3 ratio every three or four days until reaching ~ 80% confluence. To grow tumors, 6.0 – 7.0x10<sup>6</sup> cells in a total volume of 100  $\mu\text{L}$  of PBS 0.02 M were injected subcutaneously into the left mammary fat pad of athymic nude, female mice. Tumor growth was periodically monitored using a caliper and taking the mean of three consecutive measurements, for approximately four weeks. All the protocols in this work were performed according to the protocol approved by the *Institutional Animal Care and Use Committee (IACUC)*, University of Florida.

#### **4.3.4 Pharmacokinetics and biodistribution**

After nanoparticle injection either via IV or IP, blood samples of approximately 8  $\mu\text{L}$  were periodically taken via tail vein every 15 minutes during the first 1.5 hours, and gradually decreasing the frequency until completing 24 hours. Blood samples were collected in heparinized capillary tubes and stored at 4°C for further use. Twenty-four hours post injection mice were euthanized in a CO<sub>2</sub> rodent euthanasia chamber followed by cervical dislocation and then organ collection was performed including fat pad, kidneys, spleen, liver, heart, lungs, brain, and the tumor. Organs were collected in plastic vials, frozen at -80°C, lyophilized, and then plastic capsules with dried organ powders were filled for further use, recording the weight of organs and

tumor in each step. Furthermore, the iron content in blood samples and dried body organs/tumors was analyzed using an Electron Paramagnetic Resonance spectrometer (EPRs) (Brooker, Billerica, MA) using a set of both liquid and solid iron standards to determine the concentration of unknown samples.

#### **4.3.5 Isolation of peritoneal cavity cells and iron uptake**

After animal euthanasia as described in section 4.2.4, five milliliters of fetal bovine serum 3% in sterile PBS were injected into the abdomen of the mouse followed by a gentle massage of the abdominal area for a few seconds. The contents of the peritoneal wash were withdrawn with a sterile syringe and collected in a sterile tube, making sure that the liquid coming from the mouse's peritoneal cavity had no apparent blood. A second wash was performed as previously described and the collected liquid from washes was centrifuged and the supernatant was discarded. The obtained pellet was resuspended in culture media and then peritoneal cavity cells were manually counted with a hemocytometer using Trypan Blue live/dead cell exclusion, and results were recorded as total peritoneal cavity cells/mL. Afterwards, cells were seeded in non-treated petri dishes, let to attach for 24 – 72 hours at 37°C and 5% CO<sub>2</sub> with daily change of medium, washed with PBS to discard other peritoneal cells different than macrophages. Macrophages continued to be cultured for up to five days, and then they were laboriously detached from petri dishes using EDTA 5 mM and trypsin. Detached cells were centrifuged, resuspended in 500 µL of culture medium and manually counted using Trypan Blue live/dead exclusion. After cell counts were performed, cell suspensions were centrifuged one more time, the supernatant was discarded leaving approximately 50 µL in the tubes, and then capillary tubes were filled with cells suspension to account for at least  $2 \times 10^5$  cells/tube. The iron content in each capillary tube was quantified using EPRs and the iron uptake by peritoneal macrophages was

normalized by cell counts, reporting the results in  $\mu\text{g}_{\text{Fe}}/\text{cell}$ . A separate set of petri dishes with attached macrophages was also incubated for three days at  $37^{\circ}\text{C}$  and 5%  $\text{CO}_2$  after the non-attached peritoneal cavity cells were washed away and used for Prussian Blue staining of iron. Cells were fixed with paraformaldehyde, stained with an acid solution of potassium ferrocyanide 4%, pararosaniline 1% and eosin at 1 mg/mL, and rinsed thoroughly with deionized water. Once dry, petri dishes were imaged under a brightfield microscope and pictures were taken using a 20X objective.

## **4.4 Results and discussion**

### **4.4.1 Pharmacokinetics**

Iron concentrations in blood normalized by body weight of mice were determined as a function of time, using EPRs iron quantification of liquid blood samples, and experimental data were used for calculations of half-lives. Results are depicted in Figure 4.1, showing the mean value of experimental replicates, which are also shown for each timepoint rather than error bars, as suggested by Festing and Altman to a better understanding of variability in animal experiments<sup>24</sup>. It was found that PEG-coated nanoparticles immediately reached peak concentrations in the bloodstream when injected via IV, whereas gradual increments were detected when injected via IP, reaching peak concentrations approximately three hours post injection. As expected, IV injection resulted in higher iron concentrations in blood when compared to those achieved with IP injection. For example, peak iron concentrations with IV injection were 4-fold those obtained with IP injection with values in the order of  $10 \times 10^{-3}$  ( $\mu\text{g}/\mu\text{L}$ )/g and  $40 \times 10^{-3}$  ( $\mu\text{g}/\mu\text{L}$ )/g for IP and IV injections, respectively. However, care must be taken because pharmacokinetics for these two routes of administration are different. Upon IV

injection, 100% of injected nanoparticle dose is readily available in the bloodstream, and it is subsequently cleared from the systemic circulation following a first-order exponential decay. Pharmacokinetics in blood for nanoparticles injected via IP occurred in two separate stages: the first one is the absorption in the peritoneal cavity and the simultaneous, gradual nanoparticle accumulation in the bloodstream within three hours post injection, followed by nanoparticle being cleared from the bloodstream. Peak iron concentrations in the order of  $\sim [(8 \mu\text{g}/\mu\text{L})/\text{g}]$  were measured for IP injection approximately three hours post-injection and, interestingly, similar iron concentration values were detected in blood at that timepoint for nanoparticles injected via IV. The moment when iron concentrations in blood are similar for both routes of administration nanoparticle clearance for IP injection had just begun whereas that for IV injection dropped to approximately 25% of the injected dose. As mentioned before, the amounts of nanoparticles that reached the bloodstream with IP injection was lower when compared to IV injection. This occurred because only a small proportion of the original dose escapes from the peritoneal cavity, presumably via lymphatic diffusion, but most of the nanoparticle dose remains in the peritoneal cavity, as reported in the literature<sup>8</sup>. After peak concentrations are reached in the bloodstream, nanoparticles are rapidly cleared with similar kinetics to those observed for IV injection. The rapid nanoparticle clearance from the bloodstream suggests that elements from the MPS, presumably monocytes, are recognizing the circulating nanoparticles and taking them mainly to the liver for further metabolism. Such resemblances are demonstrated by comparing the half-lives of both routes of administration during nanoparticle clearance from the bloodstream. By definition, half-life is the time it takes for the concentration of a substance in the blood plasma to be reduced by 50%<sup>25</sup>. Hence, it was found that nanoparticle elimination kinetics was similar between the two routes of administration, with half-lives of 74 and 62 min for IV and

IP injections, respectively. When comparing these values to those reported in the literature, we found that half-lives of PEG-coated nanoparticles injected via IV range from 12 to 38 minutes for PEG with molecular weights up to 2 kDa, and values up to 150 min for molecular weights of 10 kDa<sup>26–28</sup>. In other words, the molecular weight of PEG is proportional to half-lives of nanoparticles. In this work, PEG with molecular weight of 5 kDa was used as a nanoparticle coating thus half-life values are in agreement with those that should be obtained for PEG with molecular weight of 5 kDa.

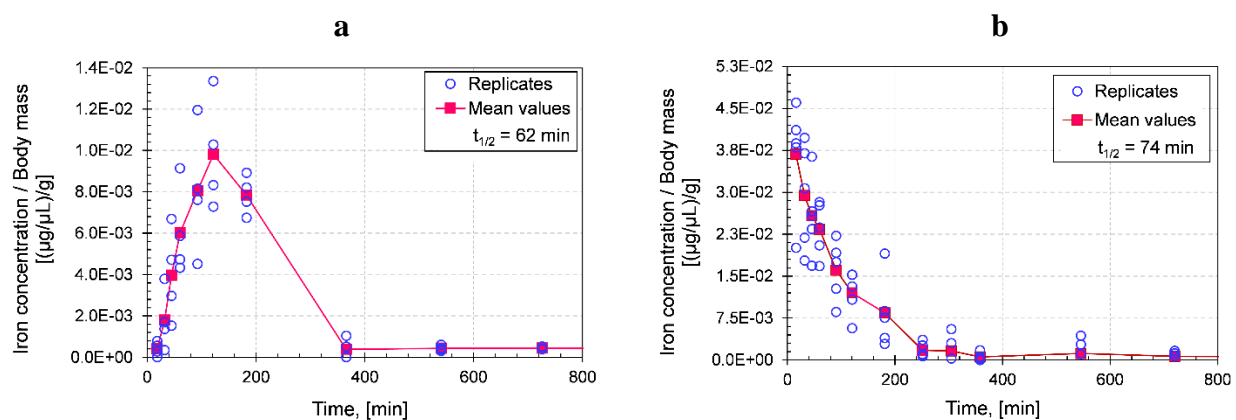


**Figure 4.1** Pharmacokinetics and half-lives of PEG-coated nanoparticles in blood. Hollow circles represent individual replicates and solid squares represent the mean values. Athymic nude mice were injected either, a) intraperitoneally or b) intravenously. Individual replicate values represent independent experiments carried out using 4 and 5 mice for a) and b), respectively.

#### 4.4.2 Biodistribution

Twenty-four hours post injection, nanoparticle accumulation in body organs was quantified using EPRs, as shown in Figure 4.2 for both IP and IV nanoparticle injections. Results are

presented as the iron content normalized by the dry mass of tissue, and the investigated organs in our study included liver, heart, kidneys, lungs, spleen, brain, fat pad and omentum. Nanoparticle accumulation was high in liver and spleen, as these organs are the major clearance pathways for nanoparticle clearance in the bloodstream. For IP injection, both liver and spleen had similar nanoparticle distribution profiles, with values in the order of  $5 \times 10^3 \mu\text{g}_{\text{Fe}}/\text{g}$  tissue which were also very similar to those reached with IV injection in the liver, and slightly lower in the spleen. These observations support the premise that for both routes of administration, once nanoparticles reach the systemic circulation, they are rapidly cleared from blood and taken up by elements of the mononuclear phagocytic system (MPS). There are reports of liposomes with hydrodynamic diameters of 50 nm injected via IP showing accumulation in the spleen slightly higher than that of the liver, which can be attributed to nanoparticles being absorbed by the lymphatic circulation<sup>29</sup>. The end point of nanoparticles after passing through lymph nodes and ducts, is the systemic circulation as reported previously in the literature for nanocarriers injected via IP<sup>23</sup>, which explains the gradual accumulation of nanoparticles in the bloodstream occurring within the three hours post injection as discussed in section 4.4.1. Organs such as heart, kidneys, lungs, brain and fat pad had very low or even undetectable nanoparticle accumulation, with iron contents below the limit of detection in most of the cases, excluding kidneys and lungs for IV injection which were barely above such limit. Similar findings regarding minimal quantities of nanoparticles in these organs have also been reported for PEGylated iron oxide nanoparticles injected via IV<sup>30</sup>. As for nanoparticle accumulation in the omentum, IP injection led to a notably high iron distribution in the organ, with values of approximately  $20 \mu\text{g}_{\text{Fe}}/\text{g}$  which is 4-fold the iron mass accumulated in the liver. Such high value indicates the potential of targeting the omentum, as a key tissue to accumulate high nanoparticle concentrations for cancer therapy,

especially for MFH applications as demonstrated in previous studies<sup>12</sup>. The mechanisms of nanoparticle transport from the site of injection to the omentum via IP may include a combination of diffusion through the interstitial fluid and macrophage-mediated transport. Nanoparticle accumulation in the omentum for mice injected via IV was undetectable, which was expected to occur as it has been previously reported<sup>31</sup>. Figure 4.3 shows an excised omentum from one of the animals injected with nanoparticles via IP where the intense brown color distinctive of PEG-coated nanoparticles can be easily observed, similarly to the observations made by Ikehara *et al*<sup>11</sup>. When seen under a brightfield microscope at 40X, magnified omental tissues can be observed along with nanoparticles agglomerated in several areas, indicated by yellow arrows. Based on our observations and those from the literature, we hypothesize that nanoparticles were trafficked from the intraperitoneal cavity to the omentum by peritoneal macrophages.

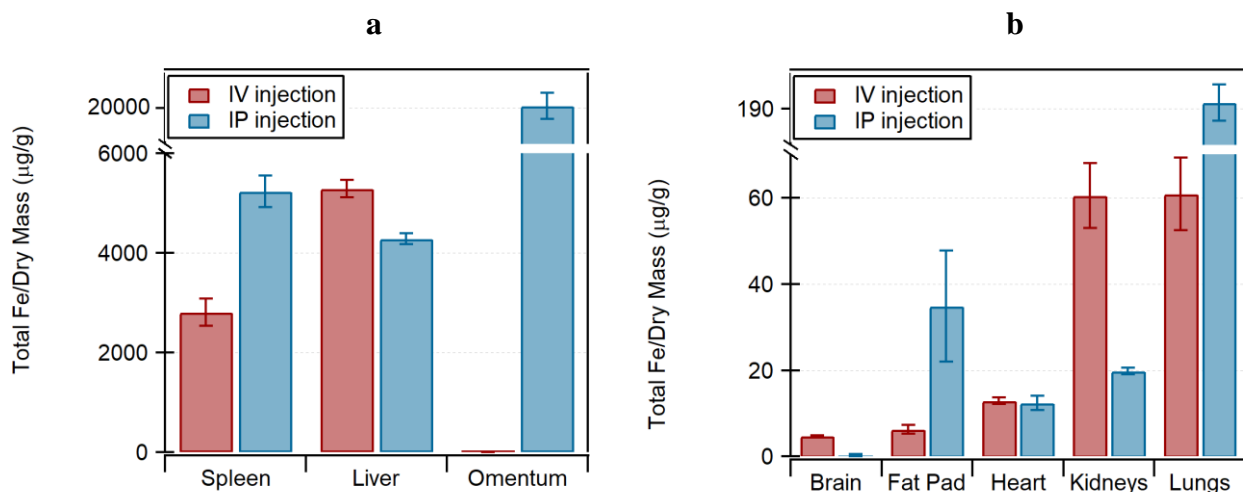


**Figure 4.2.** Biodistribution of PEG-coated nanoparticles in body organs of athymic nude mice injected either intraperitoneally or intravenously. a) Organs with significant nanoparticle accumulation. b) Organs with small nanoparticle accumulation. Error bars represent the standard error of independent experiments carried out with four mice.



**Figure 4.3** Excised omentum from a mouse, twenty-four hours after IP injection, showing significant nanoparticle accumulation. a) Brown-colored omentum showing high nanoparticle accumulation, b) brightfield micrograph of omental tissues with nanoparticle clusters indicated by yellow arrows.

Biodistribution in body organs was also studied at different timepoints post injection to investigate whether the accumulation of nanoparticles in body organs is time dependent or not, thus the IP injection approach was chosen to conduct the test. The chosen timepoints were 3, 6 and 12 hours, and we were particularly interested in comparing results three-hour post injection because based on pharmacokinetics results, is the approximate time required for nanoparticle clearance after they reach peak concentrations in blood. As shown in Figure 4.4, the omentum had a significant increase of iron contents between 3 and 6 hours, and between 3 and 12 hours post-injection ( $p$ -values of 0.008 and 0.02, respectively) whereas the spleen revealed a relatively constant iron content. However, no net increment of iron was observed beyond 6 hours, which indicates that maximal nanoparticle accumulations were achieved in this time period and that nanoparticle accumulation was, in fact, time dependent within 6 hours post-injection. Noticeably, nanoparticle accumulation in the omentum 6-hour post injection was 4-fold the one found after

the first three hours, and it was also 4-fold the iron found in the liver for the same studied time period. This is the same ratio observed between the omentum and the liver for biodistribution experiments after 24 hours, discussed previously, thus it was demonstrated that results are consistent and reproducible. Gradual increments and time-dependent nanoparticle accumulation in the omentum has been also previously reported, with plateau up to 24 hours<sup>31</sup>. Similarly, to the observations from biodistribution experiments 24-hour post injection, the remaining organs such as brain, kidneys, lungs, heart and fat pad had very low or undetectable iron concentrations.

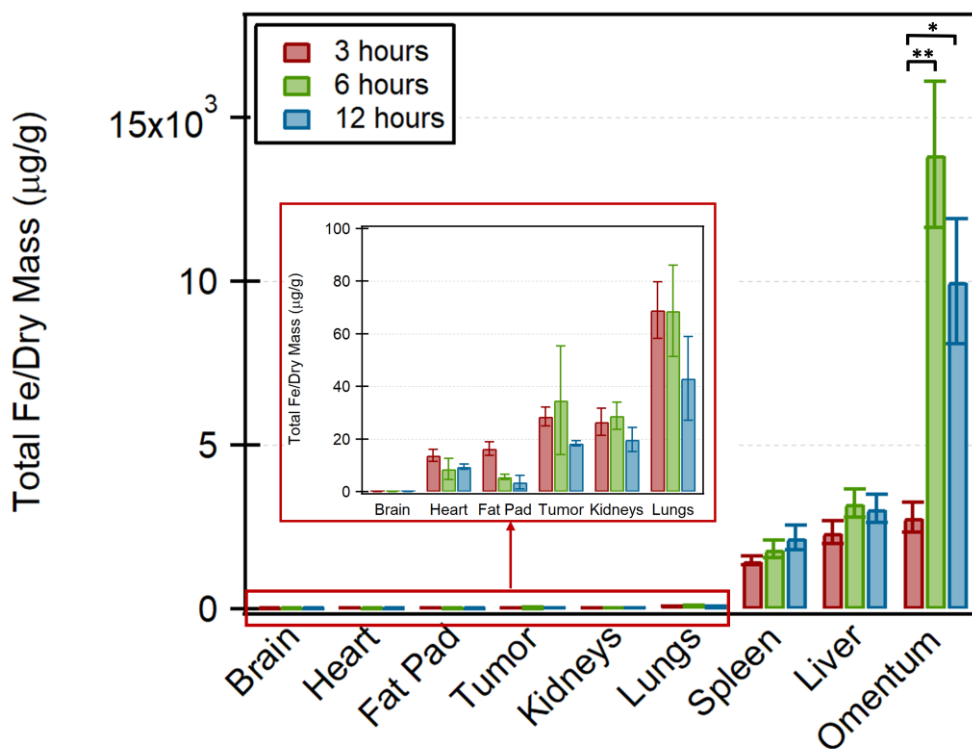


**Figure 4.4** Biodistribution of PEG-coated nanoparticles in body organs and tumor at 3, 6 and 12 hours after IP injection. Error bars represent the standard error of 3 independent experiments.

#### 4.4.3 Nanoparticle accumulation in subcutaneous tumors

Triple negative breast cancer (TNBC) human xenografts grown in the fat pad of female athymic nude mice were also used to investigate the nanoparticle accumulation profiles using both IV and IP nanoparticle injections. As shown in figure 4.5, nanoparticles injected intravenously resulted in higher accumulation in tumors when compared to the IP route of administration, with the latter leading to very low iron contents in tumor tissues, mostly below the limit of detection. However, the iron accumulation in tumors via IV injection was low when compared to those quantified in organs such as liver and spleen, indicating that only a small percentage of the injected dose (ID) reached the tumor. Table 4.1 summarizes the % ID during the study along with tumor volumes and the ID for each individual animal. These results are below the median delivery efficiency as reported by a recent dosimetry analysis of nanoparticle delivery to tumors, which has found that only 0.7% of ID reached the tumor<sup>3</sup>. The reason behind these low amounts of nanoparticles in tumors was the high degree of nanoparticle sequestration by the MPS, primarily monocytes from the blood stream, which rapidly identified the circulating nanoparticles thus taking them to the liver and spleen. Even when PEG is still considered as the best coating option for magnetic nanoparticles, there is evidence that accelerated blood clearance of PEG-coated nanoparticles still prevails, characterized by high rates of nanoparticle uptake by MPS, especially with repeated injections<sup>32</sup>. Therefore, additional efforts are still required to improve the delivery of non-targeted PEG-coated nanoparticles to tumors using IV injection along with the EPR effect as a strategy for nanoparticle delivery to tumors. From these observations, it is obvious that IP injection is not a practical approach to increase the delivery of PEG-coated nanoparticle to subcutaneous breast cancer models. However, according to the discussion in the previous section, the potential of IP injection to accumulate nanoparticles in the

omentum was demonstrated and is the starting point for further experiments using peritoneal models (e.g. ovarian cancer) to study transport mechanisms and delivery efficiency.

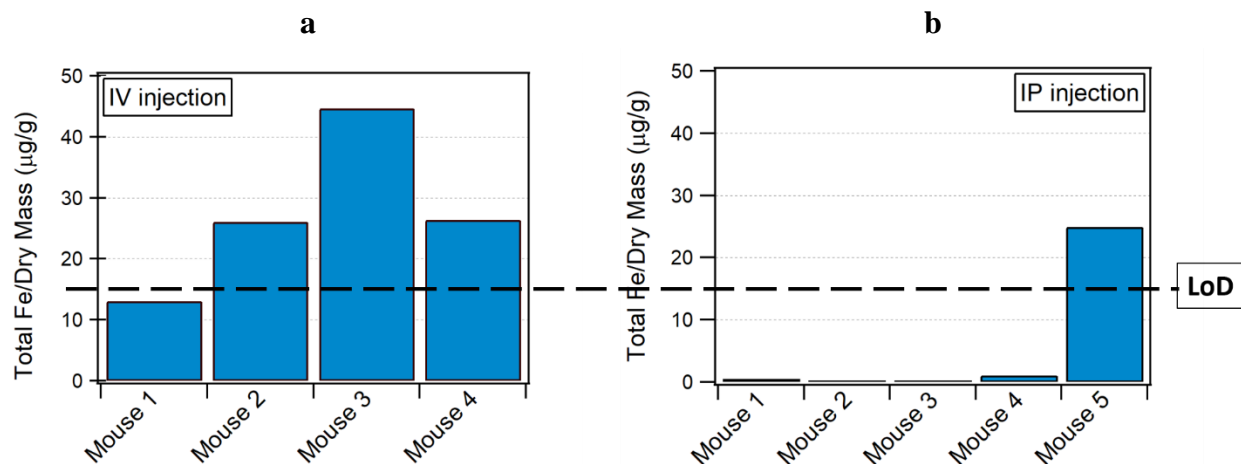


**Figure 4.5** Comparison of nanoparticle accumulation in TNBC xenografts twenty-four hours post injection either a) intravenously, or b) intraperitoneally

**Table 4.1.** Delivery efficiency of nanoparticle delivery to tumors with IV injection

Animal	Tumor volume (mm <sup>3</sup> )	Injected dose (mg <sub>Fe</sub> /kg)	% ID
Mouse 1	1402	118.08	0.09
Mouse 2	495	143.67	0.09
Mouse 3	1522	151.89	0.04
Mouse 4	485	137.75	0.09

#### 4.4.4 Nanoparticle uptake by peritoneal macrophages

Peritoneal cavity cells isolated from mice as described in section 4.2.5, yielded average cell numbers of approximately  $4.2 \times 10^6$  cells/mouse after peritoneal washes, defined as total peritoneal cavity cells including macrophages, T and B cells, dendritic cells, eosinophils, neutrophils, and other cell subsets<sup>33</sup>. Among these cells, only macrophages were attached to petri dishes whereas the remaining non-macrophage cell populations floated in the culture medium, and they were easily washed away. After 4-day culture with periodical change of culture medium, macrophages were detached and counted, yielding an average of  $\sim 4.7 \times 10^5$  cells/mouse, which is in agreement to those reported in the literature using a similar, non-elicited isolation protocol<sup>34</sup>. Cell counts and macrophage recovery fractions are included in Table 4.2, and adherent mouse macrophages as seen under the microscope are illustrated in Figure 4.6. Interestingly, mouse macrophages exhibited a very strong attachment behavior, even when cultured in non-treated petri dishes as suggested elsewhere<sup>34</sup> thus cell detachment was remarkably arduous. Gentle cell scraping technique was used to improve cell detachment, but it led to considerable cell death. Cold EDTA solutions (5 mM) were used with incubation times up to 20 minutes to promote cell detachment but most cells were still attached to plates. Trypsin-EDTA 0.05% (0.5 mL) was then added to the remaining adhered macrophages, incubated for 5 min and neutralized with additional cold EDTA 5mM, which improved cell detachment. Even when the use of trypsin-EDTA improved cell detachment, its use with peritoneal macrophages is not recommended because it interferes with macrophage characterization, especially those of flow cytometry and immunohistochemistry staining.

**Table 4.2.** Cell numbers after isolation of peritoneal macrophages in athymic nude mice

<b>Animal</b>	<b>Total peritoneal cells (x10<sup>6</sup>)</b>	<b>Attached macrophages (x10<sup>5</sup>)</b>	<b>Macrophage fraction (%)</b>
Mouse 1	1.95	2.32	11.90
Mouse 2	5.25	8.20	15.62
Mouse 3	4.80	4.62	9.63
Mouse 4	4.85	3.62	7.46

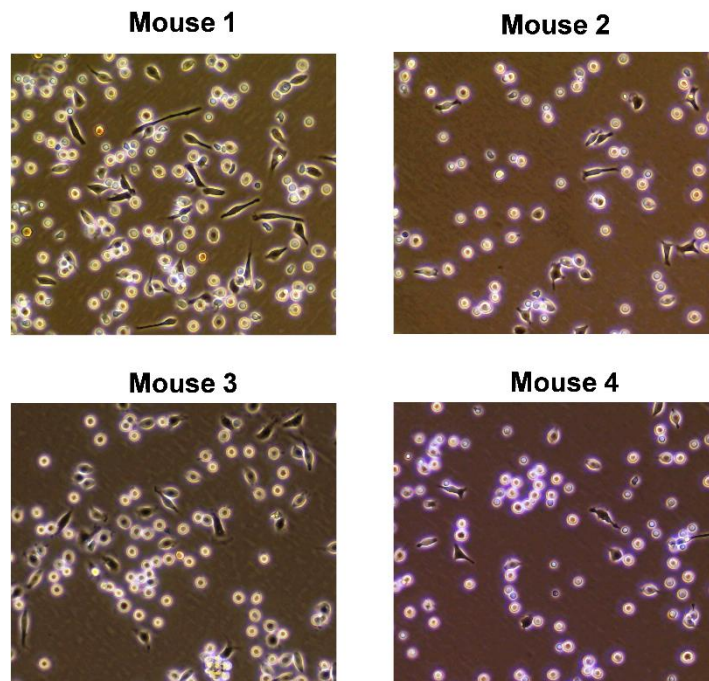


**Figure 4.6** Mouse macrophages adhered to non-treated petri dishes, four days after non-elicited isolation from mice. Images were obtained using a 20X objective.

Nanoparticle uptake by peritoneal macrophages was inspected under the optical microscope after the remaining non-adherent cells were washed away, and as shown below in Figure 4.7-a, nanoparticle clusters can be seen closely associated to macrophages. We hypothesized that nanoparticles were internalized into macrophages since the culture medium was changed periodically during three days after peritoneal cavity cells were seeded in petri dishes, thus free nanoparticles in the liquid medium should be greatly minimized. To demonstrate our hypothesis, macrophages were laboriously detached, washed and pelleted for iron quantification using EPRs and as shown in Figure 4.7-b, the iron oxide spectrum in the macrophage sample was precisely identified. To avoid any overestimation of iron oxide, spectra comparison was carried out showing that neither cells alone nor supernatants from macrophage detachment had paramagnetic signals, as their spectra are virtually the same as that from deionized water. In addition, the spectrum of an iron oxide standard with concentration of 50 $\mu$ g/mL is also shown, demonstrating that nanoparticles were internalized by macrophages. From these measurements along with cell counts obtained during macrophage detachment, it was found that nanoparticle internalization into macrophages occurred with values up to 0.192  $\rho_{\text{Fe}}$ /cell.

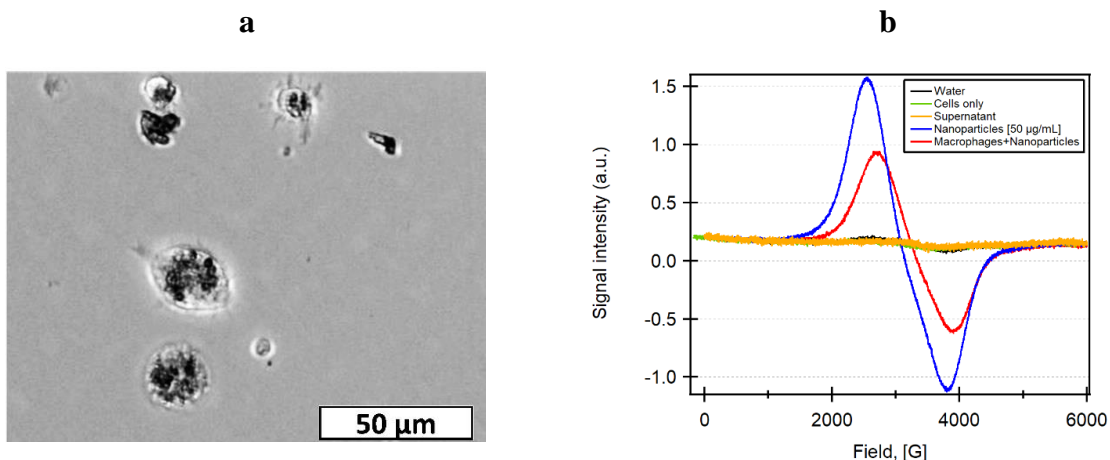


**Figure 4.7** Nanoparticle uptake by mouse peritoneal macrophages after IP injection. a) Brightfield microscope image using a 40X objective, b) EPRs spectra of iron oxide internalized into macrophages.

Additionally, nanoparticle internalization into mouse peritoneal macrophages was also assessed by Prussian Blue staining using macrophages fixed in petri dishes, and treated with hydrochloric acid and potassium ferrocyanide. As shown in Figure 4.8, intense blue colored macrophages were observed for mice receiving IP nanoparticle injection which indicates the presence of iron oxide inside cells. Similar techniques have been reported by others, using Prussian Blue staining to study the internalization of iron oxide nanoparticles coated with human serum albumin into macrophages at different timepoints<sup>35</sup>.

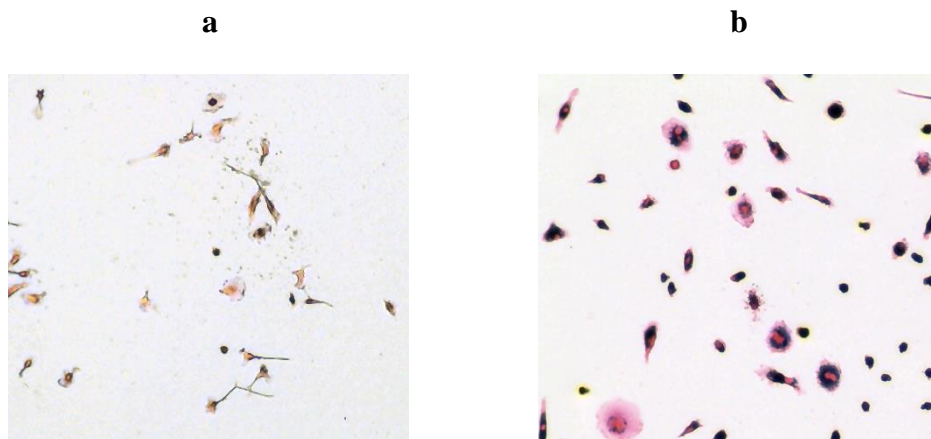


**Figure 4.8** Prussian Blue staining of PEG-coated, iron oxide magnetic nanoparticles taken up by mouse peritoneal macrophages. a) Control group -no nanoparticles-, b) Experimental group -nanoparticles injected via IP

In the light of results achieved for nanoparticle uptake by peritoneal macrophages and high nanoparticle accumulation in omental tissues, it is highly recommended to conduct further experiments. It is suggested to develop an intraperitoneal cancer model which was not possible by the time this work was conducted because of the current IACUC protocols, valid only for subcutaneous breast cancer models. Writing, submitting, and getting approval for a new IACUC protocol, and the subsequent time required to obtain and characterize IP tumors was not feasible within the limited timeframe to perform these experiments in facilities other than ours. In addition, the preparation of dextran- and mannose-based polymeric coatings and their conjugation to nanoparticles is still underway and requiring further optimization. Such additional nanoparticle platforms will allow to target receptors overexpressed in peritoneal macrophages, which will enhance the results when working with intraperitoneal cancer models.

## 4.5 Conclusions

Results included in this chapter exploit the potential of IP injection, using a systematic comparison of pharmacokinetics and biodistribution profiles between IP injection and the traditional IV route of administration. This preliminary work presents evidence of high nanoparticle accumulation in the omentum via IP injection, which was substantially higher than that occurring in the liver and spleen. These findings are of utmost importance because they support observations from previous work of this research group carried out with carboxymethyl dextran-coated nanoparticles injected via IP, with orthotopic ovarian cancer models. In that work, nanoparticle accumulation in tumors was qualitatively studied and attributed to macrophage-mediated nanoparticle transport<sup>19</sup>. This work demonstrated both qualitative and quantitatively that peritoneal macrophages efficiently take up PEG-coated nanoparticles upon IP injection, resulting in iron uptake values up to 0.192  $\mu\text{g}_{\text{Fe}}/\text{cell}$ . The observed uptake patterns highlight the potential of these immune cells to be used as vehicles for nanoparticle delivery to tumors and metastases occurring in the peritoneal cavity. No significant nanoparticle accumulation in subcutaneous tumors was found either with intravenous or intraperitoneal injection, thus the pursuit of increased nanoparticle delivery to tumors remains a challenge. Findings on nanoparticle accumulation in omental tissues and the potential of macrophage-mediated nanoparticle transport are the pillars for future experiments using intraperitoneal cancer models.

## 4.6 References

1. Chatterjee, D. K., Diagaradjane, P. & Krishnan, S. Nanoparticle-mediated hyperthermia in cancer therapy. *Ther. Deliv.* **2**, 1001–1014 (2011).

2. Kobayashi, H., Watanabe, R. & Choyke, P. L. Improving Conventional Enhanced Permeability and Retention (EPR) Effects; What Is the Appropriate Target? *Theranostics* **4**, 81–89 (2014).
3. Wilhelm, S. *et al.* Analysis of nanoparticle delivery to tumours. *Nat. Rev. Mater.* **1**, 16014 (2016).
4. Chen, W. C., Zhang, A. X. & Li, S.-D. Limitations and niches of the active targeting approach for nanoparticle drug delivery. *Eur. J. Nanomedicine* **4**, 89–93 (2012).
5. Cole, A. J. *et al.* Polyethylene glycol modified, cross-linked starch-coated iron oxide nanoparticles for enhanced magnetic tumor targeting. *Biomaterials* **32**, 2183–2193 (2011).
6. Giustini, A. J., Ivkov, R. & Hoopes, P. J. Magnetic nanoparticle biodistribution following intratumoral administration. *Nanotechnology* **22**, 345101 (2011).
7. Hilger, I., Hergt, R. & Kaiser, W. A. Use of magnetic nanoparticle heating in the treatment of breast cancer. *IEE Proc. - Nanobiotechnology* **152**, 33 (2005).
8. Bajaj, G. & Yeo, Y. Drug Delivery Systems for Intraperitoneal Therapy. *Pharm. Res.* **27**, 735–738 (2010).
9. Krist, L. F. G. *et al.* Milky spots in the greater omentum are predominant sites of local tumour cell proliferation and accumulation in the peritoneal cavity. *Cancer Immunol. Immunother.* **47**, 205–212 (1998).
10. Cassado, A. A., D’Império Lima, M. R. & Bortoluci, K. R. Revisiting mouse peritoneal macrophages: Heterogeneity, development, and function. *Front. Immunol.* **6**, 1–9 (2015).

11. Ikehara, Y. A Carbohydrate Recognition-Based Drug Delivery and Controlled Release System using Intraperitoneal Macrophages as a Cellular Vehicle. *Cancer Res.* **66**, 8740–8748 (2006).
12. Toraya-Brown, S. *et al.* Phagocytes mediate targeting of iron oxide nanoparticles to tumors for cancer therapy. *Integr. Biol. (Camb)*. **5**, 159–71 (2013).
13. Gordon, S. & Taylor, P. R. Monocyte and macrophage heterogeneity. *Nat. Rev. Immunol.* **5**, 953–964 (2005).
14. Mantovani, A., Sozzani, S., Locati, M., Allavena, P. & Sica, A. Macrophage polarization: Tumor-associated macrophages as a paradigm for polarized M2 mononuclear phagocytes. *Trends Immunol.* **23**, 549–555 (2002).
15. Zhu, S., Niu, M., O'Mary, H. & Cui, Z. Targeting of Tumor-Associated Macrophages Made Possible by PEG-Sheddable, Mannose-Modified Nanoparticles. *Mol. Pharm.* **10**, 3525–3530 (2013).
16. Xie, J., Xu, C., Kohler, N., Hou, Y. & Sun, S. Controlled PEGylation of Monodisperse Fe<sub>3</sub>O<sub>4</sub> Nanoparticles for Reduced Non-Specific Uptake by Macrophage Cells. *Adv. Mater.* **19**, 3163–3166 (2007).
17. Vu-Quang, H. *et al.* Carboxylic mannan-coated iron oxide nanoparticles targeted to immune cells for lymph node-specific MRI in vivo. *Carbohydr. Polym.* **88**, 780–788 (2012).
18. Kim, J. S. *et al.* Toxicity and Tissue Distribution of Magnetic Nanoparticles in Mice.

- Toxicol. Sci.* **89**, 338–347 (2006).
19. Court, K. A. *et al.* HSP70 Inhibition Synergistically Enhances the Effects of Magnetic Fluid Hyperthermia in Ovarian Cancer. *Mol. Cancer Ther.* **16**, 966–976 (2017).
  20. Arvizo, R. R. *et al.* Modulating Pharmacokinetics, Tumor Uptake and Biodistribution by Engineered Nanoparticles. *PLoS One* **6**, e24374 (2011).
  21. Harivardhan Reddy, L., Sharma, R. K., Chuttani, K., Mishra, A. K. & Murthy, R. S. R. Influence of administration route on tumor uptake and biodistribution of etoposide loaded solid lipid nanoparticles in Dalton's lymphoma tumor bearing mice. *J. Control. Release* **105**, 185–198 (2005).
  22. Jung, C. *et al.* Intraperitoneal Injection Improves the Uptake of Nanoparticle-Labeled High-Density Lipoprotein to Atherosclerotic Plaques Compared With Intravenous Injection: A Multimodal Imaging Study in ApoE Knockout Mice. *Circ. Cardiovasc. Imaging* **7**, 303–311 (2014).
  23. Kohane, D. S. *et al.* Biodegradable polymeric microspheres and nanospheres for drug delivery in the peritoneum. *J. Biomed. Mater. Res. Part A* **77A**, 351–361 (2006).
  24. Festing, M. F. W. & Altman, D. G. Guidelines for the Design and Statistical Analysis of Experiments Using Laboratory Animals. *ILAR J.* **43**, 244–258 (2002).
  25. Ahmed, T. A. in *Basic Pharmacokinetic Concepts and Some Clinical Applications* (ed. Pesek, K.) (InTech, 2015). doi:10.5772/61573
  26. Ruiz, a. *et al.* Biodistribution and pharmacokinetics of uniform magnetite nanoparticles

- chemically modified with polyethylene glycol. *Nanoscale* **5**, 11400 (2013).
27. Arami, H., Khandhar, A., Liggitt, D. & Krishnan, K. M. In vivo delivery, pharmacokinetics, biodistribution and toxicity of iron oxide nanoparticles. *Chem. Soc. Rev.* **44**, 8576–8607 (2015).
  28. Moffat, B. a *et al.* A Novel Polyacrylamide Magnetic Nanoparticle Contrast Agent for Molecular Imaging using MRI. *Mol. Imaging* **2**, 324–332 (2003).
  29. Hirano, K. & Hunt, C. A. Lymphatic Transport of Liposome-Encapsulated Agents: Effects of Liposome Size Following Intraperitoneal Administration. *J. Pharm. Sci.* **74**, 915–921 (1985).
  30. Gu, L., Fang, R. H., Sailor, M. J. & Park, J.-H. In Vivo Clearance and Toxicity of Monodisperse Iron Oxide Nanocrystals. *ACS Nano* **6**, 4947–4954 (2012).
  31. Ikehara, Y. *et al.* A carbohydrate recognition-based drug delivery and controlled release system using intraperitoneal macrophages as a cellular vehicle. *Cancer Res.* **66**, 8740–8748 (2006).
  32. Zhao, Y. *et al.* A frustrating problem: Accelerated blood clearance of PEGylated solid lipid nanoparticles following subcutaneous injection in rats. *Eur. J. Pharm. Biopharm.* **81**, 506–513 (2012).
  33. Ray, A. & Dittel, B. N. Isolation of Mouse Peritoneal Cavity Cells. *J. Vis. Exp.* 10–12 (2010). doi:10.3791/1488
  34. Zhang, X., Goncalves, R. & Mosser, D. M. The Isolation and Characterization of Murine

Macrophages. *Curr. Protoc. Immunol.* / Ed. by John E.Coligan ...[et al.] **CHAPTER,**  
Unit-14 (2008).

35. Xie, J. *et al.* Human serum albumin coated iron oxide nanoparticles for efficient cell labeling. *Chem. Commun.* **46**, 433–435 (2010).

# Chapter 5

## ***Final Remarks: Conclusions and Dissertation Contributions***

---

The aim of this dissertation was the optimization of experimental methodologies in response to challenges that Magnetic Fluid Hyperthermia (MFH) currently faces as an adjuvant in cancer therapy. To accomplish this goal, strategies included the optimization of: (i) synthesis and peptization conditions to increase the heat dissipation rates of nanoparticles; (ii) the use of low-intensity focused ultrasound (LIFU) to enhance the cellular uptake of chemotherapeutic drugs and nanoparticles; and (iii) the intraperitoneal administration of nanoparticles to target peritoneal macrophages, with subsequent particle accumulation in specific intraperitoneal sites.

Results presented in this dissertation demonstrated that remarkably high heat dissipation rates were obtained for iron oxide nanoparticles, both in liquid and solid matrices. Importantly, the high SAR values were obtained by using a simple, cost-effective and straightforward co-precipitation method, along with an ultrasonic-assisted and enhanced peptization step. From the high SAR values obtained, those for solid matrices were found to exceed the reported values by the moment the study was conducted, for similar co-precipitation synthesis approaches. Such observations demonstrate that the synthesized nanoparticles are capable to dissipate substantial amounts of heat, even when restricted from physical rotation. The reproducibility of the optimized synthesis method was confirmed, and high SAR values were consistently obtained within the predicted limits. Ultimately, coating nanoparticles with a layer of PEG-Silane resulted in colloidal suspensions with excellent stability in various biological media for several days.

This dissertation demonstrated that the use of microbubble-mediated ultrasound led to significant potentiation of toxic effects of MFH and 2-phenylethanesulfonamide (PES) *in vitro*, either individually or as combined therapies. The ultrasonic-potentiation of MFH/PES was confirmed at mild hyperthermia conditions (41°), indicating that the proposed combination therapies can improve the effects of MFH, even when temperatures at the hyperthermia range (43-47°C) were not achieved. These improvements were achieved after a systematic optimization of ultrasound conditions to induce maximum cell membrane permeabilization/poration with minimal damage to cell viability. When ultrasound was incorporated before magnetic field exposure, the cell killing profile of MFH/PES combination therapies previously reported as synergistic, was significantly increased as a result of enhanced cellular uptake of PES and nanoparticles. These findings are of utmost relevance because, at the moment this dissertation was written, the use of LIFU to improve the performance of MFH has not been reported. Therefore, it is expected that results presented in this dissertation become the foundations for the establishment of a novel sono-thermo-chemotherapy.

Results from *in vivo* experiments exploit the potential of intraperitoneal administration of nanoparticles to target peritoneal macrophages, aiming to use them as vehicles for nanoparticle transport inside the peritoneal cavity. Nanoparticle accumulation in subcutaneous breast tumors was low for IP injection, though IV injection did not significantly improve tumor uptake. Evidence of large nanoparticle accumulation in omental tissues was presented, substantially higher than that observed in the liver and spleen. The uptake of nanoparticles by peritoneal macrophages was quantitatively confirmed, demonstrating that macrophages were able to recognize and take up nanoparticles upon IP injection. Therefore, results presented herein are

considered an important starting point to continue additional investigations using intraperitoneal cancer models that originate or metastasize in the omentum.

Furthermore, this work also incorporated additional experimental protocols, characterization techniques and quantification platforms that can be used by this research group in the future. Dynamic magnetic susceptibility was used for complementary assessment of magnetic behavior and colloidal stability of nanoparticles. The use of paramagnetic resonance spectroscopy (EPRs) was also implemented for quantitative determination of nanoparticle accumulation in blood, body organs and peritoneal macrophages. The protocol for the isolation of mouse peritoneal macrophages was refined and it can be subsequently optimized in future *in vivo* experiments.

# Appendix

## A.1 Mapping of acoustic intensity at the target region

The acoustic intensity plotted as a function of distance at the target region of the transducer (horizontal and vertical) is shown in Figure A.1a and A.1b. In addition, characterization included acoustic intensity measurements as a function of the input voltage in the focal point. This was performed by varying the input voltage from 0.1 to 5 V at steps of 0.1 V. Results of intensity as a function of voltage are shown in Figure A.2 with experimental data fitted to a second-order polynomial model, as depicted in equation 3.2 for a frequency of 1.1 MHz.

$$I_{1.1} = 0.0074 * V_{in}^2 + 0.0293 * V_{in} - 0.1525 \quad (\text{A.1})$$

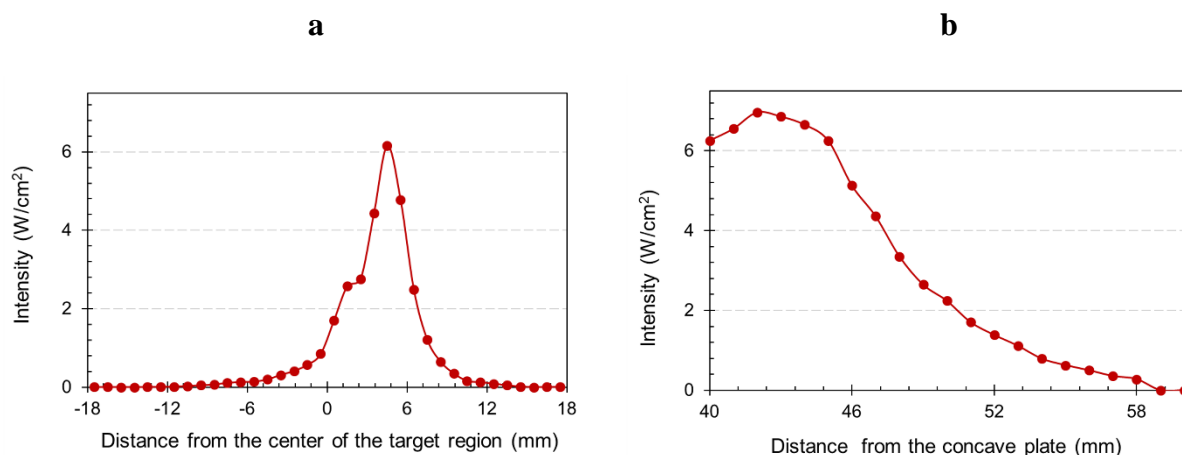


**Figure A.1.** Acoustic intensity mapping at the target region,  $f = 1.1$  MHz. a) Horizontally (total diameter of target region is 35 mm). b) Vertically, from the concave plate of transducer.

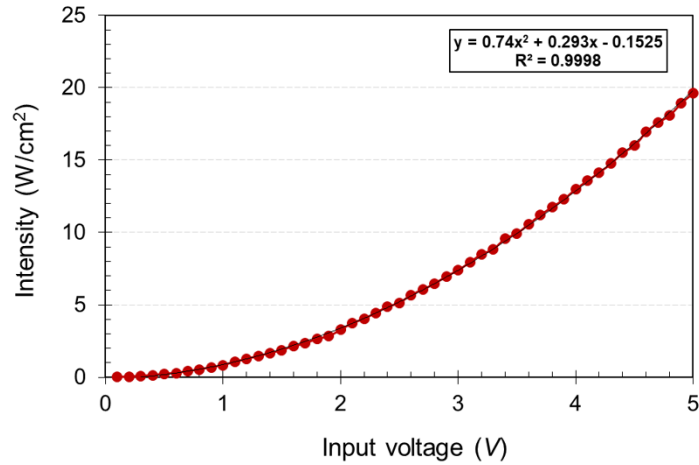


**Figure A.2.** Distribution of acoustic intensity as a function of input voltage, as measured in the target region. Experimental data was fitted to a second-order polynomial model (included).

### A.2 Comparison of Trypan Blue vs Calcein-AM to determine cell viability

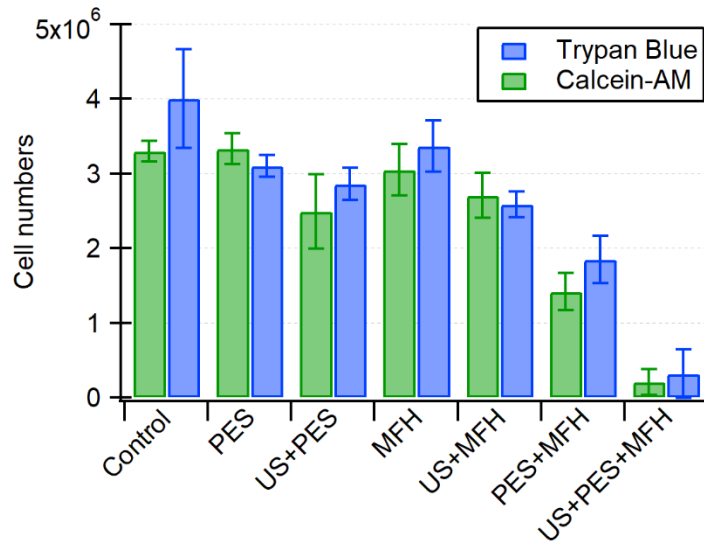


**Figure A.3.** Live cell counts determined by Trypan Blue exclusion (blue bars) compared to metabolically active cells emitting green fluorescence, determined by Calcein-AM staining using image cytometry.

### **A.3 Authorization for *in vivo* experiments issued by IACUC for University of Florida**

Notification of Initial Approval

From: [Michael Katovich](#)

To: [Carlos Rinaldi](#)

CC: [Chris Pampo](#)

Re: Continuing Review ID: [IC00005914](#)  
2016 Review for 201508852

Title: Pilot Studies to Evaluate EGFR-Targeted Magnetic Nanoparticle Accumulation and Induction of Lysosomal Death Pathways in Triple Negative Breast Cancer Rodent Models

I am pleased to inform you that the Continuation for study [201508852](#) was APPROVED on 3/15/2016 . You are required to return to this site at least 60 days prior to the Expiration Date of 5/6/2017 and file a Continuation or a Triennial.

If this IACUC protocol pertains to a sponsored research project it is the responsibility of the PI to forward a copy of IACUC approval and associated PeopleSoft Project number to the Office of Award Administration via Fax at (352) 392-4522 or email at [ufawards@ufl.edu](mailto:ufawards@ufl.edu)

Sincerely,



[Michael Katovich](#)

IACUC Chair

**Institutional Animal Care & Use Committee**  
**PO Box 100142**  
**Gainesville, Florida 32610-0142**  
**Tele: (352) 273-9535 Fax: (352) 273-9538**

Notification of Initial Approval

From: [Michael Katovich](#)

To: [Carlos Rinaldi](#)

CC: [Chris Pampo](#)

Re: Continuing Review ID: [IC00005914](#)  
2016 Review for 201508852

Title: Pilot Studies to Evaluate EGFR-Targeted Magnetic Nanoparticle Accumulation and Induction of Lysosomal Death Pathways in Triple Negative Breast Cancer Rodent Models

I am pleased to inform you that the Continuation for study [201508852](#) was APPROVED on 3/15/2016 . You are required to return to this site at least 60 days prior to the Expiration Date of 5/6/2017 and file a Continuation or a Triennial.

If this IACUC protocol pertains to a sponsored research project it is the responsibility of the PI to forward a copy of IACUC approval and associated PeopleSoft Project number to the Office of Award Administration via Fax at (352) 392-4522 or email at [ufawards@ufl.edu](mailto:ufawards@ufl.edu)

Sincerely,



[Michael Katovich](#)

IACUC Chair

**Institutional Animal Care & Use Committee**  
**PO Box 100142**  
**Gainesville, Florida 32610-0142**  
**Tele: (352) 273-9535 Fax: (352) 273-9538**